

## ABSTRACT

Rhome, Jamie Robert. An Analysis of Hurricane Debby (2000) and the Impact of Vertical Shear on the GFDL Forecast Performance. (Under the direction of Dr. Sethu Raman).

The need for improved tropical cyclone (TC) intensity guidance has never been greater given recent upward population trends in coastal areas. The difficulty in forecasting rapid intensity change remains one of the more challenging aspects of TC forecasting and was recently highlighted by the unexpected weakening of Hurricane Debby (2000) along the northern coast of Hispaniola on August 23, 2000. To address the need for improved understanding of rapid intensity change and the ability of dynamical TC models to accurately forecast intensity, a three-dimensional dynamical TC model (GFDL) is analyzed during the lifecycle of Debby. This was accomplished by first performing a comprehensive observational analysis making use of observed in-situ data as well as remotely sensed satellite data and derived products. Results from this analysis indicate that rapidly increasing vertical shear was the primary catalyst for the sudden weakening.

Accordingly, vertical shear was analyzed within several operational simulations of the GFDL model near the time of weakening. This was accomplished by comparing the GFDL initial and forecast intensity with the National Hurricane Center official best track data as well as comparing the GFDL vertical shear with the AVN global analysis. Deviations in the GFDL intensity and vertical shear from the analysis data were considered to represent forecast error. These errors were then analyzed further by comparing the GFDL model forecast environmental wind field with a suite of observed data including GOES-8 satellite-derived winds, NOAA G-IV dropwindsondes, and upper-air observations supplemented by the GFDL initial analysis (F00).

Results indicate that errors in vertical shear were nearly coincident with deviations in observed intensity versus forecast intensity. These deviations were primarily the result of a misrepresentation of the upper-level flow in the model due to an overdeveloped downstream upper-level ridge. Additionally, an erroneous anticyclone developed over the model storm in several cases, resulting in significant weakening of the upper level westerly flow and

associated vertical shear. In this case, the downstream anticyclone was more intense and closer to the storm in nearly all simulations analyzed.

These findings are similar to previous studies where a storm to environment interaction has been identified as the result of redistribution of latent heat release due to convection and the downstream advection of the associated low Potential Vorticity (PV) outflow. The misrepresentation of convection and the associated effects on the surrounding environment is identified as the primary factor for both track and intensity forecast errors by the GFDL model during Debby.

An Analysis of Hurricane Debby (2000) and the Impact of Vertical Shear on the  
GFDL Forecast Performance.

by  
Jamie R. Rhome

A thesis submitted to the Graduate Faculty of North Carolina State University in  
partial fulfillment of the requirements for the Degree of Master of Science

Atmospheric Sciences

Raleigh, North Carolina  
2002

Approved By:

---

Chair of Advisory Committee

*Dr. Sethu Raman*

---

Member of the Advisory Committee

*Dr. Gary Lackmann*

---

Member of the Advisory Committee

*Dr. Al Riordan*

## BIOGRAPHY

Jamie Robert Rhome was born on June 21, 1976 in South Hill, Virginia. Although born in Virginia, he spent the vast majority of his youth in North Carolina being raised in a small city called Roanoke Rapids. He attended a small Christian academy called Halifax Academy from kindergarten through high school. Upon graduation from high school, he relocated to Raleigh, North Carolina, where he attended North Carolina State University (NCSU) and received a Bachelor of Science degree in Meteorology in 1998. Jamie also worked part-time and summers with the United States Environmental Protection Agency on matters related to long-range transport of agricultural based pesticides and the formation of ground level ozone. Jamie was later accepted to graduate school at NCSU where he studied the climatology of North Carolina under the direction of Dr. Sethu Raman. Jamie was offered a full-time position with the Tropical Prediction Center/National Hurricane Center (NHC) in Miami one year into his Masters of Science (MS) degree, and he relocated to Miami in September of 1999. He continued to work part-time on his MS degree while working at NHC and graduated in the fall of 2002.

## ACKNOWLEDGEMENTS

Given that the completion of this work was done remotely while working full-time at the Tropical Prediction Center/National Hurricane Center and spanned nearly four years, many people are deserving of recognition for their assistance, support, and encouragement. First and foremost, I wish to thank many people at North Carolina State University and the Department of Marine, Earth and Atmospheric Sciences for allowing me to complete this work remotely at the Tropical Prediction Center. Specifically, I wish to thank my advisor, Dr. Sethu Raman, for his guidance and being so flexible/understanding of the limitations/obstacles involved in finishing the degree while working full-time. Additionally, I wish to acknowledge the thoughtful comments and guidance by co-committee members Dr. Gary Lackmann and Dr. Al Riordan. My classmates and friends are thanked for their help and support during my years at NCSU.

My family is acknowledged for their moral and financial support and for always being supportive of my desire to continue higher education. Very few conversations were had without the inevitable question “how is the thesis coming?”

Many people at the Tropical Prediction Center have made significant contributions and provided assistance in this work. First and foremost, I wish to thank Chris Sisko for his computing expertise and unwavering support especially during the most difficult times. He never ever let me give up. I wish to also acknowledge the outstanding efforts of Dr. Richard Knabb whose enthusiasm and encouragement was extremely motivational. Moreover, he provided numerous suggestions and comments that proved instrumental in formulating the final conclusions. Others deserving recognition: Dr. Richard Pasch for several fruitful conversations regarding Hurricane Debby and vertical shear, Michelle Mainelli for providing assistance with writing scripts and general Unix support, Fiona Horsfall for providing the NOAA G-IV data, Bill Frederick for help with Gempak, and Robbie Berg for assistance with editing and format of the thesis. I wish to also thank my coworkers for their patience and understanding during this long and at times painful process.

Mark DeMaria of NOAA/CIRES and Chris Velden of CIMSS/University of Wisconsin are both acknowledged for many conversations and helpful suggestions.

Finally, I want to acknowledge Dr. Ellen Cooter of NOAA/ARL for giving me my first shot at research and providing me the knowledge and confidence which laid the foundation for all progress and success to date. She remains my mentor and friend, and I could never express in words how pivotal her contributions were in helping me pursue a dream.

# Table of Contents

<b>List of Tables</b>	<b>vii</b>
<b>List of Figures</b>	<b>viii</b>
<b>1) Introduction</b>	<b>1</b>
1.1) Purpose and Objective	1
1.2) Literature Review	3
1.2.1) Oceanic Influence	3
1.2.2) Upper-level Synoptic Environment	7
1.2.3) Vertical Shear	8
1.2.4) Relative Eddy Angular Momentum Flux	11
1.2.5) Potential Vorticity	14
1.2.6) Outflow/Divergence	16
1.2.7) Inner Core Dynamics	18
1.2.8) Land Interactions	21
1.2.9) Literature Review Summary	25
1.3) Case Study Synopsis	26
<b>2) Data</b>	<b>29</b>
2.1) Observed in-situ data	29
2.2) Satellite data	30
2.2.1) GOES Imagery and Passive Microwave Data	30
2.2.2) Quikscat	31
2.2.3) GOES Satellite Derived Winds	32
2.2.4) MPI and Topex/ERS-2	33
2.3) GFDL Numerical Model	33
<b>3) Methodology</b>	<b>36</b>
<b>4) Results</b>	<b>40</b>
4.1) Observational Analysis	40
4.1.1) Synoptic Analysis	40
4.1.2) Oceanic Influence	44
4.1.3) Low-level Inflow and Moisture	44
4.1.4) Satellite Analysis	46
4.1.5) Observational Summary	47
4.2) GFDL Model Analysis	50
4.2.1) Introduction and Overview	50
4.2.2) Initialization	50
4.2.3) Forecast	51
<b>5) Summary and Conclusions</b>	<b>60</b>
<b>6) References</b>	<b>64</b>



## List of Tables

<b>Table 1.</b> Official track forecast errors for Debby (2000) in nautical miles with number of forecasts in parenthesis.	<b>2</b>
<b>Table 2.</b> Official National Hurricane Center best track for Debby 2000 August 19-24 (from Pasch 2000).	<b>27</b>

## List of Figures

- Figure 1.** Official National Hurricane Center best track for Hurricane Debby August 19-24, 2000. 2
- Figure 2.** Comparison of the 72-hour forecasts (12 hour points) for UKMET (orange), AVN (green), NOGAPS (red), Clipper (pink), and GFDL (yellow) initialized 1200 UTC 22 August along with the official NHC best track (white) from 1200 UTC 22 August through 1200 UTC 24 August. 2
- Figure 3.** Time series of minimum central pressures for the cases with constant easterly flow of 3.5, 5, 10, and 15 m s<sup>-1</sup> shear, and no large-scale flow. The vertical line at t = 48 h is shown to mark the time at which the environmental fields are changed to introduce the shear or zonal flow (from Frank and Ritchie 2001). 11
- Figure 4.** NHC 72-hour forecast from August 22 1200 UTC. Black hurricane symbols indicate past track. Red hurricane symbols indicate forecast locations in 12-hour increments. Green, blue, and red lines indicate radius of 63, 50, and 34 knot winds respectively. Dash blue line indicates area of avoidance. 27
- Figure 5.** One-kilometer GOES-8 Visible satellite imagery on August 23 1545 UTC. Tip of arrow indicates location of low-level circulation. 28
- Figure 6.** Four-panel display of 200 mb wind (kt)/150 mb divergence (10<sup>-6</sup>s<sup>-1</sup>) (panel A), 200/850 mb shear streamlines/speed (kts) (panel B), 200 mb streamlines/speed (kt) (panel C), 200 mb wind/relative vorticity (10<sup>-5</sup>s<sup>-1</sup>) (panel D) for August 22 2000 1200 UTC. Tip of arrow indicates approximate location of the center of Debby. 41
- Figure 7.** Time series analysis of CIMSS vertical wind shear (knots) versus intensity (knots) for Debby (2000). A trend analysis is also shown for vertical shear using a six-degree polynomial function. Horizontal axis denotes time (tick mark equals 6 hrs) from August 19 1800 UTC through August 24 1200 UTC. 41
- Figure 8.** Same as in Figure 6 except for August 22 2000 1800 UTC. 41
- Figure 9.** Same as in Figure 6 except for August 23 2000 0000 UTC. 42
- Figure 10.** Same as in Figure 6 except for August 23 2000 1200 UTC. 42
- Figure 11.** Same as in Figure 6 except for August 24 2000 0000 UTC. 43

- Figure 12.** Time series analysis of maximum potential intensity (MPI) (kts) versus mean sea level pressure (MSLP) (mb) for August 19 1800 UTC through August 24 1200 UTC. **44**
- Figure 13.** Topex/ERS-2 sea height anomaly (cm) analysis for August 22 2000. Warm colors indicate positive anomalies, and cool colors indicate negative anomalies. **44**
- Figure 14.** SeaWinds scatterometer surface winds (10 m) over Debby on August 22 2000 (panel A) and SSM/I 22 GHz low-level vertical integrated water vapor (panel B) at 1400 UTC August 23 2000. For panel A, times (GMT) are denoted at bottom of image and correspond to time when right edge of swath passes 25N. Black barbs indicate rain contamination. For panel B, cool colors indicate drier air. Tip of arrow indicates approximate location of Debby at 0000 UTC 23 August 2000 (panel A) and 1200 UTC 23 August 2000 (panel B). **45**
- Figure 15.** 925 hPa storm-relative flow for 0000 UTC 23 August (panel A) and 0000 UTC 24 August (panel B). Gray wind barbs denote upper air soundings. Black wind barbs denote NOAA G-IV dropsondes with text indicating time of dropsonde in UTC (lower right) relative humidity in percent (lower left), temperature in Celsius (upper left), and geopotential height in meters (upper right). **45**
- Figure 16.** Hispaniola elevation contours (m). **45**
- Figure 17.** GOES-8 infrared satellite imagery at 0045 UTC 23 August (panel A), 1246 UTC 23 August (panel B), and 2145 23 August (panel C) along with SSM/I 85 Ghz at 0127 UTC 23 August (panel D), 1114 UTC 23 August (panel E), and 2229 UTC 23 August (panel F). Tip of arrow indicates approximate location of the center of Debby. **46**
- Figure 18.** Official NHC best-track (white line) for Debby (2000) versus 72-hour forecast track guidance (yellow line) from GFDL simulations (initialized 1200 UTC 22 August through 1800 UTC 24 August) indicating a consistent poleward bias. **50**

<b>Figure 19.</b> Official National Hurricane Center best track maximum sustained surface wind speed curve for Debby, 19-24 August 2000, and the observations on which the best track curve is based. AC denotes aircraft observations, which have been adjusted for elevation using 90%, 80%, and 85% reduction factors for observations from 700 hPa, 850 hPa, and 1500 feet, respectively. Drop denotes dropsonde observations which include actual 10 meter winds (sfc), as well as surface estimates derived from the mean wind over the lowest 150 meters of the wind sounding (LLM), and from the sounding boundary layer mean (MBL). Sat denotes satellite intensity estimates using Dvorak technique (adapted from Pasch 2000).	<b>50</b>
<b>Figure 20.</b> Comparison of the GFDL versus AVN initial vertical shear.	<b>51</b>
<b>Figure 21.</b> Time-series analysis of NHC best track intensity (knots), GFDL 72-hour forecast intensity (knots) initialized 0600 UTC 21 August 2000, AVN global analysis vertical shear (knots), and the GFDL 72-hour forecast vertical shear (knots) initialized 0600 UTC 21 August 2000. Time period extends from 0600 UTC 21 August (2000) through 0600 UTC 23 August (2000).	<b>51</b>
<b>Figure 22.</b> Time-series analysis of NHC best track intensity (knots), GFDL 72-hour forecast intensity (knots) initialized 1200 UTC 21 August 2000, AVN global analysis vertical shear (knots), and the GFDL 72-hour forecast vertical shear (knots) initialized 1200 UTC 21 August 2000. Time period extends from 1200 UTC 21 August (2000) through 1200 UTC 24 August.	<b>52</b>
<b>Figure 23.</b> Comparison of the 72-hour GFDL 200 hPa forecast winds (streamlines) initialized 1200 UTC 21 August (2000) versus satellite derived winds (wind barbs with cross), upper-air data (wind barbs with diamonds), and the GFDL analysis (wind barbs) valid 1200 UTC 23 August, 2000.	<b>52</b>
<b>Figure 24.</b> Time-series analysis of NHC best track intensity (knots), GFDL 72-hour forecast intensity (knots) initialized 1800 UTC 21 August 2000, AVN global analysis vertical shear (knots), and the GFDL 72-hour forecast vertical shear (knots) initialized 1800 UTC 21 August 2000. Time period extends from 1800 UTC 21 August (2000) through 1800 UTC 24 August.	<b>53</b>
<b>Figure 25.</b> Time-series analysis of NHC best track intensity (knots), GFDL 72- hour forecast intensity (knots) initialized 0600 UTC 22 August 2000, AVN global analysis vertical shear (knots), and the GFDL 72-hour forecast vertical shear (knots) initialized 0600 UTC 22 August 2000. Time period extends from 0600 UTC 22 August (2000) through 0600 UTC 25 August.	<b>54</b>

- Figure 26.** Comparison of the 36-hour GFDL 200 hPa forecast winds (streamlines) initialized 0600 UTC 22 August (2000) versus NOAA G-IV dropsondes (wind barbs with circles) satellite derived winds (wind barbs with cross), upper-air data (wind barbs with diamonds), and the GFDL analysis (wind barbs) valid 1800 UTC 23 August 2000. **54**
- Figure 27.** Comparison of the 48-hour GFDL 200 hPa forecast winds (streamlines) initialized 0600 UTC 22 August (2000) versus satellite derived winds (wind barbs with cross), upper-air data wind barbs with diamonds), and the GFDL analysis (wind barbs) valid 0600 UTC 24 August 2000. **54**
- Figure 28.** Time-series analysis of NHC best track intensity (knots), GFDL 72-hour forecast intensity (knots) initialized 1200 UTC 22 August 2000, AVN global analysis vertical shear (knots), and the GFDL 72-hour forecast vertical shear (knots) initialized 1200 UTC 22 August 2000. Time period extends from 1200 UTC 22 August (2000) through 1200 UTC 25 August. **55**
- Figure 29.** Comparison of the 12-hour GFDL 200 hPa forecast winds (streamlines) initialized 1200 UTC 22 August (2000) versus NOAA G-IV dropsondes (wind barbs with circles), satellite derived winds (wind barbs with cross), upper-air data (wind barbs with diamonds), and the GFDL analysis (wind barbs) valid 0000 UTC 23 August 2000. **55**
- Figure 30.** Comparison of the 24-hour GFDL 200 hPa forecast winds (streamlines) initialized 1200 UTC 22 August (2000) versus satellite derived winds (wind barbs with cross), upper-air data (wind barbs with diamonds), and the GFDL analysis (wind barbs) valid 1200 UTC 23 August 2000. **55**
- Figure 31.** Comparison of the 48-hour GFDL 200 hPa forecast winds (streamlines) initialized 1200 UTC 22 August (2000) versus satellite derived winds (wind barbs with cross), upper-air data (wind barbs with diamonds), and the GFDL analysis (wind barbs) valid 1200 UTC 24 August 2000. **55**
- Figure 32.** Time-series analysis of NHC best track intensity (knots), GFDL 72-hour forecast intensity (knots) initialized 1800 UTC 22 August 2000, AVN global analysis vertical shear (knots), and the GFDL 72-hour forecast vertical shear (knots) initialized 1800 UTC 22 August 2000. Time period extends from 1800 UTC 22 August (2000) through 1800 UTC 25 August. **56**
- Figure 33.** Comparison of the 36-hour GFDL 200 hPa forecast winds (streamlines) initialized 1800 UTC 22 August (2000) versus satellite derived winds (wind barbs with cross), upper-air data (wind barbs with diamonds), and the GFDL analysis (wind barbs) valid 0600 UTC 24 August 2000. **56**

- Figure 34.** Time-series analysis of NHC best track intensity (knots), GFDL 72-hour forecast intensity (knots) initialized 0000 UTC 23 August 2000, AVN global analysis vertical shear (knots), and the GFDL 72-hour forecast vertical shear (knots) initialized 0000 UTC 23 August 2000. Time period extends from 0000 UTC 23 August (2000) through 0000 UTC 26 August. **57**
- Figure 35.** Time-series analysis of NHC best track intensity (knots), GFDL 72-hour forecast intensity (knots) initialized 0600 UTC 23 August 2000, AVN global analysis vertical shear (knots), and the GFDL 72-hour forecast vertical shear (knots) initialized 0600 UTC 23 August 2000. Time period extends from 0600 UTC 23 August (2000) through 0600 UTC 26 August. **57**
- Figure 36.** Time-series analysis of NHC best track intensity (knots) versus vertical shear (knots) calculated from the AVN global analysis valid 1800 UTC 19 August 2000 through 1200 UTC 24 August 2000. A trend analysis is also shown for vertical shear using a six-degree polynomial function. Horizontal axis denotes time (tick mark equals 6 hours). **58**
- Figure 37.** Time-series analysis of NHC best track intensity (knots), GFDL 72-hour forecast intensity (knots) initialized 1200 UTC 23 August 2000, AVN global analysis vertical shear (knots), and the GFDL 72-hour forecast vertical shear (knots) initialized 1200 UTC 23 August 2000. Time period extends from 1200 UTC 23 August (2000) through 1200 UTC 26 August. **58**
- Figure 38.** Time-series analysis of NHC best track intensity (knots), GFDL 72-hour forecast intensity (knots) initialized 1800 UTC 23 August 2000, AVN global analysis vertical shear (knots), and the GFDL 72-hour forecast vertical shear (knots) initialized 1800 UTC 23 August 2000. Time period extends from 1800 UTC 23 August (2000) through 1800 UTC 26 August. **59**

## Chapter 1 Introduction

### 1.1) Purpose and Objective

According to a recent study on hurricane damage by Pielke and Landsea (1998) tropical cyclones (TC) are the costliest natural disasters in the United States (U.S.). This has been particularly manifested in the last few decades as population growth trends in coastal and near coastal regions has increased significantly (Sheets 1990). As a result, the U.S. is now more vulnerable to TC than ever before (Marks et al. 1998). While damage has risen substantially, deaths attributable to TC have shown a decreasing trend (Sheets 1990). Still, as coastal population density increases, it is necessary to provide more timely and accurate predictions to facilitate evacuations with increasing clearance times. Accordingly, the research community has responded by focusing on the increased understanding of tropical cyclone movement and improving forecast track accuracy.

Less emphasis has been placed on the improved understanding of intensity and structural changes of TC. As a result, systematic and skillful intensity forecasting techniques have yet to be developed, and much is still not understood about TC intensity change (Fitzpatrick 1996, Elsberry et al. 1992). The annual averages of the 1990-1997 Atlantic basin intensity forecast errors show no significant improvement over the period (Avila 1998). Additionally, DeMaria (1997) showed that intensity forecasts are only about half as skillful as the TC track forecasts, and TC intensity forecasts beyond 36 hours show little improvement over climatology and persistence. This lack of skill is attributable in part to the lack of intensity forecast models that are not based solely on climatology and persistence (Kaplan and DeMaria 1998).

To address the need for improved dynamical TC intensity guidance, a three-dimensional dynamical TC model has been developed at the Geophysical Fluid Dynamics Laboratory (GFDL) to provide both track and intensity forecasts. The National Weather Service incorporated this model operationally in 1995. Since its introduction, the GFDL model has become one of the more heavily utilized intensity forecasting tools available operationally to the Tropical Prediction Center (TPC). However, Lawrence and Gross (1994) and Kurihara et

al. (1998) showed that the GFDL intensity forecasts were not skillful as compared with the traditional persistence and climatology models, especially in cases of rapid changes in intensity.

The difficulty in forecasting rapid intensity change is especially challenging and was recently highlighted by the unexpected weakening of Hurricane Debby along the northern coast of Hispaniola on August 23, 2000 (Figure 1). Debby moved across the northeast Caribbean Sea making landfall near Barbuda and later near St. Barthelmy in the British Virgin Islands. Debby caused minimal damage; however, heavy rains occurred over Puerto Rico as the center moved north of the island, indirectly resulting in one death. While Debby's impact was not substantial, several GFDL runs suggested that Debby would move more poleward and intensify, becoming a significant threat to southeast Florida. In actuality, Debby dissipated harmlessly over the northern Caribbean Sea just south of Cuba. The GFDL model track guidance was not uniquely inaccurate. In fact, the GFDL track guidance remained near the center of the forecast swath associated with other numerical guidance used at TPC. An example is given in Figure 2 showing the forecasts associated with TPC operational numerical guidance initialized on 22 August 1200 UTC. Similarly, Table 1 shows the forecast errors associated with several of the more commonly used operational models at TPC. While the GFDL track forecast errors were comparable with other numerical guidance, intensity errors were nearly double that of the 2000 season average. These errors are highlighted by the fact that the GFDL track forecasts consistently indicated an increasing threat to the south Florida region, especially as the storm passed through the northeast Caribbean and moved north of Puerto Rico. The increasing threat of a dangerous hurricane prompted authorities in the Florida Keys to initiate evacuations of all non-residents given the lengthy time required for evacuation processes in that region. This resulted in a significant loss of tourism revenue.

Even though Debby never struck the continental United States and dissipated harmlessly in the western Caribbean Sea, she provided an overwhelming reminder of the limitations of TC intensity forecasting. It is therefore necessary to improve dynamical intensity guidance for rapidly evolving TC. Given that the GFDL model represents the most state of the art purely dynamical operational model available to NHC, a comprehensive analysis of the

GFDL forecast output for cases of rapid intensity change is the logical first step towards improving the model performance. This is the motivation for the present work, which presents a detailed analysis of Debby (2000) as well as an analysis of the operational GFDL forecasts. This will be accomplished in two parts: 1) a comprehensive case study utilizing operationally available data to determine the major environmental factors responsible for the weakening of Debby and their relative importance, and 2) analysis of the operational runs of the GFDL to determine if those features found prevalent in the case study were appropriately analyzed and/or forecast by the model. This paper begins with a literature review of research dealing with environmental factors in tropical cyclone (TC) weakening/intensification. A case study of Debby is then presented focusing on the time period when Debby's weakening was most rapid. An analysis of the GFDL model simulation of Debby is then presented with emphasis on the most salient features found within the case study. Finally, conclusions from the case study and model analysis are presented with emphasis on possible real-time implications of model initialization and forecast error.

## 1.2) Literature Review

TC intensity change is difficult to forecast because it involves complex interactions between upper-oceanic heat content, inner core atmospheric dynamics, land interactions and synoptic scale environmental conditions. These interactions can occur over various temporal and spatial scales and they can act alone or simultaneously with other processes. There has been increasing research interest regarding TC intensity and structural changes and the responsible environmental factors. This section provides a historical perspective as well as some of the more recent research involving TC intensity change. The factors discussed are important to establish for the analysis of the current case study presented in later sections.

### 1.2.1) Oceanic Influence

The ultimate source of energy for a TC is the ocean, which provides latent and sensible heat exchange. As air cyclonically converges into the center, it experiences a decrease in pressure that causes cooling due to adiabatic expansion. However, in the presence of warm

sea surface temperatures (SST), sensible heat flux allows the air parcel to preserve most of its temperature and counteracts this cooling. Lowering the surface pressure while holding the temperature constant leads to an increase in equivalent potential temperature which is ultimately transported aloft within updrafts of the deep eyewall convection. This heat source warms the upper levels and lowers the surface pressure resulting in stronger surface convergence.

Palmen (1948) was one of the first to recognize the relationship between warm SST and TC development. He noted that the critical threshold of SST for TC development is approximately 26.5° C. Additionally, Kleinschmidt (1951), Riehl (1954), and Merrill (1987) further established the importance of air-sea interaction by examining the climatology of storm intensity and SST. They showed that the most intense storms typically occur over regions of the ocean with the highest SST. However, more recent research has noted that SST alone cannot account for the total variation in TC intensity and is a poor indicator of whether an individual TC will intensify. For example, DeMaria and Kaplan (1994) compared Tropical Storm Earl (1992) and Hurricane Bonnie (1992). Earl's maximum sustained surface winds (mssw) reached 28 ms<sup>-1</sup> with a SST of 27°C and Bonnie's mssw reached 49 ms<sup>-1</sup> with a SST of about 25°C. Merrill (1987) also noted that the presence of high SST was necessary but not sufficient for intensification.

Traditionally SST has been used to diagnose the available potential energy from the ocean surface. While it is widely accepted that a warm underlying ocean is the primary energy source for a TC, the redistribution of energy within the TC is not well understood. However, some upper bound exists in the potential intensity for an individual storm based on the available potential energy within the underlying ocean. The upper bound is based on thermodynamic limits given available energy from the ocean and dissipative processes. Miller (1958) was one of the first to establish an upper bound theory based upon lifting an air parcel moist adiabatically to the tropopause level in the eyewall and then allowing dry adiabatic subsidence back to the surface. The resulting minimum surface pressure defined the maximum potential intensity (MPI). This method is sensitive to the selection of surface moist entropy and the entrainment into the eye, and it assumes a constant surface relative humidity of 85%. Conversely, Malkus and Riehl (1960) calculated the MPI by estimating

the along-parcel trajectory energy necessary to balance surface momentum loss. Unlike Miller (1958), they concluded that pressure falls are not entirely due to subsidence and that the redistribution of near-surface moist entropy in the vertical through convective mixing could cause pressure falls within the eye. Emanuel (1986) further expanded this idea by assuming the TC acts as a Carnot heat engine. This method uses an exact equation governing the maximum sustainable central pressure of a hurricane using the Carnot cycle. Inflow within the boundary layer acquires entropy from the ocean, then ascends and gives off heat in the lower stratosphere/upper troposphere. Net heating from this cycle negates the effects of friction by self-induced circulations resulting in higher fluxes. Emanuel (1988, 1991) later refined this model by including the effects of moist thermodynamics. However, Emanuel's model lacks an eye and assumes 100% relative humidity in a cloud-filled cyclone core (Holland 1997).

More recently, Holland (1997) expanded upon the work of Miller (1958) by using a purely thermodynamic approach to derive MPI. This method is based on hydrostatic pressure falls resulting from entropy changes above 500 hPa and on the establishment of an upper-tropospheric warm core. Holland (1997) and Miller (1958) used only thermodynamic approaches while Malkus and Riehl (1960) and Emmanuel (1986, 1988) combined thermodynamic and dynamic approaches. Tonkin et al. (2000) evaluated the performance of the two most recently developed MPI models (Emanuel 1988, 1991 and Holland 1997). In general, both models provide reasonably similar estimates of potential TC intensity. However, they both appear to underestimate MPI, especially at lower SST values. Both models produce significantly greater intensities than the actual observed storm intensity at lower SST values, which suggests that warmer SST may play an increasing role in intensity. Stronger storms aided by the higher SST values may be more resistant to other detrimental environmental influences. Additionally, Holland's model provides reasonable seasonality but underestimates the early and late season MPI in certain areas (Tonkin et al. 2000). Conversely, Emanuel's model shows poor seasonality with intense TCs during winter months (Tonkin et al. 2000).

Storms seldom reach their MPI (Miller 1958, Emanuel 1991) due to other factors working against TC development. Available energy from the ocean determines the upper bound or

maximum intensity, whereas the surrounding environment determines how closely the TC approaches its upper bound. DeMaria and Kaplan (1994) used an empirical relationship based on 31 years of data between SST and maximum intensity to develop a method for determining the probabilities of a given storm reaching the MPI. They showed that only 16% of Atlantic TCs reach 80% of their MPI. This is due in part to the fact that existing MPI estimates only incorporate the SST as an indication of the upper-ocean heat content and further establishes that SST alone is not a sufficient indication of TC intensification. SST only represents the temperature of a thin layer typically less than a few centimeters thick that mixes with the underlying water as the winds increase beyond  $5 \text{ ms}^{-1}$  (Shay et al. 1998). Winds of  $5 \text{ ms}^{-1}$  typically extend well out from the center of a mature TC, thus higher SST could be mixed with cooler temperatures from below well before the TC arrives. The importance of the underlying oceanic structure and vertical temperature profile in TC development has been documented by many sources (Dunn and Miller 1960, Perlroth 1967, 1969, Leipper and Volgenau 1972).

The role of upper-ocean heat content in TC intensification has recently gained more attention due to advanced remote sensing platforms such as AVHRR and TOPEX/ERS. In particular, studies have shown that Opal (1995) was affected by a warm eddy only faintly discernible based on SST alone due to uniformly distributed temperature values (Black and Shay 1998, Shay et al. 1998, 2000). The use of altimeter data onboard the NASA Oceanographic Topography Experiment (TOPEX) mission helped detect the presence of a warm eddy along the path of Opal. Additionally, their results showed that the warm eddy was partly responsible for the rapid intensification. Moreover, the extraction of heat content prior to Opal traversing the warm eddy showed a decrease in heat content by a factor of more than two as a result of Opal's track over the eddy. This may have enhanced air-sea exchange, which aided the rapid burst of convection and subsequent intensification of Opal (1995) through enhanced surface fluxes.

This conclusion has been verified by several numerical studies. For example, Hong et al. (2000) used a three-dimensional coupled numerical model to quantitatively study the mutual interaction between Opal (1995) and the ocean. Additionally, this study used numerical simulations from the GFDL Modular Ocean Model to represent the initial state of the ocean

during the rapid intensification of Opal (1995). Results indicate that stronger fluxes caused by Opal's track over a warm core ring accounted for 60% of the observed pressure fall during rapid intensification. Moreover, a similar simulation was generated where the warm core ring was removed. The results from this simulation showed a pressure fall of 7 hPa as opposed to 17 hPa with the warm core ring included, thus indicating that intensification was a response to both atmosphere and ocean processes. However, based on this study the relative role of the ocean appears to dominate over that of the atmosphere.

Conversely, Krishnamurti et al. (1998) utilized numerical simulations to conclude that the warm eddy may have enhanced convection but did not appear to be crucial for intensification. However, the coarse grid spacing (75-km) of the global model may not have been able to fully capture smaller scale features such as the warm eddy traversed by Opal. Additionally, Krishnamurti et al. (1998) only utilized SST in diagnosing the role of the warm eddy. In a more recent study, Bosart et al. (2000) showed that the overall intensification of Opal was a function of both atmospheric and oceanic factors. However, atmospheric forcing played a more important role during the onset of rapid intensification. A convective burst was observed about 9 hours prior to the center of Opal traversing the warm eddy. Intensification began approximately 3 hours prior to the center of Opal being over the warm eddy. Despite the fact that trajectories from the warm core may enter/affect the eye prior to the eye moving over the eddy, the time lag was too large for the warm core to be directly responsible for the onset of intensification. However, a second intensification ( $52 \text{ ms}^{-1}$  to  $68 \text{ ms}^{-1}$ ) period coincides with the eye moving over the warm eddy. Thus, they concluded that this second portion of intensification was more directly related to the warm eddy

### 1.2.2) Upper-level synoptic environment

The upper-level anticyclonic outflow associated with a TC has been shown to be less dynamically stable and less resistant to environmental flow than the cyclonic flow in the lower to middle layer of the TC (Black and Anthes 1971 and Holland and Merrill, 1984). Many studies have investigated the role and interaction of the upper-tropospheric synoptic environment with TC development. Much of this research has focused on the relative role of physical mechanisms that potentially strengthen or weaken a TC (e.g. inward flux of cyclonic

eddy angular momentum, enhanced outflow/jets, divergence aloft, potential vorticity (PV), and vertical wind shear). Despite establishing a link between the upper level synoptic environment and TC intensity, the relative roles of these physical processes are not clearly understood. Moreover, these processes can act concurrently or individually and can affect the storm at different times during its life cycle further complicating their roles. Despite these uncertainties, the mechanisms are typically most prevalent during interactions with upper-level troughs. It is generally accepted that the most favorable position of the trough is northwest of the TC (Sadler 1976), a location that enhances divergent outflow without producing deep strong shear over the TC.

Much of the existing knowledge regarding the role of upper-level flow has come from composite analysis and numerical simulations due to the upper-level data sparsity over open water. Composite analysis has provided significant insight into the overall TC model but limited knowledge into sub-synoptic scale motions and properties. The underlying philosophy behind composite analysis is to overcome data limitations by averaging multiple data sources from similar storms at many times in order to facilitate quantitative measurements, especially vertical profiles. While this method provides insight into large-scale features, it suffers from data smoothing. Similarly, the lack of upper-level observations hinders the direct verification of model-simulated structure. Despite data limitations, these methods have yielded an overall model of the interaction of a TC with upper level features. The following sections will discuss various research on each of these environmental features.

### 1.2.3) Vertical Shear

It has long been accepted that weak or no vertical shear is a necessary condition for the development of a TC. These ideas were first acknowledged in the late 1800's to early 1900's based on observations of upper-level clouds. Observational studies became possible with the advent of upper-air networks and confirmed the importance of environmental flow relative to a tropical storm or disturbance (Ramage 1959 and Gray 1968). More recent observational studies have cited strong vertical shear as an inhibiting factor in TC development (Case and Gerrish 1984; Merrill 1988; Pasch and Avila 1992). Even though these observational studies

noted the importance of vertical shear, they provided little or no insight into the physical mechanisms and structural changes that result within the TC.

The most common explanation of the effects of vertical shear on a TC is ventilation (Gray 1968). Gray used upper-air observations over the tropical oceans to study the relationship between various parameters and intensity. He concluded that vertical shear results in a decoupling of the warm anomaly aloft from the surface, thereby inhibiting intensification. The latent heat of condensation aloft is advected away from the TC center causing the surface pressure to rise and a reduction in sea level pressure gradient across the storm. Madala and Piacsek (1975) expanded upon this idea by using a three-layer model to show that the warm core is smaller when strong shear is included in the simulation. They conclude that shear was responsible for the advection of heat in a similar manner as Gray (1968).

However, limitations to the Gray (1968) argument have been identified. Energy aloft is generally dispersed by gravity waves, which typically have phase speeds larger than advective speeds of the upper-level environmental flow. Therefore, the inclusion of shear should have little effect on the dispersion of upper-level energy (DeMaria and Huber 1998). Based on this argument, the data utilized by Gray (1968) and early modeling attempts may not have been sufficient to capture some of the mesoscale processes involved in the response of the TC to vertical shear. Another limitation of Gray's argument is that strong vertical shear may actually decrease static stability of the atmosphere by advecting the warm anomaly aloft away from the low-level center. This was proposed by DeMaria (1996) by using a simple two-layer diagnostic model to conclude that shear causes the potential vorticity associated with the TC to become tilted in the vertical resulting in a mid-level temperature perturbation near the vortex center. The mid-level warming reduces vertical instability and possibly suppresses convective activity associated with the TC. DeMaria and Huber (1998) expanded upon this by using the GFDL model to simulate Hurricane Isidore (1996) in a highly sheared environment. The GFDL model included advanced parameterization and increased horizontal/vertical resolution as compared to models used in earlier numerical studies. Moreover, the 3-way nested model includes a vortex replacement strategy with the specified vortex more capable of representing the asymmetric mesoscale structure of the TC. Therefore, the GFDL model should represent a more realistic

representation of the mesoscale response of vertical shear than the earlier composite analysis. Results from this study confirm that the shear induced tilting of the TC resulted in a mid-level temperature perturbation. While stabilization associated with the warm anomaly could not be isolated as the dominant process in weakening, it was hypothesized that a reduction in convection near the core may result due to increased vertical stability. These results are quite different from the traditional ventilation conceptual model provided by Gray (1968). However, the modeling results of DeMaria (1996) and DeMaria and Huber (1998) may better represent both thermodynamic and dynamic mesoscale processes within the TC.

Additional theories have been proposed regarding the dynamic/thermodynamic response of the inner vortex to shear. Flatau et al. (1994) used a three-dimensional primitive equation model to study vortex tilting caused by vertical shear by utilizing PV for analysis of the effects of shear. The results showed that a secondary circulation arises due to vortex tilting with a flow through the center of the upper-level PV anomaly that causes the lower-level PV anomaly and upper-level PV anomaly to rotate around each other. Conversely, Tuleya and Kurihara 1981 and Bender 1997 provide an explanation of the effects of shear using a vorticity stretching and compression argument. Tuleya and Kurihara (1981) used an eleven-level primitive equation model to simulate a TC, and Bender (1997) used the GFDL model to simulate Gilbert (1988). These studies also noted that shear results in a tilting of the inner vortex; however, they focused more on near-surface asymmetries as opposed to mid-level temperature anomalies. Also, these methods focused more on the comparison of easterly versus westerly shear. The results from these studies suggest that genesis is more likely in easterly shear as opposed to westerly shear. Additionally, vertical shear was shown to affect the vertical velocity and precipitation patterns relative to the center. Vertical shear-induced stretching of vorticity generates asymmetric near-surface convergence/divergence patterns. In the simulation with easterly shear, convergence was found in the front of the storm and divergence in the rear (with respect to the direction of storm motion). Easterly shear creates a net inflow in the front quadrant of the storm resulting in increased convergence. This results in increased convection ahead of the storm and decreased convection toward the rear relative to the motion, thus favoring development for a westward moving TC. Frank (1998) found similar results using composite initial conditions from McBride and Zehr (1981) to

simulate the response of a tropical depression-like vortex to various environmental flows. They showed that the environmental flow and vertical shear affects the patterns of vertical velocity and organization of latent heat release. Based on these results, vertical shear appears to affect near surface more than middle level relative flow.

More recently, several studies have suggested that a time lag exists between the onset of vertical shear and weakening (Frank and Ritchie 2001 and Gallina 2002). Frank and Ritchie (2001) used numerical simulations of TCs to show that time lags exist between the imposition of the large-scale shear and the resulting rise in the minimum central pressure. The time lag is a function of the magnitude of the imposed vertical shear ranging from a few hours under strong shear ( $15 \text{ ms}^{-1}$ ) to 36 hours under weaker shear ( $5 \text{ ms}^{-1}$ ) (Figure 3). Similarly, Gallina (2002) found analogous results in a study utilizing satellite-derived winds. The results of this study suggest an inverse relationship between shear and intensity with a time lag of 12-24 hours. Furthermore, this study showed that the time-lag relationship between shear and intensity is a function of the TC strength with larger/strong cyclones having a longer time lag.

It is generally accepted that the development of convection is limited if the tops are sheared off by strong winds aloft. The appearance of an exposed low-level circulation outside the convection is commonly used as operational evidence of shear and as an indication that weakening is occurring or intensification will be minimal (Dvorak 1984). Despite this evidence and the recent results from model simulations discussed earlier, the effects of vertical shear, especially on the inner core, remain unclear primarily due to limited data and the difficulty in modeling the dynamics of the inner core. While the physical mechanisms and mesoscale response of the inner vortex to vertical shear remain unknown, the detrimental effects to TC development have been established. Thus, vertical shear will be closely examined in the current case study on Debby presented in later sections.

#### 1.2.4) Relative eddy angular momentum flux

The basic idea behind relative eddy angular momentum (REAM) flux theory is that, when there is outflow aloft, mass continuity requires that there be a compensating lower to

middle level inflow. If the inflow has tangential momentum larger than the air leaving the center, the result is an inward flux of REAM. The presence of upper level outflow and outflow jets ensures that there will almost always be inward cyclonic momentum fluxes (Molinari and Vollaro 1989). Thus a TC approaching an upper-level trough typically experiences larger fluxes of REAM due to enhanced outflow. Based on this theory, an approaching trough modifies the upper level environment (enhanced outflow) with a resulting increase in REAM.

Several studies have noted the presence of large inward fluxes of REAM into the upper levels of an intensifying TC at outer radii. Anthes (1970) showed that these eddies could supply cyclonic angular momentum at outer radii of the TC. Additionally, Holland (1983) showed that these fluxes were confined mainly in the outflow layer. McBride and Zehr (1981) used composite analysis to compare developing and non-developing systems and found that non-developing systems contained weaker fluxes of REAM. Pfeffer and Challa (1981) used the composite data from McBride and Zehr (1981) to initialize a numerical model. Numerical simulations showed that REAM fluxes were more intense and organized for developing disturbances. Additionally, simulations of composite developing disturbances with and without REAM fluxes showed that the vortex fails to intensify without REAM fluxes.

Molinari and Vollaro (1989) used a different approach by analyzing outflow layer winds during the life cycle of Elena (1985) to investigate the role of REAM fluxes. They concluded that a high correlation exists between central pressure changes and REAM fluxes at outer radii. However, they also noted that a response lag existed, which they concluded represented an adjustment of the hurricane vortex. Molinari and Vollaro (1990) expanded upon these results by using model data to solve Eliassen's balanced vortex equation to study the response of the hurricane vortex to fluxes of angular momentum and heat. Their results show a band of upward motion with deep inflow and narrow outflow that shifted inward during the 24 hours prior to intensification. Momentum convergence forces axisymmetric outflow just below the tropopause with deep compensating inflow in the lower troposphere. The inflow is joined to the outflow by ascent, which destabilizes the column and enhances convective heat release (Willoughby and Black 1996). Challa and Pfeffer (1990) and Pfeffer

and Challa (1992) also used numerical models with composite initial conditions to show the importance of REAM fluxes. However, their explanation was somewhat different from earlier findings. They concluded that REAM fluxes could cyclonically spin up a TC by exerting a cyclonic torque on the vortex. This induces upper-level divergence and low-level convergence. These results are similar to the findings of Krishnamurti et al. (1998) who used a global spectral model to simulate the intensification of Opal (1995) and attributed intensification to reduction of the gradient in angular momentum above the region of maximum convective heating. This contributed to stronger cyclonic spinup of parcels entering the storm. Rogers et al. (1998) found similar results using the Special Sensor Microwave/Imager (SSM/I) to estimate the release of latent heat during Opal (1995) within the eyewall region. Results reveal at least two major episodes of elevated latent heat release, which they assumed was due to convective bursts. Using data from the ECMWF model, they show that the second convective burst (elevated latent heat release) coincided with high values of REAM fluxes.

Additional studies have cited the importance of REAM fluxes utilizing a more statistical/climatological approach. For example, Demaria et al. (1993) showed that for all named storms during the 1989-1991 seasons, one-third of the storms intensified just after a period of enhanced REAM. The ten storms with the largest intensity change were analyzed separately and six of the ten periods of rapid intensification were associated with enhanced REAM. In the remaining four cases the storm intensified in the absence of an upper-level trough. However, these results also included the effects of SST and vertical shear thus suggesting that REAM may act together with other environmental features and that REAM fluxes alone may not fully account for intensity variations. Since this method includes other factors over multiple storms, it may represent a more realistic representation of the relative importance of REAM fluxes in TC intensification. Individual storms may be dominated by one forcing mechanism and therefore highlight the importance of REAM fluxes.

Despite these findings, there is still uncertainty involving the relative importance of REAM fluxes on TC intensification. REAM fluxes may enhance the deepening or just reflect turbulent mixing from enhanced convection resulting in momentum and heat perturbations. Merrill and Velden (1996) showed that Typhoon Flo (1990) was influenced by REAM fluxes

just after peak intensification. They observed a decrease in minimum central pressure and increase in maximum winds before REAM fluxes affected the TC. Similarly, Ooyama (1982) showed that REAM fluxes might actually represent that intensification is occurring as opposed to a precursor. Moreover, several studies have noted that REAM is not important in rapid intensification. For example, Merrill (1988) concluded that the beneficial impacts of REAM are offset by the increased vertical shear and that momentum fluxes are a poor index of intensity change. DeMaria and Kaplan (1994) showed 200 hPa fluxes of REAM for rapidly intensifying TCs were not substantially different than the sample mean. Similarly, Landsea et al. (1998) showed that high rates of intensification could occur in the absence of upper-level angular momentum fluxes. Based on these findings, REAM fluxes may be less important during rapid intensification.

#### 1.2.5) Potential Vorticity

Another hypothesis concerning superposed potential vorticity (PV) anomalies associated with upper-tropospheric troughs has also been proposed. Traditionally, PV has been used as an analysis tool in mid-latitude cyclones. However, PV analysis has recently gained popularity among scientists in diagnosing the structure of a mature TC. The primary advantage of PV is its conservative nature in adiabatic frictionless flow therefore allowing unambiguous identification of diabatic processes. Upper-troughs produce a positive vorticity anomaly aloft and increased vertical shear. Vertical shear associated with a PV anomaly is zero directly below the anomaly increasing to large values at outside radii (Thorpe 1986). As a TC approaches an upper-trough and PV anomaly, it experiences an increase in vertical shear until the anomaly is directly superposed above the core of the TC.

The role of PV anomalies in TC intensification has typically been studied using numerical models due to data limitations (Molinari et al. 1995, 1998). The results of these studies have yielded two explanations for TC intensification. The first involves the interaction between the upper-level positive PV anomaly associated with the trough and the negative PV anomaly associated with the outflow layer of the TC. The interaction allows perturbation energy to grow at the expense of mean vertical wind shear. This causes the positive PV anomaly

associated with the trough to weaken as it approaches the TC thus reducing the overall strength, depth, and duration of vertical shear. Additionally, the enhanced divergence typically associated with an upper-level trough may enhance convection, which provides additional heating aloft. The enhanced heating produces lower PV aloft further offsetting the negative effects of vertical shear. Another explanation is that the interactions of PV anomalies initiates the evaporation-wind feed back instability (WISHE) proposed by Emanuel (1986) by enhancing surface circulations and fluxes. This explanation is somewhat similar to that proposed by Montgomery and Farrell (1993). They used two and three-dimensional moist geostrophic momentum models to investigate the role of upper-level PV anomaly. They concluded that the process of intensification was similar to that of mid-latitude systems where the superposed PV anomalies caused a low-level spinup through vortex stretching and enhanced convergence.

Despite these findings, the above conceptual models involve a complex interaction among environmental factors of varying scales. Thus it is difficult (from a forecast perspective) to determine if the overall outcome will produce a stronger or weaker TC. Moreover, divergence ahead of the large-scale trough may enhance convection and heating aloft. This may act to prevent or at least limit the detrimental effects of increased vertical shear by weakening the positive PV anomaly associated with the trough. This could result in an overall intensification of a TC as it interacts with a trough despite an increase in vertical shear due to the positive effects dominating the negative effects. The positioning of the trough in relation to the TC strength/structure appears to dictate whether the overall interaction results in weakening or intensification. If the trough is positioned in such a way as to enhance convective activity, the increased heating could result in lower PV aloft over the cyclone. This may act to offset some of the detrimental effects of increased vertical shear. However, if the trough interaction is not favorable for intensification, the increased vertical shear may result in an overall weakening.

The role of PV appears to be equally important for developing as well as mature TCs. Molinari et al. (1995) investigated the role of PV during the intensification of Hurricane Elena (1985) and Molinari et al. (1998) on a weak tropical storm Danny (1985). Both studies linked the intensification to PV anomalies. Therefore, the ability of the TC to modify the

approaching trough and associated PV is not a function of the TC strength prior to the interaction. Research in this area has been plagued by a lack of upper-level data surrounding a TC during intensification. Additionally, this type of research suffers from the lack of PV analysis in real tropical systems (Shapiro and Franklin, 1995) thus providing little ground truth to compare modeling results.

#### 1.2.6) Outflow/divergence

Upper-level outflow associated with TC is an important process for removing excess heat and sustaining convective instability. The overall outflow associated with a TC has been shown to be strongly influenced by mid-latitude troughs or tropical upper-tropospheric troughs (TUTT) if positioned favorably (Sadler 1976, Wu and Cheng 1999, Shi et al. 1997). Chen and Grey (1985) utilized data collected during the First GARP Global Experiment (FGGE) to construct 200 hPa composite patterns associated with TC intensification. Six patterns most likely to intensify a TC were identified. The most frequently observed pattern was an easterly moving mid-level trough on the poleward and westward side of the TC enhancing poleward outflow. Another pattern identified was the TC located at the tip or in the rear of a TUTT enhancing a single outflow channel. Chen and Grey (1985) also showed how anticyclones of the opposite hemisphere could enhance outflow acting alone or in unison with an upper tropospheric trough streamlines.

Many observational studies have shown that intensity tendencies of a TC are related to the strength of outflow jets/channels. Moreover, recent studies have proposed that upper-troughs may enhance/strengthen outflow jets associated with a TC. As a mid-latitude trough or TUTT approaches a TC, conditions may become more favorable for the development or strengthening of a poleward outflow jet (Chen and Grey 1985). If the flow associated with the trough or TUTT superimposes with the existing poleward outflow jet, the outflow jet is strengthened allowing increased ventilation. Studies have confirmed the existence of outflow jets and shown that convective activity is correlated with the channeling and/or strengthening of the outflow jets. Based upon this, Merrill (1985) concluded that the thermally direct secondary circulations associated with the outflow jets may increase convective activity near

the inner regions of a TC similar to jet streaks in midlatitude systems (Uccellini and Kocin, 1987). The ascending branch of the thermally direct circulation about the entrance region of the outflow jet provides enhanced vertical motions, which could strengthen or initiate convective activity. Rodgers et al. (1991) utilized satellite-measured total ozone to conclude that an increase in convection near the core of Irene (1980) was preceded by the formation of an outflow channel. Shi et al. (1990, 1997) used a numerical model to investigate the sudden burst of convection in TC Florence (1988) in relation to upper-level flow. They linked the convective growth and subsequent increase in intensity with the approaching upper-level trough and enhanced outflow jets. These findings are in good agreement with those of Bosart et al. (2000). They concluded that the rapid intensification of Opal (1995) was due to a complex interaction with a jet entrance region.

Additionally, the role of divergence aloft (often associated with enhanced outflow) has been studied in relation to TC development. McBride and Zehr (1981) used composite analysis over the Pacific and Atlantic to differentiate between developing and non-developing systems. They noted that divergence aloft was more pronounced in developing storms, and is most important for initial development. An existing system with sufficient divergence did not respond with an increase in divergence. This suggests that a TC is more responsive to the synoptic environment initially. As a TC nears maturity mesoscale processes play a more important role in intensification. Bosart et al. (2000) also investigated the role of upper-level divergence based on analysis of satellite derived cloud drift winds. The increased sensing capabilities of GOES 8/10 has allowed extraction of wind fields over multiple layers and cloud free areas (Velden et al. 1997), thus providing better spatial and temporal continuity. In a study on the rapid intensification of Opal (1995), Bosart et al. (2000) utilized high resolution water vapor winds and NCEP gridded data to show that a significant area of divergence occurred over Opal just prior to and during rapid intensification. They hypothesized that increased mid-level ascent enhanced convection and subsequent intensification of Opal. They further concluded that the first part of the rapid intensification of Opal was enhanced by the interaction with a trough tail/jet entrance region. The increased divergence associated with this feature helped to trigger the areal expansion of deep convection. One possible reason for the differences in McBride and Zehr (1981) and

Bosart et al. (2000) is that Bosart et al. (2000) used high-resolution data for an individual storm as opposed to composite data over multiple storms and times. The findings of McBride and Zehr (1981) represent large-scale divergence and may represent overall divergence associated with trough interactions rather than mesoscale processes such as jet dynamics. It is therefore possible that the findings of Bosart et al. (2000) represent a mesoscale interaction over a short period of time and may be a better representation of the interaction of upper-level flow on a TC.

Operational TC forecasting has been plagued by the complexity of trough interactions. The size, intensity, and proximity of an upper-level trough in relation to a TC are important factors influencing TC dynamics and intensity. Several studies have documented that a well-formed TC with a strong anticyclone aloft is resistant to external forces (Molinari et al. 1995 and Drury and Evans 1998). However, the term strong anticyclone is subjective. Is the strength based on the depth of the outflow layer or the overall divergence? There is still uncertainty as to whether an upper tropospheric trough will produce a favorable or unfavorable environment for intensification. The effects of one environmental factor may be shadowed by another factor. The complexity of scale interactions and even varying interactions among the physical mechanisms responsible for intensification make this a challenging and essential area for future research.

One limiting factor in research on upper-level outflow is that dense observational data of the outflow layer is rare due to the altitude limitations of the NOAA P-3 and the data void over the tropical oceans. However, the recent inclusion of the high altitude NOAA Gulfstream IV allows the first opportunity to view the three dimensional structure of the outflow layer and may shed light on the relative importance and processes involved in intensity changes. The present case study on Debby will utilize these new data supplemented by other, more traditional, data discussed in later sections.

#### 1.2.7) Inner core dynamics

Many studies have attempted to explain the variation in TC strength in terms of inner core dynamical processes and associated eyewall convection. These studies traditionally focus on concentric eyewalls and/or axisymmetric and asymmetric convective structure. Concentric

eyewalls occur when a ring of convection forms around an existing eyewall. As the outer band contracts, the inner band erodes resulting in a temporary weakening of the TC. However, the TC may strengthen if the outer band continues to contract. Studies have shown that spiral rainbands and/or convection with an associated wind maximum typically form around the eye during rapid intensification (Willoughby et al. 1982, Willoughby 1990). The formation of convective rings are common in storms which display vigorous convection, and often form in storms which have a maximum wind speed in excess of 45 meters per second (Willoughby, 1990). Reconnaissance over the Western North Pacific noted concentric eyewalls in 58% of the typhoons with MSLP < 900 hPa (Dodge et al. 1999).

One of the first to observe concentric eyewalls was Fortner (1958) when he sited an eye within an eye during Typhoon Sarah (1956). Jordan and Schatzle (1961) noted a double eye using radar data during Donna (1960), but were unable to establish a connection between the inner and outer ring. Jordan (1966) studied the irregular track of Carla (1961) in relation to multiple eyes. He speculated that the rotation of the inner eye about the outer eye might have induced the unusual track of Carla. However, it was not until Hoose and Colon (1970) that a relationship between the inner and outer eye was established. Using radar data from Puerto Rico, they observed the formation of a second eye intensifying at the expense of the inner eye. Holliday (1977) expanded upon these results in a study of Gloria (1974). Gloria underwent two rapid deepening periods followed by a period of filling over twelve hours. This rapid intensity fluctuation occurred over open water ( $>27^{\circ}\text{C}$ ) and in the absence of a synoptic environment capable of such an abrupt weakening. Furthermore, he attributed the weakening to a rainband encircling the inner eye. Additionally, Alicia (1983), Diana (1984) and Andrew (1992) were observed to have concentric eyewalls.

While the above observational studies have noted the existence of concentric eyewalls, theoretical and/or modeling studies have been used to provide further explanation of concentric eyewalls and eyewall replacement cycles. Eliassen (1951) performed the first of these studies by imposing sources of heat and momentum on a balanced symmetric vortex. By assuming gradient balance, the thermodynamic and tangential momentum equations were simplified to form a single equation governing the heat/momentum induced secondary circulation. Substituting the diagnosed secondary circulation into the original equations

provided additional insight into the temporal evolution of the heat induced circulation (Smith, 1981; Shapiro and Willoughby, 1982; Schubert and Hack, 1982). All of these studies were similar in that they represented a diagnostic analysis as opposed to closure theory. The results provided a description of the evolution of the balanced vortex induced by the addition of heat and/or momentum. A heat/momentum source forces a transverse circulation with ascent through the center of the source and compensating subsidence surrounding the source. Smith (1981) found that the local removal and/or redistribution of heat and momentum caused the tangential velocity to increase whether or not this takes place inside or outside the radius of maximum winds. Conversely, Shapiro and Willoughby (1982) and Schubert and Hack (1982) found that the tangential wind acceleration was largest inside the radius of maximum winds. Rosenthal (1971b) found similar results using a circularly symmetric primitive equation model. The results demonstrated that weakening of the surface winds was more effective if the artificial heating was induced at outer radii beyond the maximum surface winds. Hawkins (1971) used data collected during the cloud seeding experiments on Debbie (1969) and found general agreement with the results of Rosenthal (1971b). Willoughby et al. (1982) expanded and verified these findings by examining research aircraft data. They concluded that a secondary wind maximum and concentric eyes often occur when a ring of convection forms around an already formed eye. The convection provides a local heat source similar to those induced in earlier numerical studies causing rapid isobaric height falls. The radial change in the rate of isobaric height falls is concentrated on the inner edge of the wind maximum, causing an increase in gradient wind. This causes the outer eyewall to contract and intensify and the inner eye to weaken and eventually vanish. This cycle is known as eyewall replacement, and typically coincides with a temporary decrease in intensity. Marks (1985) likewise showed that the changes in eye radius were similar to that described by earlier numerical studies. He utilized reflectivity data from airborne radar systems during six days in Allen (1980).

Despite a well-formed description of the evolution of concentric eyewalls, this conceptual model is based on limited observations, model simulations, and diagnostic analysis of vortex theory. Willoughby (1990) performed the first study using extensive observations on multiple hurricanes to confirm that TC intensity change can involve the contracting of

convective rings/wind maxima. Using more than 900 radial profiles from aircraft observations collected in 19 storms over 13 years as well as radar data; he provided direct evidence in support of earlier results. Once convective rings form, they move inward in response to latent heat released within the inner edge of the convective rings, which leads to adiabatic warming and rapid isobaric height falls. This local convective heat source forms a transverse circulation with ascent through the heat source and surrounding subsidence. As the inner ring moves inward, it induces upper-tropospheric warming and decreased convective instability over the inner eyewall. Moreover, the outer eyewall inhibits the low-level warm moist inflow from reaching the inner vortex (Black and Willoughby 1992). Several additional studies have verified the existence of concentric eyewalls and linked TC intensity variation to eyewall replacement cycles. However, the possible link between synoptic scale environments including precursors and the formation of concentric eyes remains unknown.

#### 1.2.8) Land interactions

Tropical cyclones traditionally weaken as they move near or over land. However a TC can maintain hurricane status well inland especially if forward speed is high. Hurricane Hugo (1989) and Fran (1996) maintained hurricane strength well inland causing severe inland damage. Moreover, the majority of the deaths and most of the damage during Hugo (1989) and Andrew (1992) were directly related to the effects of inland wind as opposed to storm surge (U.S. Dept. of Commerce 1993). For Andrew, this was particularly compounded by the occurrence of intensification just prior to landfall. It is therefore necessary to understand the effects of landfall on the structure and intensity of a TC. Of particular importance is the ability to predict the rate of dissipation or degree to which storm force winds move inland. This section presents literature dealing with structure and/or intensity changes during and after landfall of a TC. It is important to establish the role of land interaction for the present case study on Debby, which tracked just north of the high elevation of Hispaniola.

There are three primary factors responsible for storm decay due to land interaction: 1) reduction in evaporation as the storm leaves the ocean resulting in reduction of latent heating 2) low-level air within the TC circulation is cooled by the surrounding air over land 3)

increased surface roughness or friction (Anthes 1982). While it is commonly thought that increased friction ultimately results in weakening, numerous observational and numerical studies have shown that the primary mechanism for decay is the loss of oceanic heat source and suppression of evaporation. One of the first studies to note this was Hubert (1955) in which he analyzed the pressure changes of landfalling hurricanes from 1900-1949. He concluded that friction alone could not account for the rapid decrease in wind speeds. Miller (1964) compared the rates of energy exchange at the surface over a three-day period during hurricane Donna (1960). The three-day period included two days over water and one day over land. He concluded that the increased surface roughness over land was partly responsible for the reduction of wind speed, but not responsible for the filling of the cyclone. The results show that after landfall the warm core of a TC is spread out due to the pressure within the core rising and the pressure at outside radii falling. This causes the pressure gradient across the storm to weaken and a subsequent decrease in winds.

These ideas were further investigated beginning in the late 1960's with the use of numerical models. Ooyama (1969) used a simple model to demonstrate that the supply of heat and moisture from the ocean is a crucial requirement for growth and maintenance of a TC. Rosenthal (1971a) ran sensitivity cases in which the drag and exchange coefficients for sensible and latent heat were varied. He showed that air-sea exchanges of latent heat were more important than sensible heat exchange. Tuleya and Kurihara (1978) utilized a three-dimensional primitive equation model (GFDL) to simulate landfall. They noted that the lack of evaporation is the most important factor in storm decay as compared with surface friction. Moreover, their study concluded that a storm could deepen despite increased surface roughness if sufficient latent energy is available. More recent studies have benefited from models with greater horizontal and vertical resolution, advanced parameterization of sub-cloud processes, and improved subsurface layer to expand upon these earlier findings. Tuleya (1994) utilized a triple nested version of the GFDL model to generate sensitivity runs by changing the thermal properties of the underlying surface from values typical over a mixed layer ocean to that of land. The results show that dissipation or lack of development was caused by the suppression of evaporation. Friction induced inflow becomes moist adiabatic as opposed to isothermal thus causing the low-level air converging upon the center

to cool as it encounters lower pressure. The heat capacity of land is much smaller than that of the ocean and therefore interferes with the latent heat transfer and ultimately reduction in convection. In addition, injection of surrounding dry / cool (low  $\theta_e$ ) air into the circulation can weaken the system. Moreover, the relative humidity of the middle troposphere has significant impacts on TC decay since much of the mass convergence in a TC occurs above the boundary layer (Anthes 1982). If the TC interacts with an area of low middle tropospheric relative humidity, moisture convergence and latent heat release will be reduced. This is more important in the mid-latitudes because the tropical atmosphere is conditionally unstable and daily variations in the vertical gradient of  $\theta_e$  are small over the tropics (Anthes 1982).

Most of the above studies have focused on the rate of filling and associated decrease in pressure gradient during landfall. Empirical studies have noted that the central pressure rises at a rate of 1-4 hPa per hour after landfall (Miller 1964 and Hawkins and Rubsam 1968). However, these numbers provide very little insight into the degree of inland wind potential. Moreover, enhanced convection at landfall due to increased surface friction may mix upper-level momentum downward creating mesoscale areas of higher winds. In addition there is great uncertainty as to the degree to which the surface conditions have on inland decay. For example, Andrew's (1992) central pressure rose despite its track over the moist surface of the Florida Everglades. Recent attempts to model inland winds have yielded some success. Batts et al. (1980) developed an empirical relationship between pressure gradient after landfall to the time a TC was over land and angle at which the storm made landfall. The wind speeds were then deduced using the gradient wind equation and the assumption that the translational speed resulted in asymmetric patterns of the wind field with the strongest winds in the right rear quadrant. Georgiou (1985) utilized empirical relationships for four different geographical areas in the United States to determine pressure gradient after landfall. However this relationship was a function of distance inland as opposed to time inland thus eliminating biases created by slow or stationary storms. Kaplan and DeMaria (1995) further expanded this idea by adding a correction, which accounts for the difference between storms that move inland slowly and storms that move inland rapidly. Results show that their model accounts for 91% of the variance of the best track intensity changes. Despite these advances,

there is still uncertainty concerning the relationship between surface winds and convective activity during landfall.

Enhanced convection is often associated with a landfalling TC as was evidenced in Andrew (1992) just prior to landfall in south Florida. This is mainly due to surface convergence that results from increased surface friction over land and resulting decreased onshore flow. The onshore winds associated with a landfalling TC are reduced due to increased friction resulting in a decrease in Coriolis and frictional forcing. This creates a greater cross-isobar flow increasing boundary layer inflow and convergence. Frictional effects over land produce features in the mesoscale wind and precipitation structure related to the areas of heaviest damage (Powell 1982). Despite the fact that most of the knowledge concerning the structure and dynamics of a TC is associated with storms over water due to the inherent dangers of flying reconnaissance over land, some recent studies have utilized cases of landfall in observational dense areas (Powell 1982, 1987).

Numerous theoretical studies have investigated the role of surface friction on boundary layer winds and associated convergence/divergence patterns (Shapiro 1983, Tuleya et al. 1984, Tuleya 1994). These numerical model studies suggest that convergence and rainfall will be minimum on the left side of a landfalling TC as a result of accelerating offshore wind. Early observational studies confirmed these results. Powell (1982) performed the most comprehensive of these studies in which he composited aircraft, land station, and buoy data over a period before and during landfall of Frederic (1979). He concluded that landfall causes a shift of maximum inflow angle for the right rear portion to the landward side. This resulted in increased convection on the northern side of the eyewall, which corresponds to the most damage. However, Powell (1987) showed that for Hurricane Alicia (1983), the strongest surface convergence, highest radar reflectivity, and maximum inflow angle occurred on the left of the storm as a result of increased inflow caused by the background environmental flow. Furthermore, he concluded the surface wind distribution was a complex function of the background flow, translation of the storm, and coastline orientation in addition to surface friction.

More recent studies have utilized the 10-cm WSR-88D network and even mobile Doppler systems to yield significant insight into the surface wind and precipitation structure.

Willoughby and Black (1996) concluded that the severe damage associated with Andrew (1992) was due in part to the formation of convective cells on the northern eyewall as the storm moved on land. Wakimoto and Black (1994) also concluded that increased friction during landfall led to a transient intensification of surface tangential winds through enhanced convection. Schneider (1998) showed that a convective cell during Fran (1996) organized into a bow echo and moved through Raleigh, North Carolina causing strong straight-line winds. These methods utilized single Doppler velocity and reflectivity patterns to analyze the two-dimensional wind fields. Bluestein and Hazen (1989) performed a dual-Doppler analysis of the wind field for hurricane Alicia (1983) as it moved well inland and affected Oklahoma as a tropical storm. The results indicate that the cyclonic vortex became elliptically shaped and elongated along the direction of motion. In addition, the strongest precipitation and winds were located in the east and southeast section due to enhanced convection caused by advection of moist air from the Gulf of Mexico. Even though numerical studies have shown that rapid weakening will occur even over wet surfaces (Tuleya, 1994), the results of Bluestein and Hazen (1989) suggest that the formation of convection may be tied to the available moisture of the surrounding boundary layer and surface. Moreover, Tuleya (1994) and Hopkins et al. (1998) showed that reduced wetness of the underlying surface contributes to enhanced decay. Heavy rainfall prior to landfall may play a significant role in moisture convergence and convective development. Moreover, physiological differences in soil characteristics have been linked to the formation of convection in non-tropical situations and may play a role in inland damage associated with landfall.

### 1.2.9) Literature Review Summary

Ultimately, TC intensity change involves a complex interaction of multiple processes over varying spatial and temporal scales. Studies have been plagued by the complexity of these processes compounded by the lack of observed data over the open oceans. Much is still not known regarding the relative importance of these processes leading to an overall lack of knowledge on TC intensity change. Moreover, recent numerical studies have shown that TC

intensification involves mesoscale mechanisms not easily resolved in field studies aimed at improving data coverage. Thus, traditional operational intensity guidance has relied more on climatology and/or persistence which often leads to large forecast errors especially for rapidly evolving systems. Accordingly, a purely dynamical TC model (GFDL) was incorporated operationally by the NWS in 1995, which provides intensity guidance. The GFDL has shown skill in TC intensity forecasts and has become one of the more extensively used forecasting tools available at NHC. However, the forecasting of rapid intensity changes remains problematic and was recently highlighted by the unexpected weakening of Debby (2000) along the northern coast of Hispaniola. Given that the GFDL represents the most sophisticated purely dynamical intensity model available, further advances in intensity forecasting skill would constitute an improved understanding of factors influencing rapid intensity change as well as the model's ability to resolve and forecast those features. This is the motivation for the present research. Environmental factors known to influence TC intensity have been established, and a comprehensive case study is undertaken for Debby (2000). Those factors found to be prevalent during the weakening phase will then be analyzed further within the operational GFDL runs.

### 1.3) Case Study Synopsis

Hurricane Debby (2000) represents an excellent case for further analysis given the rapid and unexpected weakening along the northern coast of Hispaniola (Figure 1). Moreover, much of the numerical guidance available at NHC indicated the system would move toward south Florida and intensify. In fact, the increasing threat of a significant TC affecting south Florida prompted the initialization of evacuation procedures in the Florida Keys. A detailed case study of Debby is presented in the following section followed by conclusions regarding features found to be responsible for the sudden weakening. The National Hurricane Center's official best track data were used for intensity and center positions. Tropical weather discussions, subjective Dvorak classifications (Dvorak 1974), and surface analyses from the Tropical Analysis and Forecast Branch of the Tropical Prediction Center were used in the analysis of the incipient disturbance/wave.

Debby began as a tropical wave, which moved off the coast of Africa on August 15, 2000. The wave continued a westward motion of 10-15 knots and slowly became better organized over the open water of the east Atlantic. A broad area of low pressure was associated with the tropical wave and a weak 1011 hPa low formed along the wave axis on August 16. Even though a low-level circulation was evident in satellite imagery for several days, the system remained too weak for a Dvorak satellite classification until August 18 when convection became better organized and banding features were evident in satellite imagery. The system was upgraded to the seventh tropical depression of the 2000 season on August 19. Persistent deep convection began forming near the center and banding increased prompting an upgrade to Tropical Storm Debby on August 20 at 0600 UTC. Initially the system had a large cyclonic envelope; however, the low-level circulation was situated west-southwest of the deepest convection. Debby was located to the south of a sub-tropical high, which kept the system on a general west-northwest track (Figure 1) with good outflow. The lower-tropospheric steering flow was quite strong and Debby moved unusually fast with the lower level center outrunning the middle level center resulting in a sheared appearance in satellite imagery. The cloud mass associated with Debby increased in both areal coverage and intensity late on 20 August into early 21 August. However, the low-level center continued to be displaced slightly southwest of the deepest convection.

Despite a sheared pattern in satellite imagery, Debby became a hurricane on 21 August at 0600 UTC and intensified to its maximum intensity of 75 knots later that day. The system remained asymmetric with most of the convection and highest wind speeds displaced north and east of the low-level center within the deep convection. Numerical guidance and the official forecast indicated that Debby would take a more poleward turn and intensify bringing her dangerously close to the southeast Florida coast in 72 hours (Figure 4). A brief weakening period began on the 22 August at which time Debby's maximum winds decreased slightly to 65 knots (kts) (Table 2) over the next 12 hours. In spite of maximum sustained winds decreasing to 65 kts, the surface pressure fell 9 hPa over a 6 hour period during this brief weakening period (Table 2). Debby's intensity then leveled at 65 kts for the next 24 hours as she moved through the British Virgin Islands and just north of Puerto Rico. Satellite imagery on 22 August indicated that deep convection began to form over the low-level center

as Debby moved north of Puerto Rico. Heavy rains in excess of 10 inches occurred over portions of Puerto Rico with reports of mudslides and damaged bridges. Some structural damage was reported from the British Virgin Islands and five homes were damaged in Puerto Rico with a total damage estimate of 0.5 million dollars. South to southwest shear increased late on 22 August and during the day on 23 August as Debby pulled away from Puerto Rico and approached the island of Hispaniola. As Debby continued to move west the structure began to change. The large envelope initially associated with the system began to shrink as more statically stable air over the east Atlantic surged south around the southwest portion of the storm, restricting inflow primarily to the south of the system. As Debby approached Hispaniola, she turned more west and paralleled the northern coast of Hispaniola maintaining minimal hurricane strength until 1200 UTC 23 August. Satellite imagery showed an increasingly disorganized system and the low-level circulation became completely exposed near 1500 UTC (Figure 5). The low-level circulation continued to move west along the coast of Hispaniola with all of the convection remaining well east of the circulation. Debby began rapid weakening over the next 24 hours and dissipated south of Cuba on 24 August. The onset of weakening began between 0600-1200 UTC 23 August (10-hPa pressure increase) through 1200 UTC 24 August when the system dissipated (Table 2). The central pressure rose 16 hPa over this time period and wind speed decreased to 35 knots.

Satellite imagery during the onset of weakening showed an increasingly ragged and disorganized convective pattern. The low-level circulation became increasingly exposed with all the deep convection remaining east of the center. The remaining convection began to move south through the Mona Passage (Figure 1), but no new convection was observed near the low-level center as it continued moving west. Scattered convection formed over eastern Cuba as the center approached but never organized about the low-level circulation. The system weakened rapidly and dissipated at 1200 UTC 24 August. The remnant open wave moved west causing thunderstorms and gusty winds over portions of Cuba and Jamaica. Debby's maximum intensity occurred at 1200 UTC 21 August (75 kt). The minimum central pressure (991 hPa) was later observed at 0300 UTC 22 August.

## Chapter 2 Data

TC intensification involves a complex interaction between upper-ocean heat content, land interactions, surrounding environmental flow, and inner core dynamics. Accordingly, this study makes use of a wide variety of operationally available data. Satellite derived winds, rawinsonde observations, and NOAA Gulfstream-IV GPS dropsondes were used to analyze the surrounding synoptic environment including the role of vertical shear, divergence, trough interactions, and jet dynamics. Multi-sensor and passive microwave imagery was used to analyze the evolution of storm structure and convection. A surface wind analysis and Quikscat sea winds were used to analyze the evolution of the surface wind field including possible disruptions to the low-level inflow. TOPEX/Poseidon data and Maximum Potential Intensity (MPI) estimates were used to investigate the role of upper-ocean heat content. Additionally, Advanced Microwave Sounder Unit (AMSU) data was used in an attempt to isolate changes in the thermodynamic structure of the system. The following sections provide a more detailed description of each of these data sources and their usage in this work.

### 2.1) Observed in-situ data

Traditionally, studies of a TC suffer from lack of observations over the open oceans until the storm nears land or makes landfall. This lack of data can complicate the analysis as the storm may be experiencing modification by land interactions as well as the synoptic environment. However, in the case of Debby, several data sources were available during the weakening process including GPS dropsonde data obtained during synoptic flow surveillance missions from the NOAA Gulfstream IV. The Gulfstream-IV releases GPS dropwindsondes at 150-200 km intervals in the TC environment to obtain profiles of wind, temperature, and humidity (Aberson and Franklin 1999, Hock and Franklin 1999). Three synoptic flow surveillance missions were flown during Debby. Two of these missions occurred near the time of dissipation (08/22 1800 UTC-08/23 0600 UTC and 08/23 1800 UTC-08/24 0600 UTC). These data were used in conjunction with the more traditional upper air soundings where available and remotely sensed satellite derived winds (see discussion below).

Surface observations are often reported at various times, heights, exposure levels, and averaging periods making analysis problematic. Powell et al. (1996) developed a procedure for a wind field analysis that conforms to a standard framework of 1-minute sustained wind speed at the 10-meter level over open terrain (land) or over an observed or modeled sea state (water). The procedure utilizes all available wind data including metar surface observations, drifting buoys, ships, and GOES-8 satellite-derived low-level winds adjusted to surface, Air Force Reserve Command (AFRC) data adjusted to the surface, and Quikscat data to construct a wind field analysis centered about some time interval. These analyses are made available by the Hurricane Research Division (HRD) and sent to the National Hurricane Center on a real-time basis. This analysis made use of archived surface wind analyses to diagnose the evolution and symmetry of the surface wind field.

## 2.2) Satellite Data

### 2.2.1) GOES Imagery and Passive Microwave Data

Multi-sensor displays of geostationary (GOES-8) and passive microwave imagery (SSM/I and TRMM) obtained from the Naval Research Laboratory (NRL) Monterey Marine Meteorology Division (Hawkins et al. 2001) are utilized to diagnose storm features and structure. The use of multi-sensor and passive microwave imagery facilitates analysis of cloud/convective patterns as well as the structure and organization of the system. Horizontal polarization, vertical polarization, and polarization corrected brightness temperature (PCT) were used to diagnose convection and structure of Debby. Additionally, the 22 GHz channel on the SSM/I satellite was used to diagnose low-level moisture surrounding Debby where available. The following section provides a brief description of these data and a more detailed discussion is available in Hawkins et al. 2000.

The 85 GHz channel was chosen based on its capability of penetrating cirrus clouds and sensitivity to emissions (below freezing level) by low-level clouds/water vapor and scattering (above freezing level) by ice/snow particles. Thus the brightness temperature is lower for large precipitation particles above the freezing level such as snow and higher for warm rain

(no ice process) including low-level clouds/water vapor. Care must be used in observations near or over land as the temperature brightness of land is similar to that of low-level clouds and water vapor. However, it has been demonstrated (Spencer et al. 1989) that the polarization diversity at 85 GHz is sufficient to differentiate low brightness temperatures due to surface water from precipitation. Away from the storm in the cloud-free environment, the sea surface may have a similar brightness temperature as convection, thereby complicating the analysis of convection. The PCT isolates the scattering effect (above freezing level) and therefore enhances deep convection and rainbands by removing noise typical in single channel imagery. PCT is computed by taking a linear difference between the polarization (horizontal and vertical) of the 85 GHz channel.

Integrated low-level water vapor derived from the 22 GHz channel on SSM/I was used to diagnose low-level moisture surrounding Debby. These data corresponds to values below 700 hPa and is considered one of the more accurate and applicable products from the SSM/I. Unlike the geostationary satellite water vapor channels (6.7-micron infrared), the low-level water vapor does not give values over multiple levels but rather represents an integrated value. The product is only valid over open water and has limited use near coastal areas. Since the marine boundary layer contains a majority of the available moisture, the product is weighted toward lower level moisture as opposed to middle level moisture. If we assume that the maximum inflow for a tropical cyclone is within the boundary layer, this product is usually a good representation of low-level moisture inflow.

### 2.2.2) Quikscat

Seawinds/Quikscat is a sun-synchronous polar orbiting satellite equipped with an active microwave sensing instrument (13.4 GHz, 110-watt) that estimates surface winds over the ocean by measuring reflection/scattering off the ocean surface. The 1,800-kilometer (km) swath width has a horizontal resolution of 25 km and measures wind speeds of 3-20 m/s with an root mean-square error of 2 m/s. Higher wind speeds above 20 m/s can have degraded quality exceeding 10% of the true value. The Quikscat covers 90% of the world's oceans per day producing roughly 2 passes/day over any geographical area. Data quality processing

indicators are also included within the data stream including rain contamination and instrument diagnostic information.

Quikscat winds were used to diagnose the evolution of the near-surface synoptic environment especially the inflow region as Debby dissipated. As discussed above, Quikscat winds are included in the HRD wind field analysis. Therefore, the Quikscat data will not be used to analyze the TC circulation and wind radii. Quikscat winds were considered estimates of the true wind field thus supplementing observed surface data. Rain flagged vectors and vectors near the edge of the swath were considered erroneous and excluded from the analysis.

### 2.2.3) GOES Satellite Derived Winds

Middle and upper-tropospheric flow was analyzed using high-density satellite-derived winds obtained from the Cooperative Institute for Meteorological Satellite Studies (CIMSS) at the University of Wisconsin. Satellite-derived wind vectors are produced from water vapor and cloud drift motions using GOES-8 multi-channel imagery by identifying and tracking targets to obtain approximations of layer-mean motions. This is accomplished by estimating the height of the target using the radiometric signal. The enhanced multi-spectral water vapor sensing capabilities of the new GOES-8 allows wind vectors to be extracted from multiple levels in cloud-free environments (Velden et al. 1997) thus overcoming some of the earlier limitations of satellite-derived cloud-tracked wind vectors. Additionally, CIMSS employs a high-resolution three-dimensional recursive filter analysis to quality control the data and output analyses as well as diagnostic fields. Further information on the CIMSS satellite winds processing methods can be found in Velden et al. (1997).

Vertical shear and upper-level divergence estimates were also provided by UW-CIMSS. These estimates were calculated first by removing the vortex associated with the system, and then bi-linearly smoothing the surrounding data back over the area removed. The area associated with the vortex removal was 800 km radius for the lower levels (700-925 hPa) and 400 km radius for the upper levels (100-350 hPa). The CIMSS shear calculations employed a novel approach by averaging the winds over two (upper and lower) layers rather than

simply using two levels (850 and 200 hPa) to represent the vertical structure of the atmosphere. The upper layer winds were defined by the pressure-weighted average of the 150-350 hPa winds. Similarly, the lower layer winds were defined by the pressure-weighted average of the 700-925 hPa winds. This method has several benefits over the traditional 850-200 hPa vector subtraction as it encompasses a larger vertical area thus better capturing the three-dimensional wind profile. Additionally, averaging over a layer increases the wind resolution used in the analysis thus relying more on satellite winds and less on the NOGAPS global analysis used as the background field.

#### 2.2.4) MPI and TOPEX/ERS-2

Maximum Potential Intensity (MPI) estimates were provided by Professor Kerry Emanuel and calculated from the daily reanalysis and Reynold's weekly sea surface temperature (SST) data from NCEP. The along track values were bi-linearly interpolated to the Debby best track position from the 2.5 degree grid using the four nearest points. However, since this method makes use of SST alone, sea-height anomalies were also utilized to investigate the role of upper-ocean heat content. Sea height anomalies were obtained from the Colorado Center for Astrodynamics Research to diagnose upper heat content in the vicinity of Debby. Sea surface heights/anomalies were derived from TOPEX and ERS-2 altimeter data. Anomaly values are plotted in three-day increments and calculated by deviations of the observed sea height from the mean sea surface.

#### 2.3) GFDL numerical model

The GFDL model is a three-dimensional dynamical TC model developed at the Geophysical Fluid Dynamics Lab and incorporated by the National Weather Service as an operational model in 1995. The GFDL hurricane prediction system is a triply nested moveable mesh model with a resolution within the inner mesh ( $1/6^0$  or  $\sim 20$  km) capable of resolving portions of the inner structure of tropical cyclones. The GFDL model uses the NCEP global analysis and information on tropical cyclone location, maximum sustained

surface wind, and wind radii structure and size provided by NHC to specify the initial conditions. To overcome the coarse horizontal resolution of the NCEP global analysis, a vortex replacement strategy is utilized in which the NCEP vortex is removed and replaced with a specified vortex. The specified vortex is generated at each initial time through a controlled spinup process using operational data provided by NHC. Observed wind distribution, TC size, and TC height are used in this process to uniquely define the radial and vertical profiles of the tropical cyclone. Additionally, the GFDL system uses the NCEP global model forecast to define the time-dependent lateral boundary conditions.

The triple nested moveable mesh has the added benefit of allowing the two inner meshes to follow the forecast position of the tropical cyclone such that the center of the system always remains within the inner mesh. The outer domain consists of 18 vertical levels (sigma coordinates) with 1 degree horizontal resolution. The lateral boundary positions of the outer domain are determined by initial conditions and forecasts as provided from NHC and remain fixed in space throughout the simulation. The medium mesh extends 11 degrees in both longitude and latitude with a horizontal resolution of 1/3 degree. The inner mesh extends 5 degrees in both longitude and latitude with a 1/6-degree horizontal resolution.

Global topography is assigned at 1/6-degree resolution with vegetation specified at 1-degree resolution. Topography for the coarse resolution is set by averaging the subgrids in the inner mesh. The GFDL system uses a cumulus parameterization with a moist convective adjustment scheme. Once initiated, the cumulus parameterization scheme adjusts the vertical profile toward the moist adiabat and the new profile is then reexamined for the possibility of further convection. The process continues until the atmosphere is no longer favorable for moist convection and the new profile is then adjusted/relaxed toward the initial profile. Owing to the inclusion of entrainment by the surrounding air and the relaxation factor, the moist convective adjustment is “soft” (Kurihara et al. 1998). Horizontal and vertical diffusion is estimated using the nonlinear viscosity scheme and a level two-closure scheme (Mellor and Yamada 1974, 1982), respectively. Vertical diffusion coefficients are a function of the vertical shear, stability, and mixing length (Kurihara et al. 1998). Vertical fluxes of momentum and heat exchange across the land/air and ocean/air interface is obtained using the Monin-Obukhov similarity theory computed from the friction velocity, friction

temperature, and friction mixing ratio of water vapor. Radiative effects are parameterized using the Schwarzkopf and Fels (1991) infrared parameterization and Lacis and Hansen (1974) solar radiation parameterization. Additional information on the GFDL modeling system can be obtained from Kurihara et al. 1998.

## Chapter 3 Methodology

Several steps were undertaken to evaluate the overall performance of the GFDL during these simulations. First, the absolute storm location and intensity errors were analyzed for each model initialization time (every 6 hrs) in order to evaluate the initialization performance. Initialization errors can have exponential impact on the forecast output and thus were the first area of interest. This task was accomplished by comparing maximum sustained wind speed and location as specified by NHC in real-time with the NHC best track data. Similarly, forecast location and intensity errors were calculated to evaluate the overall forecast performance. However, error statistic calculations are not possible for all forecast times during the later runs as the system was dissipated. Consequently, no verification is performed against remnant systems even if the model forecast the system to remain beyond the observed dissipation. However, 72-hour track forecast guidance for each run was compared with the NHC best track data to examine track tendencies and biases.

The model initialized and forecast synoptic wind fields were verified against a suite of data including satellite derived winds, NOAA G-IV dropsondes, upper air radiosondes, and corresponding model analysis from both the AVN global analysis as well as the GFDL. Each forecast step (every 6 hours) was compared with all available data at that time. Vertical shear was computed every 6 hours from the GFDL runs and verified against vertical shear from the corresponding AVN global analysis. Shear calculations are often problematic given that the vortex itself induces an environmental shear. Accordingly, shear calculations often involve removing some specified wind field associated with the vortex. Given the uncertainty involved in the vortex size, depth, and perturbed field associated with the vortex versus the environmental field, this procedure often leads to various methods of calculating vertical shear including the extent or size of the vortex removed, location of the vortex, and averaging area. It can be argued that vortex removal techniques remove some of the existing environmental shear especially if the vortex for a given case is smaller or larger than the specified removed area. Accordingly, this study makes use of a technique in which there is no attempt to manually remove the vortex. Rather, vertical shear is calculated by taking an areal average centered on the model storm location based upon a similar method employed

by DeMaria and Huber (1998) and conveyed through personal communications with Mark DeMaria (2001). If the storm center is located at the center of the averaging domain then the symmetric portion of the vortex will essentially be canceled out thus having little or no contribution to the areal average. However, tropical cyclones often display a highly asymmetric wind field and only that part which is symmetric will be negated. If we assume that asymmetries within a tropical cyclone are, to a large degree, a function of the environmental wind, then subtracting out (or in this case canceling out through averaging) the symmetric portion will yield the environmental wind itself without risking modification of shear by removing some specified vortex. This method overcomes limitations or a possible error associated with removing a specified vortex especially if the vortex characteristics change rapidly, as was the case with Debby.

Given the uncertainty in the proper size of the averaging domain, two domains were selected for test calculations of shear from the AVN global analysis. The averaging domains selected were storm-centered boxes ( $5^{\circ} \times 5^{\circ}$ ), based upon earlier work by DeMaria and Huber (1998), and a second larger ( $10^{\circ} \times 10^{\circ}$ ) box. The storm location was based upon NHC best track data. Vertical shear values from the AVN global analysis were then computed for each domain size and compared with the shear calculations obtained from CIMSS for all available times during Debby to see which of the two averaging domains produced the best overall results. While the CIMSS method of calculating shear is somewhat different, the overall philosophy behind the method is similar. Thus, the CIMSS data were utilized with the understanding that some differences should exist, and trends in the data were compared as opposed to exact values. Both the ( $5^{\circ} \times 5^{\circ}$ ) and ( $10^{\circ} \times 10^{\circ}$ ) averaging domains indicated a slight positive bias as compared with the CIMSS shear. However, both methods show the increasing shear trend and the relative peaks/valleys. The slight positive bias tends to increase with increasing shear possibly due to increased vortex contamination. While both averaging domains produced relatively similar shear values, the ( $5^{\circ} \times 5^{\circ}$ ) produced the best overall shear values as compared with CIMSS. Thus, shear calculations were similarly performed on the GFDL simulations utilizing the ( $5^{\circ} \times 5^{\circ}$ ) averaging domain centered on the model storm location.

The method utilized in this work did expand upon the method presented by DeMaria and Huber (1998) by employing a layer averaging technique similar to that used by CIMSS. The lower and upper level components of the wind were calculated by the taking layer average rather than using individual levels such as 850 and 200 hPa. In the present study, all available levels between 925 and 700 hPa were used in the lower layer calculations. Similarly, all levels between 100 and 300 hPa were used to calculate the upper layer average. This layer averaging technique allows more representative calculations of vertical shear, as sampling one individual level does not always represent the strongest winds within a layer. It is worth noting that the gridded output between the GFDL model and the AVN is slightly different. Specifically, the GFDL model has a higher horizontal resolution and outputs more individual levels than the AVN. Thus the GFDL layer averaging benefited from slightly more levels and more data points over the averaging domain; however, it is assumed that any discrepancies introduced by these differences will be relatively insignificant.

In order to test how the model intensity responds to shear, a series of steps was employed. The first step was to compare the analysis shear (AVN) against the observed intensity (NHC best track). In this way, a critical shear can be estimated by using a 12-24 hour time lag between a weakening trend and the corresponding shear value. That is, detrimental shear is considered to be the value that occurs roughly 18 hours prior to the observed onset of weakening. Since each TC seem to have individual critical shear values (i.e. resistance), it is necessary to examine each on a case by case basis. For example, high latitude and/or larger/stronger storms are often more resistant to shear. The critical shear was calculated for each GFDL forecast in a similar fashion. This method allowed analysis of the relative resistance of the GFDL vortex to vertical shear versus the actual vortex. That is, does the model tend to be more or less resistant to environmental shear than what is observed? However, the response of the inner vortex to the environmental flow represents a complex process within model simulations. It is necessary to go beyond an analysis of the shear itself to fully analyze the response of the model intensity to shear. In addition to verifying the shear against the AVN analysis, vertical cross sections of vorticity were also cut through the model storm center and compared with satellite imagery in order to analyze the degree of

vertical tilt. This procedure allows direct analysis of how the inner vortex responds to the model environmental shear.

In addition to comparing the critical shear value from the analysis (AVN) with the critical shear value from the forecast (GFDL), the actual shear trends from both the analysis and forecast were compared. While the analysis does not represent an exact representation of the true atmosphere, deviations in the forecast shear from the analysis shear were assumed to represent forecast shear error. Forecast shear from each of the GFDL simulations was compared individually with the corresponding analysis shear.

## Chapter 4 Results

### 4.1) Observational analysis

The following sections present the results of a detailed analysis of synoptic environmental features occurring during the rapid weakening of Hurricane Debby (2000). Debby underwent a temporary weakening period between August 21 1800 UTC and August 22 0600 UTC prior to dissipation. The onset of the second weakening period began between 0600-1200 UTC August 23 lasting through 1800 UTC August 24 when the system dissipated (Table 2). For ease, the results of this section will focus on the second weakening period beginning late August 22, 2000 leading to dissipation on August 24, 2000.

#### 4.1.1) Synoptic Analysis

This section provides a discussion of the evolution of synoptic scale upper tropospheric features based on analysis of satellite derived winds, upper-air soundings, and GPS dropwindsondes obtained near the time of the onset of weakening. Given that the data sources utilized lacked temporal homogeneity, several steps were undertaken in order to produce a more homogenous data set. First, missing satellite-derived data were replaced with interpolated values for the shear calculations and replaced with the next closest hour (i.e. 2100 UTC used to replace missing 0000 UTC). No attempt was made to replace/interpolate the recursive filter analysis; however, intermediate times were analyzed where possible to provide better continuity of evolving patterns. Additionally, given that the GPS dropwindsondes were deployed over a large time interval on the order of several hours, a grouping method was undertaken to assign each observation to a synoptic hour. All observations taken within 3 hours of a synoptic hour were assigned to that hour. That is, data collected between 2100 UTC and 0300 UTC were assigned 0000 UTC. Plots of all available data as well as derived fields obtained from the recursive analysis were generated every six hours starting 24 hrs prior to the onset of weakening until the system was completely dissipated.

Analysis of satellite derived winds at 1200 UTC August 22 shows that the large scale flow over Debby was dominated by an upper-level anticyclone centered approximately 300-400 nautical miles (nm) east of the Windward Islands (Figure 6C). A strong jet was located on the northern periphery of the anticyclone with the core of the strongest winds well north and east of Debby (Figure 6C). Peak wind speeds in association with the jet ranged from 40-50 kts. Satellite imagery indicated that the jet was enhancing northerly outflow that took the form of an outflow jet. Debby was situated beneath a large area of divergence aloft with the strongest values located just north of the center (Figure 6A). At this time the maximum sustained winds were near 65 kts and Debby was moving toward the west-northwest at approximately 20 kts owing to strong lower level easterly flow. The 1200 UTC sounding from St. Marteen (not shown) showed deep easterly flow extending to 350 hPa with 35 kts reported from approximately 850 hPa-700 hPa. Upper level winds over Debby were primarily from the south-southeast producing southwest shear of approximately 13 kts (Figure 6B and 7). However, most of the vertical shear was attributable to strong low-level easterly flow as opposed to strong westerlies aloft. Upstream, a longwave trough was moving off the eastern United States coast over the Western Atlantic northwest of Debby. Additionally, a weak upper-level low was located over the northwest Caribbean near Jamaica with evidence of a shortwave trough extending northward over eastern Cuba (Figure 6C, D).

At 1800 UTC August 22, the upper-level anticyclone moved west and became more east-west elongated (Figure 8C). The upper level low over Jamaica shifted slightly southwest with an upper-level trough axis extending northeast over eastern Cuba and the central Bahamas into the broader longwave trough moving eastward over the western Atlantic (Figure 8C, D). Debby continued to move west-northwest and was now just north of the Virgin Islands (Figure 1). The upper level flow over Debby continued to be dominated by the anticyclone to the east with southeast winds ranging from 16-18 kts at 200 hPa (Figure 8C). Satellite derived shear values indicated that the southwest shear weakened slightly over this time period (Figure 8B and Figure 7) as the low-level easterly flow weakened slightly. The upper-level jet to the north of Debby split creating two distinct wind maxima (Figure 8C). The first speed maximum was located over western Hispaniola with a second stronger speed maximum to the northeast of Debby. The strengthening jet appeared to increase upper

level northerly outflow over the storm. Despite a somewhat better environment for intensification, Debby remained a minimal hurricane with maximum winds of 65 kts. However, a convective burst was noted in satellite imagery over this same time period forming a symmetric central dense overcast feature (see also satellite discussion below). This burst of convection began during the typical diurnal maximum; however, it appears that increased outflow and speed divergence as well as the reduced vertical shear may have aided in the process. The slightly more favorable environment did not last long enough for any significant intensification.

By 0000 UTC August 23, the upper level anticyclone to the east of Debby moved west to approximately 50-100 nm east of the northern Leeward Islands (Figure 9C). Upper level winds over Debby veered from the southeast to south with no significant increase in speeds. However, vertical shear increased significantly from 10 kts to 17 kts (Figure 9B and Figure 7) owing mainly to a change in the direction of the upper-level flow as opposed to increasing wind speeds aloft. The upper-level speed maxima north of Debby merged to form a larger scale jet extending from just north of Hispaniola around the northern periphery of the anticyclone (Figure 9C). The core of the strongest winds remained well north of Debby; however, Debby was now situated near the right entrance region of the jet. Satellite derived upper level divergence increased significantly and the recursive filter analysis indicated that this area of strong divergence was more favorably positioned over Debby possibly due to the jet interaction (Figure 9A). It is not certain from this analysis if this increase in divergence was due to a change in the flow regime or a by-product of the burst in convection noted 6 hours earlier. However, given the favorable positioning of Debby with respect to the right entrance region of the jet to the north, it appears that some of this increase in divergence was a response to the upper-level synoptic environment. Debby's maximum sustained wind speed remained at 65 kts due to the increasing southwest wind shear despite the favorable positioning of the jet to the north and associated increase in divergence.

At 1200 UTC August 23 the upper level anticyclone became elongated from the northwest to southeast and the upstream upper low over the northwest Caribbean became sheared out slightly to the northeast with a weak trough axis remaining over central Cuba and the Bahamas (Figure 10C, D). West to southwest upper-level winds are noted over the

southwest Caribbean with a 30 kt speed maximum just south of Jamaica creating a strong area of confluence over the central Caribbean as it converged with southeast flow over the eastern Caribbean in association with the anticyclone (Figure 10A). Strong southerly flow developed north of Hispaniola in association with the strengthening jet. The core of strongest winds shifted east and the right entrance region was no longer situated favorably over Debby (Figure 10C). Upper level divergence continued to increase with the maximum values shifting just northeast of the center coincident with entrance region of the upper-level jet (Figure 10A). As the flow over Debby became more southerly, southwest shear continued to increase with values near 18 kts (Figure 10B and Figure 7). This corresponds to the time when Debby was becoming increasingly disorganized and the low-level center became displaced from the deep convection. It is interesting to note that this time lag between the onset of strong shear ( $> 15$  kts) and the weakening process as observed in satellite imagery coincides with earlier studies on this subject (Gallina 2002, Frank and Ritchie 2001, and Pasch and Velden 1999).

By 0000 UTC on August 24, the anticyclone became increasingly east/west elongated and the center ill defined over the northeast Caribbean Sea (Figure 11C). Additionally, a second anticyclonic circulation is noted over the southwest Caribbean. The upper-level flow over Debby was now from the southwest further increasing southwest shear to approximately 23 kts (Figure 11B and Figure 7). The upper-level low over the northwest Caribbean moved further west and weakened with a weak trough remaining over central Cuba and the Bahamas (Figure 11C, D). Debby was now located between two distinct upper-level wind speed maxima (Figure 11C). The first was located over the western Caribbean with peak winds of approximately 35 kts. A second stronger jet was located well north of Puerto Rico over the Atlantic. The right entrance region of the upper-level jet was now well east of Debby with the strongest divergence over eastern Hispaniola and adjacent coastal waters to the south (Figure 11A).

By 1200 UTC August 24, the nearly dissipated Debby was just south of eastern Cuba and had moved into an area with increasing southwest flow aloft in association with the upper low over the northwest Caribbean. The anticyclone over the east Caribbean remained nearly stationary with the associated jet northeast of the center. The upper-level trough over the

western Atlantic became more positively tilted with a smaller scale trough axis extending southwest over the Bahamas and western Cuba. Satellite-derived increased to 25 kts (Figure 7). The weakening Debby was still situated beneath an area of strong divergence aloft; however, the highest values were observed east of the storm over the Windward Passage and eastern Cuba.

#### 4.1.2) Ocean Interaction

Figure 12 shows the MPI values during the entire life cycle of Debby. Even though Debby is well below the observed MPI, the MPI remains nearly constant during the weakening period indicating that there was little change in the underlying heat source. There is a small decrease in MPI near the time of dissipation; however, this is likely due to the close proximity of the cyclone to Hispaniola. MPI values over land are represented as zero. Thus, if land is within 2.5 degrees of the storm, this may account for a relatively lower value (Kerry Emanuel, personal communication). However, MPI estimates may be limited by the fact that they only use sea surface temperatures thus not taking into account mixed layer depth. Figure 13 shows TOPEX/ERS-2 analysis of sea height anomalies for August 22. There are some positive anomalies well north of the track; however, no anomalies are observed in the vicinity of the storm track. TOPEX/ERS-2 analysis for August 25 shows a positive/negative couplet just north of eastern Hispaniola (not shown). This couplet was only slightly discernible in Figure 13 prior to Debby's passage, and it appears that the negative anomaly (lower heat content) becomes more negative on August 25. Analysis of MPI and sea height anomalies near the time of Debby's dissipation showed that ocean interactions (i.e. reduced available energy) played a minimal role in the weakening of Debby.

#### 4.1.3) Low-level Inflow and Moisture

Archived quikscat, low-level satellite derived winds, and surface GPS dropwindsonde data were used to investigate the low-level inflow as Debby approached and passed north of Hispaniola. The combination of these data sets provides good temporal resolution of the

evolution of the low-level structure associated with Debby as it approached and moved north of the island of Hispaniola. Of particular importance in this case was the role of the high terrain over the island in the weakening process. It is commonly thought that increased friction ultimately results in weakening; however, numerous observational and numerical studies have shown that the primary mechanism for decay is the loss of oceanic heat source and suppression of evaporation. Accordingly, this section provides a discussion of the relative role of Hispaniola in restricting the low-level inflow. The increase in equivalent potential energy within the inflow layer inside 200 km of the center is small compared to that initially advected toward the center; however, the additional fluxes are crucial for eyewall updraft (Barnes and Powell, 1995).

Debby initially had a large cyclonic envelope that evolved into an open wave-like signature as it approached Hispaniola (Figure 14). It appears that the strongest low-level inflow became oriented to the southeast of the low-level circulation as the wave-like signature formed. This can also be seen in the 925 hPa storm-relative flow shown in Figure 15 at 0000 UTC August 23 and 0000 UTC August 24. The strongest low-level inflow is typically around 950 hPa and extends up to 850 hPa (1500 meters) (Frank 1977). While the data suggest that the strongest inflow was oriented from the southeast in association with the wave pattern in the wind field, a quantitative measure of inflow is not available. Nonetheless, some general conclusions can be made regarding the role of Hispaniola in the weakening of Debby through disrupted low-level inflow. Debby began weakening early on August 23 while still well east of Hispaniola. The weakening accelerated as Debby moved along the northern coast of Hispaniola. Nearly all of the higher terrain over Hispaniola is confined to the western portion (west of 70°W) of the island (Figure 16). The terrain over the eastern portion of the island is relatively flat and generally below 500-m elevation (Figure 15). Thus, the low-level flow into the cyclone would likely not have been disrupted until the center of the circulation actually neared the island and moved west of 70° W. In this case, weakening was already underway before Debby reached the island of Hispaniola. However, once the circulation reached the island, disrupted inflow especially southeast of the center likely accelerated the weakening already underway. Convection quickly lagged to the east of the low-level center as Debby continued west along the northern coast of the island.

Additionally, no new convection was observed to form near the low-level center until it moved away from Hispaniola over the Windward Passage. Dry air intrusion owing to downslope flow may have played some role in this process. However, the full potential of downslope was not maximized until Debby reached the island given the storm relative inflow did not become perpendicular to the higher terrain until Debby was west of  $70^{\circ}$  W (Figure 16).

Integrated low-level water vapor derived from SSM/I (corresponding to values below 700 hPa) shows a large area of more dry/stable air approaching Debby from the east (Figure 14). However, the weakening trend was already underway and there appears to be sufficient moist low-level inflow near the center especially to the south. That is, even though drier air was approaching from the east, this more stable air had not yet reached the system at the time when weakening was first observed.

#### 4.1.4) Satellite Analysis

Debby initially had a large envelope and was symmetric; however, the storm began to display an increasingly “sheared” appearance as she approached the Leeward Islands on August 22 with the low-level circulation center displaced slightly west of the deepest convection. Convection associated with the system was rather ragged and disorganized early on August 22; however, as Debby approached Puerto Rico a well-formed central dense overcast (CDO) formed with a large area of cloud top temperatures colder than  $-70^{\circ}$  F (Figure 17A). Additionally, the low-level center became more aligned with respect to the convection during this period (Figure 17D). The CDO feature began to rapidly weaken during the next few hours as Debby moved away from Puerto Rico and approached Hispaniola and by 1200 UTC August 23, the CDO feature had lost much of its symmetry. Satellite imagery began to take on an increasingly sheared appearance during the early morning of August 23 (Figure 17B) and convection became increasingly disorganized and displaced east of the center (Figure 17E). Visible imagery showed that the low-level circulation became completely exposed near 1500 UTC on August 23 (Figure 5). The remaining convection then moved south through the Mona Passage along a convergence line

revealed in satellite imagery and dissipated south of Hispaniola (Figure 17C). No new convection formed near the low-level center as it moved along the coast of Hispaniola. Some convection was observed inland of Hispaniola, possibly due to orographic/diurnal effects. As the center continued west into the Windward Passage, new areas of scattered convection began to form just south of eastern Cuba. However, this area of convection never gained organization and later weakened as the remnant disturbance moved west over the northern portions of the Caribbean and Jamaica. Scattered showers and thunderstorms were observed over the northwest Caribbean as the remnant open wave moved west.

#### 4.1.5) Observational Summary

Overall, Debby represents a complex example of how multiple environmental factors can contribute to tropical cyclone structure, movement, and intensification. A case study utilizing various observed and remotely sensed data was undertaken in an attempt to isolate the dominant factors at play during the rapid weakening process. Analysis of upper-ocean heat content and MPI reveals that oceanic influences had little or no impact on the observed weakening of Debby. Accordingly, this study focused more on atmospheric features and land interactions. This was accomplished through the use of high-density satellite winds and derived fields. Additionally, this study made use of GPS dropwindsonde data obtained during a surveillance mission by the NOAA Gulfstream IV. Multi-sensor satellite imagery and Quikscat winds was also used to examine changes in structure and near storm surface environment.

During the onset of weakening, a large anticyclone to the east of Debby and an upstream upper-level low dominated the upper level synoptic environment. Initially, the upstream upper-level low had little bearing on Debby. However, as Debby approached eastern Cuba, the upper-level low increased southwest shear over the system. Debby was situated south of an anticyclonically curved jet, which acted to increase northerly outflow over the system. Additionally, as Debby moved north of Puerto Rico, jet dynamics appeared to play a role in increasing divergence over the storm. The anticyclone to the east of Debby moved southwest and became more east-west elongated on August 22, leading to increasing southerly flow

over the Caribbean. The change in direction from southeast to south significantly increased southwest shear, as the magnitude of the upper level winds remained relatively unchanged. This led to Debby experiencing increasing southwest shear as she pulled away from Puerto Rico and approached Hispaniola. The shear then remained nearly constant as the storm moved along the northern coast of Hispaniola and then increased significantly as the center moved south of Cuba.

Prior to the onset of weakening on August 23, a convective burst was noted late on August 22 into early August 23. This burst coincided with the lower-level center becoming more aligned with the mid-level center and the formation of a CDO feature over the center. Several environmental factors were occurring simultaneously during this convective burst. The forward speed of the system began to slow indicating a weakening of the low-level easterly steering flow and satellite derived vertical shear temporarily decreased during this period (Figure 7). Additionally, Debby was in a slightly more favorable upper-level flow regime and situated favorably near the right entrance region of an intensifying outflow jet. Thermally direct transverse ageostrophic circulations have been shown to support convective development in tropical cyclones (Rodgers et al. 1991, Shi et al. 1990). Speed divergence associated with the jet increased during this period with a maximum over the center of Debby. Even though the burst of convection occurred during the typical diurnal maximum, it appears that the temporary organization of Debby was due to a complex interaction of jet interactions as well as slight weakening of the low-level easterlies and associated vertical shear. Despite this temporarily favorable environment, Debby did not intensify during this period possibly due to the short duration of the more favorable environment or possibly the marginally high vertical shear. However, this analysis does indicate potential use of satellite-derived winds in analyzing the role of upper tropospheric features in observed convective tendencies and possible intensity fluctuations of tropical cyclones.

The favorable environment began to deteriorate rapidly over the next 12-24 hours. The outflow jet observed in the satellite derived winds shifted east, and Debby was no longer situated beneath the right entrance region of the jet. Additionally, satellite-derived divergence indicated that the area of strong divergence shifted east of Debby and strengthened. However, of more importance, southwest shear began to increase over Debby.

Upper level winds became more southerly over the eastern Caribbean as an upper-level anticyclone east of Debby moved southwest. In this case, the flow aloft did not strengthen, but rather a change in direction accounts for the increase in shear beginning around 0000 UTC August 23. Satellite imagery showed an increasingly sheared pattern during the early morning hours on August 23, and the weakening period began around 1200 UTC August 23 as the low-level circulation became displaced from the deep convection. This observation is consistent with the findings by Pasch and Velden (1999) in which they show a 12 to 24 hour lag between the onset of weakening of smaller/weaker tropical cyclones and increasing vertical shear. Additionally, there appears to be some influence by Hispaniola terrain in the form of restricted/disrupted low-level inflow. Analysis of quikscat data, surface observations, and satellite-derived winds indicate that the primary inflow was from the south. It is difficult to do more than speculate on the degree of influence that Hispaniola had on Debby given that there is no readily-available quantitative measure of inflow. However, the tendencies noted in satellite imagery indicate that restricted inflow may have inhibited new convection. Specifically, no convection was observed near the low-level circulation as it passed north of Hispaniola. Additionally, the low-level circulation first became void of convection as it neared Hispaniola and new convection formed as soon as the center moved away from the island into the Windward Passage despite even stronger southwest shear over that area. Given the uncertainty involved in assessing the degree of influence Hispaniola had on the weakening of Debby, it appears that restricted low-level inflow and shear both played a role in her dissipation. The relative importance of each factor remains unknown. However, the evidence presented here indicates that increasing shear was rapidly weakening Debby even before she reached Hispaniola. Additionally, given that a time lag between the onset of shear and weakening is believed to exist, it appears that vertical shear was the primary mechanism for the weakening of Debby. Restricted low-level inflow may have accelerated the weakening process as the center moved along the northern coast of Hispaniola. Thereafter, the increasing shear prevented the remnant low-level circulation from organizing convection about the center. Accordingly, the following section will focus on analyses of the GFDL initialization and forecast of vertical shear.

## 4.2) GFDL Model Analysis

### 4.2.1) Introduction and Overview

Table 1 shows the track error statistics associated with several of the operational models available at NHC along with the official forecast error during Debby (2000) as well as the ten-year average NHC forecast error. The GFDL model showed some skill relative to other guidance especially during the first 36 hours. However, beyond 36 hours, the model performance was somewhat less skillful relative to other guidance. The relatively higher errors beyond 36 hours are due to the inability to detect the weakening stage resulting in a simulated storm well beyond the observed dissipation on August 24 at 1200 UTC. Additionally, the GFDL consistently demonstrated a poleward bias indicating that Debby would move toward southeast Florida and intensify to a major hurricane (Figure 18). Intensity errors similarly indicated the greatest error toward the later part of the life cycle of Debby when the model simulated system was forecast well beyond the observed dissipation. Given that the later runs appeared to have some of the larger track and intensity forecast errors, several simulations were chosen for further analysis. These simulations included 8/21/06 UTC through 8/23/18 UTC and were chosen based upon facilitating analysis of the model forecast during the observed weakening. Thus, a total of eleven simulations/cases were chosen for analysis.

### 4.2.2) Initialization

Analysis of model initial intensity (maximum sustained wind speed) during these simulations did indicate some errors in the initialization process. Specifically, initialization on August 21 at 0600 and 1200 UTC had an absolute intensity error of 20 knots and 30 knots respectively. This is attributable in part to reconnaissance reports, which indicated the satellite intensity estimates were running weak for the system (Figure 19). Once reconnaissance reports became available, these intensity errors decreased significantly for the remainder of the model runs. However, it is interesting to note that even though these runs

were initialized 20 and 30 knots below the actual best track intensity, the forecast intensity errors for these runs were among the lowest of all the simulations analyzed. This indicates that the model had a tendency to intensify the system in these simulations overcoming the initial error. In general, initialized location errors were reasonable and do not appear to represent any significant source of error.

The model appears to accurately initialize the near-storm environment with all major synoptic features being properly located and the output winds comparing well with the observed data. The GFDL model demonstrated slightly lower shear than the corresponding AVN shear in eight of the eleven cases with only three cases demonstrating a higher shear than the AVN (Figure 20). Thus, the GFDL model had a tendency to weaken or remove some of the environmental shear for several of the simulations analyzed. This bias may be a result of the vortex removal and replacement strategy undertaken during the GFDL model initialization process. Additional work with more cases is necessary in order to confirm this speculation.

#### 4.2.3) Forecast.

For simplicity, model output times will be abbreviated using a capital F followed by the forecast period. For example, the 12-hour forecast will be referred to as F12. The simulation of Debby (2000) initialized on August 21 at 0600 UTC displayed an initial intensity error of 20 knots, and was the worst overall intensity forecast of the cases chosen (Figure 21). The simulated intensity fluctuates rapidly through the first 36 hours of the simulation before showing a more gradual strengthening period through 72 hours. Additionally, the simulated intensity does not properly indicate the weakening phase. Debby was near peak intensity just 6 hours into the simulation, then weakened slowly through the next 42 hours before weakening rapidly and dissipating thereafter. Overall, the model forecast shear matched well against the AVN global analysis through 36 hours of the simulation. Thereafter the GFDL model began to move the anticyclone positioned over the eastern Caribbean too quickly westward over with a sizeable difference becoming evident by F60. The forecast shear begins diverging from the AVN analysis near F48 and continued through F72. While it is

likely that the erroneous weakening of the shear accounts for a portion of the inaccurate forecast of strengthening beyond F36, the large discrepancy in initial intensity in this simulation makes it difficult to draw strong conclusions regarding the forecast for this particular case. Thus it is uncertain if the inaccurate forecast is due solely to an incorrect initial condition or weakening shear due to the incorrect forecast of the upper-level anticyclone and near storm environment. However, it is interesting to note that this particular simulation was the only example where the GFDL model shear was higher than the AVN analysis for an appreciable portion of the simulation. Additionally, the model intensity remained lower than the best track through roughly 54 hours of the simulation. Thereafter, the model indicates some strengthening whereas the actual system began rapid weakening. It is at this point where the model-simulated shear fell below the AVN shear.

The simulation beginning on August 21 at 1200 UTC similarly displayed a large initial intensity error. However, unlike the previous case, the intensity begins to come into phase with the best track intensity 24 to 36 hours into the simulation (Figure 22). This indicates that the model can recover from initial intensity error given a correct depiction of the environment. However, the GFDL model began to intensify the model storm beyond F48 whereas the actual storm was weakening rapidly. This discrepancy caused a 50-kt intensity error by F72. The departure of the simulated intensity from the best track intensity coincides with the erroneous forecast weakening of the vertical shear due to an over-amplification of an upper level ridge over the system (Figure 23). Recent observational studies have noted a time lag between the onset in vertical shear and weakening (Pasch and Velden 1998, Gregg Gallina 2002). This time lag ranges from 12-24 hours and is a function of the strength, size, and structure of the tropical cyclone with weak/smaller cyclone demonstrating the quickest response to shear. Employing the shear/intensity time lag to the case presented here indicates that the incorrect intensification began prior to the inaccurate shear forecast and possibly contributed to the shear forecast. While it is difficult to determine causality in this case, the data show that an incorrect depiction of vertical shear and intensity are related. Analysis of the model forecast upper-level winds versus the verifying data indicates that the erroneous weakening of shear was due to an over developed downstream anticyclone. The model output winds compare well with the observed data through 48 hours of the simulation with

significant differences becoming evident at F60. The poorly initialized intensity is also identified as a possible source of forecast error. However, the model did recover from the initial intensity error and properly simulated the beginning of the weakening phase beginning on August 23 at 1200 UTC (F36 model).

Similar to the previous two cases, the simulation initialized on August 21 at 1800 UTC displayed an initial intensity error (15 kt), however in this case the overestimate was smaller (Figure 20). Additionally, the simulated intensity quickly comes into phase with the best track intensity by F12 (Figure 24). Thereafter, the model intensity and best track intensity compare very well for the next 36 hours through F48 with the GFDL model accurately capturing the initial weakening phase between F36 and F48. The GFDL model-simulated depiction of shear is generally below that of the AVN analysis during this period. Beyond F48, the model begins to intensify the system and deviate rapidly from the best track intensity, which displays rapid weakening. A rapid departure of the GFDL model forecast shear from the AVN shear also begins at F48 with the GFDL forecast shear falling further below the AVN shear. Similar to the previous case, the divergence of the GFDL forecast shear from the AVN shear coincides with the discrepancies in the GFDL forecast intensity versus the actual intensity. Again, employing the time lag in intensity/shear, it appears that the intensity began to deviate from the best track several hours prior to the erroneous forecast weakening of shear. Another interesting point in this case is the trends in critical shear in relation to intensity trends. Utilizing the time lag between the onset of the GFDL forecast weakening and the forecast vertical shear yields a critical shear value approximately 16-18 knots. The shear continues to increase to 20 knots and then hovers at that point through F72. However, the model intensity begins to rapidly increase at F48 even though a decreasing trend in intensity had been established at a lower shear value (16-18 kt). Similarly, a comparison of the AVN analysis shear versus best track yields a critical shear value near 16-18 kt. However, unlike the GFDL simulated cyclone, the actual system continued to weaken. Thus, the GFDL simulated vortex does not appear to be as sensitive to shear as was observed. That is, the model vortex appears to be more resistant to the increasing shear than was observed. The model simulated intensity increases despite vertical shear of 20 knots, which is above the observed critical shear of 16-18 knots.

Unlike the previous cases, the simulation initialized on August 22 at 0600 UTC accurately captured the initial intensity of Debby (Figure 25). Additionally, the forecast intensity compared well with the best track intensity through 12 hours of the simulation. Thereafter, the model began to slowly strengthen the system through the remainder of the forecast period unlike the best track, which displayed rapid weakening. The forecast depiction of vertical shear is fairly reasonable during this period as well with the GFDL shear only slightly lower than the AVN shear beginning at F12. The shear then begins a more rapid deviation from the AVN shear near F24 with the forecast shear falling well below the AVN shear. Unlike the previous case, the discrepancy between forecast versus actual intensity and forecast versus actual shear is not as abrupt. That is, the model-simulated intensity slowly begins to deviate from the AVN analysis at F12 with a more rapid deviation beginning at F24. Trends in the forecast intensity match up very well with the trends in the forecast shear. It is interesting to note that the intensification for the 24-hour period from F48 through F72 (17 knots) is larger than the earlier intensification phase between F12 and F48 (11 knots). Thus, it appears that the discrepancies of the observed versus forecast intensity are a function of discrepancies between observed versus forecast shear. While it is well documented that intensity change is a function of many environmental and internal processes that can act simultaneously, the phasing of the errors in intensity and shear indicates that shear and intensity were highly related for this simulation. The observed winds compare well with the simulated winds through 24 hours of the simulation. This is in good agreement with the observed versus forecast shear, which shows a minimal difference. However, a much larger discrepancy begins at F36 in association with an over developed anticyclone to the east of Debby and the formation of a second anticyclone just north of Hispaniola (Figure 26). This results in significant errors in the upper level flow with the model forecast indicating weak anticyclonic flow over the storm whereas the verifying data indicates uniform southerly flow. The tendency of the model to over develop the anticyclone continues with even larger differences in the forecast versus observed wind field evident by F48 (Figure 27). The forecast position of the anticyclone is too far west keeping the model storm in a weak upper level flow whereas strong westerly flow was observed. This large divergence in the observed versus forecast upper-level environment keeps the model storm in a low shear environment

allowing intensification. For this particular simulation, the GFDL model moved the upper-level anticyclone to the east of Debby too quickly westward over the eastern Caribbean and developed a second anticyclone over the model storm allowing a low shear environment and intensification. The observed data indicates the anticyclone moved slower than in the model and began to weaken with strong westerly flow developing over the cyclone and rapidly increasing vertical shear.

The simulation beginning on August 22 at 1200 UTC is one of the more interesting cases as both intensity and vertical shear are initialized very close to the verifying data (Figure 28). However, despite good initial conditions, both forecast intensity and shear rapidly diverge from the observed data within a few hours of the simulation. The GFDL intensity begins to diverge from the best track within the first few hours of the simulation even though the GFDL vertical shear compares well with the AVN global analysis through F06. Thus, in this case, the departure of observed versus forecast intensity appears to be a few hours prior to the departure in observed versus forecast shear. Beyond F06, the GFDL forecast shear begins to weaken rapidly from the strengthening AVN shear. Employing the time lag in shear/intensity, the inaccurate depiction of shear begins after the intensity diverges from the best track intensity. Comparison of the model output wind field with observed data indicates that the forecast wind field began to diverge almost instantly with small differences evident at F12 (Figure 29) and large discrepancies by F24 (Figure 30). This divergence of the forecast field from the observed field is due to an over amplification of the upper-level anticyclone positioned just east of Debby. The model moves the anticyclone too far to the west and develops a well-defined ridge axis from Puerto Rico northwest to just east of the Bahamas. Additionally, a second anticyclone develops at F36 and strengthens through the forecast period. By the F48, the developing upper-level ridge and anticyclone over the system created weak anticyclonic flow and shear with observations showing a uniform westerly flow aloft (Figure 31). The discrepancy in observed versus GFDL forecast wind field becomes increasingly evident through F72 as the model continued to develop the ridge. The low shear environment supported intensification and the poleward track bias. It is also interesting to note that even though the forecast intensity was higher than the observed intensity during most of simulation, the model did indicate a weakening period at nearly the

same time as the observed onset of weakening. However, this short-term weakening was followed by intensification through the remainder of the forecast period (F72).

Both the initial intensity and shear compared well with observations for the simulation beginning on August 22 at 1800 (Figure 32). Both shear and intensity are very close to verifying data through F12 with the GFDL shear only slightly lower than the AVN analysis. The forecast intensity displays a very gradual strengthening during this period as well with a 3-knot error by F12. This appears to be due to the small underestimate of vertical shear during the first 12 hours of the simulation. The GFDL intensity begins to deviate from the best track within the first few hours of the simulation. This trend continues with the model incorrectly intensifying the storm beyond F12 whereas the actual system began weakening on August 23 at 1200 UTC. In fact, this particular run was the most aggressive of the cases intensifying the system to 105 knots at F72 when the actual system had dissipated to a remnant wave. The deviation of observed/forecast intensity coincides well with an increasing disagreement in observed/forecast shear near the same time. Despite a good initialization of the vertical shear, the forecast shear weakened well below the observed shear beyond F12 with a 24-knot difference by F42. Given the near simultaneous occurrence in shear/intensity trends and the increasing divergence of the observed/forecast shear through the simulation, it appears that track and intensity errors were connected to the inability of the model to properly simulate increasing vertical shear which ultimately dissipated the system. Similar to the previous cases, the failure of the GFDL model to accurately represent shear is primarily due to an over amplification of an upper level ridge over the storm. The shear was well represented by the GFDL for the first 12 hours of the simulation. Thereafter, the model fails to accurately capture the onset of strong westerly flow aloft with the forecast upper level flow indicating a weaker and more southerly component (Figure 33). This was due to the model erroneously developing the upper level anticyclone and moving it too rapidly westward. Additionally, the GFDL model developed a second anticyclone over the system further decreasing the shear and creating a more favorable upper level environment (Figure 33). The GFDL shear continues to fall through F72 (Figure 32) due to the over amplification of the upper level ridge.

The overall output of the simulation initialized on August 23 at 0000 UTC is very similar to the previous simulation on August 22 at 1800. Despite a very good initialization of both intensity and shear, the model storm quickly intensifies the system beyond the observed weakening system due to a rapid departure of the observed versus forecast shear (Figure 34). The GFDL model begins to weaken the shear beyond F12 with a 20-knot difference by F36. Similarly, the intensity diverges from the best track near F06 with the model never really capturing the initial weakening phase, as was the case in some of the earlier simulations, resulting in a 36-knot intensity error by F36. The initial upper-level wind field from the GFDL model compared well with observations. However, the forecast upper-level winds began to quickly deviate similar to the previous case due to an over amplification of the upper level anticyclone over the eastern Caribbean Sea. The forecast upper level flow was from the south-southwest whereas the observed winds indicated a uniform strong westerly upper level flow. This trend continued with a weak anticyclone developing over the model storm by F36. However, despite the large disagreement in observed versus forecast intensity, the model did indicate a brief period where the intensity showed little change and actually fell slightly. While the forecast weakening is not coincident with the observed weakening, it appears that this trend is very similar to those identified in the other simulations where a short weakening stage or relative minimum in intensification is followed by rapid intensification. In this case, the forecast intensity does appear to initially respond to the high shear before intensifying the storm. Thereafter, the forecast shear falls rapidly below the observed shear allowing further deepening.

The simulation beginning on August 23 at 0600 UTC is one of the more interesting cases, as it does not display some of the same patterns and trends identified in other cases. Unlike previous cases, the observed versus forecast intensity began to deviate well before the observed versus forecast shear diverges (Figure 35). The forecast intensity immediately strays from the best track intensity despite an excellent initialization of the surrounding environment and vertical shear. While shear does begins to weaken below the observed shear beyond F12 similar to the prior cases, the model intensity already displays a 25 knot error at this time. Thus, the model erroneously intensifies the system despite good initial conditions and forecast of vertical shear through F12. The weakening shear within the model

likely contributes to the over intensification beyond F12. However, it does not appear to be the initial cause of the incorrect strengthening given the lag. One possible explanation is that the model is not as sensitive to shear as the observed system. That is, it takes stronger shear to result in weakening within the model. Closer inspection of Figure 35 reveals that the initial shear is near 20 knots allowing the model storm to develop. At F06, the shear jumps to near 26 knots, which results in a temporary weakening. Thereafter, the model shear quickly falls below 20 knots allowing the system to once again intensify. Thus, in this particular case, the critical shear value for weakening is approximately 20-23 knots. Employing a similar technique to the time series of the vertical shear from the AVN global analysis versus the best track intensity yields a critical shear slightly lower in the 17-20 knot range (Figure 36). This is consistent with a climatological study of vertical shear for weak tropical cyclones, which indicates a critical shear in the 18-20 knot range (Gallina 2002). While the difference is subtle, it appears that the critical shear for weakening within the model is slightly higher than the actual observed critical shear. This may allow for erroneous intensification, which would then feedback on the near-storm environment accounting for the weakening of the environment shear. The incorrect depiction of shear then leads to further strengthening.

The initial intensity and shear of the simulation beginning on August 23 at 1200 UTC compared well with observations with only a 5-knot overestimate of initial intensity and a fairly close initial shear (Figure 37). The simulation did initially indicate the weakening phase; however, the model simulated weakening was not as rapid as observed. Additionally, the model began intensifying the system beyond F12 as the forecast shear once again fell rapidly below the AVN analysis shear. The GFDL continued to intensify the system to 86 knots by F72 well beyond the observed time of dissipation on August 24 at 1200 UTC. Similar to the previous cases, the erroneous weakening of shear is due to an over amplification of the upper-level ridge with model-simulated intensity diverging from the best track several hours before the forecast shear fell below the observed shear. This is consistent with the previous example where erroneous forecast of intensity appears to feedback on the vertical shear. Also note that the critical shear within the GFDL model (using a 12-18 hour time lag) is in the 20-23 knot range. Once the forecast shear falls below this threshold, the

intensity begins to increase. As was the case in the previous examples, the critical shear is slightly higher than the critical shear obtained from the AVN analysis (16-18 kt) thus indicating the model vortex is not as sensitive to high shear as the observed storm.

Verifying data were only available for 18 hours for the simulation beginning on August 23 at 1800 UTC as the system dissipated on August 24 at 1200 UTC. Therefore, it is difficult to conclude much about the forecast. However, this particular run best captured the initial weakening phase of Debby. The intensity is well represented through the first 18-24 hours of the simulation (Figure 38). Thereafter, the model rapidly intensifies the storm through F72 even though Debby dissipated on August 24 at 1200 UTC. Analysis of the shear values indicates that the shear initialized well and was accurately forecast through F06 with the forecast only slightly below the AVN analysis. Similar to the earlier cases, the GFDL model forecast shear weakens and quickly diverges from the AVN analysis beyond F06. However, the intensity does not immediately respond to this discrepancy, as was the case in other simulations. That is, there is not a sharp divergence in the forecast versus observed intensity coincident with the divergence of forecast versus observed shear. Even though the model intensity remains slightly above the best track intensity through F18, they appear to be in fairly good agreement with respect to the weakening trend. Thus, the trends and conclusions drawn from the other cases do not appear to hold in this particular simulation. Additionally, the conclusions regarding critical shear drawn from the other simulations do not appear to apply in this case. The model intensifies the storm beyond F24 despite shear values ranging from 23-28 knots well above the observed critical shear. This observation introduces a dilemma in terms of conclusions drawn from the others cases. Given the complex nature of intensity change and the many factors than can contribute, it is difficult to make strong conclusions as to why this particular run does not demonstrate trends similar to the other runs. One possible explanation is that disrupted low-level inflow due to the high topography of Hispaniola may have contributed. That is, the disruption lowers the critical shear for those simulations where the storm approached the island. In this case, the system was rapidly pulling away from the island possibly permitting the storm to endure stronger shear values.

## Chapter 5 Summary and Conclusions

The unexpected weakening of Hurricane Debby along the northern coast of Hispaniola on August 23, 2000 has been examined using in-situ, satellite, and numerical model data. The results of this case study showed that increasing vertical shear on the morning of August 23 was primarily responsible for the weakening of Debby. This weakening may have been aided by disruption of the low-level inflow as Debby moved north of the high terrain of Hispaniola. However, the weakening trend was already underway 6 to 12 hours before Debby reached its closest point to the island. While disrupted low-level inflow may have played a minimal role in the weakening, rapidly increasing vertical shear was identified as the primary catalyst. Based on this hypothesis, vertical shear was computed at 6-hour intervals within eleven selected GFDL simulations (initialized 21 August 1200 UTC-23 August 1800 UTC) and compared with vertical shear from the AVN global analysis. Additionally, the GFDL model forecast environmental wind field was compared with a suite of observed data including satellite-derived winds, NOAA G-IV dropwindsondes, and upper-air observations supplemented by the GFDL initial analysis (F00).

Results indicate that the GFDL initial conditions displayed slightly lower values of vertical shear as compared with the AVN analysis for eight of the eleven runs studied. While the differences were relatively small, the AVN global analysis is used to initialize the GFDL. Thus, any difference between the GFDL and AVN should be minimal. One possible explanation of the differences in shear between the AVN and GFDL is the initialization process where the vortex within the AVN global analysis is removed and replaced with a controlled spinup vortex within the GFDL. No attempt is made to quantify the initial shear error in terms of subsequent forecast error within the context of the GFDL simulations; however, several simulations did indicate that the GFDL intensity forecast is a strong function of the vertical shear for the case studied. That is, small deviations in the vertical shear value can account for the difference between an intensifying versus weakening system. Furthermore, an erroneously intensifying cyclone caused by the initial shear being too weak could feed back on the upper-level momentum field, especially if deep convection is

initiated. Thus, the differences in AVN/GFDL initial shear may contribute to forecast error and deserves additional work.

Also, the model storm does not appear to be as sensitive to shear as was the observed storm. That is, the critical shear value for initial weakening within the GFDL model is higher than the critical shear value from the analysis in nearly all the cases. Several simulations failed to weaken the storm despite accurate depictions of initial and forecast shear for portions of the simulation. Additionally, many of the runs did indicate a temporary weakening period only to quickly recover and intensify the storm thereafter. DeMaria and Huber (1998) showed that a highly tilted vortex is often the outcome of a high shear environment. In the present study, little or no vertical tilt was observed within the simulations chosen for this analysis even though model estimated and satellite derived shear values indicated a rapid increase in vertical shear coincident with the onset of weakening.

The primary conclusion of this study was deviations in observed vertical shear versus GFDL forecast shear. Every simulation analyzed demonstrated a rapid reduction in the forecast vertical shear as compared to the AVN analysis shear. Additionally, these trends were near coincident with deviations in observed intensity versus GFDL forecast intensity. The erroneous reduction in forecast vertical shear within the GFDL simulations were primarily the result of a misrepresentation of the upper-level flow due to an over developed downstream upper-level ridge. Also, an erroneous anticyclone developed over the model storm in several cases, resulting in significant deviations in the upper level environment and associated vertical shear. Deviations between the GFDL and AVN shear were also due to track differences between the model. The excessive ridge development within the GFDL runs increased the southerly flow over the system accounting for a poleward track bias. Trends in vertical shear and intensity within the GFDL appear to be related in every simulation given the near coincident occurrence. Based on this observation, the erroneous amplification of the downstream ridge is identified as the primary mechanism for both track and intensity errors within these simulation.

However, causality is somewhat more difficult to establish. That is, did the weakening shear result in the intensification or intensification lead to the weakening shear? Employing a time lag in the onset of shear and weakening as identified in observational studies, it is

shown that the model began to incorrectly intensify the system several hours prior to the incorrect reduction in forecast shear. This is further supported by the fact that several simulations demonstrated a tendency to incorrectly intensify the storm several hours before the incorrect forecast of shear was evident. While this work does not attempt to isolate the possible mechanisms responsible for this intensity versus shear feedback, a possible reason is proposed based on the data presented and similar studies. In this case, the downstream anticyclone was more intense and closer to the storm in nearly all simulations analyzed which is similar to the results presented in Henderson et al. (1999). They attributed the error in steering-level flow within the ETA model during Opal (1995) with the incorrect forecast of a downstream ridge. Specifically, the downstream ridge was too weak resulting in a significant loss of steering flow and a westward track bias. Similarly, the effects of a tropical cyclone on the surrounding environment has been studied by Ross and Kurihara (1995) by examining GFDL integrations of Hurricane Gloria (1985) with and without the cyclone included. Their results indicated that the effects of the cyclone were far greater in the upper levels with the downstream anticyclone being stronger and closer to the storm for the simulations including the cyclone as compared to the simulations without the cyclone. This type of storm to environment interaction has been shown to be the result of the redistribution of latent heat release due to convection (Bosart and Bartlo 1991). Thus, a misrepresentation of convection can result in the downstream development of an anticyclone. It is therefore hypothesized that the incorrect forecast of the downstream anticyclone within the GFDL simulations is due to the model's inability to resolve the intensity of the cyclone. In this case, excessive ridge modification was the dynamic response of an incorrect forecast of convection resulting in enhanced latent heating and downstream advection of the associated low PV outflow. The overdeveloped ridge reduces the vertical shear over the storm allowing further development of the cyclone. This allows further environmental modification by the cyclone thus establishing a self-developmental tendency within the model. While not directly established in the present study, convective parameterization appears to be the most likely catalyst for these tendencies.

Future work will benefit from a more in-depth examination of the thermodynamic and dynamic adjustments during the portion of the simulations where the forecast/observed

intensity and shear first begin to diverge. This should include both the small-scale adjustments within the cyclone itself as well as the larger scale environment. Comparing the GFDL upper-level wind and temperature against the NOAA G-IV data available for this case will further test the hypothesis presented above. The best way to directly test the above hypothesis regarding the role of convection in the modification of the downstream ridge is through sensitivity studies where the convective parameterization is modified. Efforts are currently underway at the GFDL to perform such sensitivity studies and, additional work will benefit from investigating the results of these simulations on various storms and regimes.

## Chapter 6 References

Aberson, S.D., and J.L. Franklin, 1999: Impact on hurricane track and intensity forecasts of GPS dropwindsonde observations from the first-season flights of the NOAA Gulfstream-IV jet aircraft. *Bull. Amer. Meteor. Soc.*, **80**, 421-427.

Anthes, R.A., 1970: The role of large-scale asymmetries and internal mixing in computing meridional circulations associated with the steady-state hurricane. *Mon. Wea. Rev.*, **98**, 521-528.

Anthes, R.A., 1982: *Tropical Cyclones: Their Evolution, Structure and Effects*. *Meteor Monogr.*, volume 19, No. 41, Amer. Meteor. Soc., 208 pp.

Avila, L.A., 1998: Forecasting tropical cyclone intensity changes: An operational challenge. *Preprint*, Symposium on Tropical Cyclone Intensity Change, 78<sup>th</sup> Annual AMS Meeting, Phoenix, AZ, Amer. Meteor. Soc., 1-3.

Batts, M.E., M.R. Cordes, L.R. Russel, J.R. Shaver, and E. Simiu, 1980: Hurricane wind speeds in the United States. National Bureau of Standard Building Science Series 124, U.S. Department of Commerce, 50 pp.

Bender, M.A., 1997: The effect of relative flow on the asymmetric structure in the interior of hurricanes. *J. Atmos. Sci.*, **54**, 703-724.

Black, P.G., and R.A. Anthes, 1971: On the asymmetric structure of the tropical cyclone outflow layer. *J. Atmos. Sci.*, **47**, 909-927.

\_\_\_\_\_, and H.E. Willoughby, 1992: The concentric eyewall cycles of hurricane Gilbert. *Mon. Wea. Rev.*, **120**, 947-957.

\_\_\_\_\_, and L.K. Shay, 1998: Observations of tropical cyclone intensity change due to air-sea interaction processes. *Preprint*, Symposium on Tropical Cyclone Intensity Change, 78<sup>th</sup> Annual AMS Meeting, Phoenix, AZ, Amer. Meteor. Soc., 161-168.

Bluestein, H.B., and D.S. Hazen, 1989: Doppler-radar analysis of a tropical cyclone over land: Hurricane Alicia (1983) in Oklahoma. *Mon. Wea. Rev.*, **11**, 2594-2611.

Bosart, L.F., C.S. Velden, W.E. Bracken, J. Molinari, and P.G. Black, 2000: Environmental influences on the rapid intensification of Hurricane Opal (1995) over the Gulf of Mexico. *Mon. Wea. Rev.*, **128**, 322-352.

\_\_\_\_\_, J. A. Bartlo, 1991: Tropical storm formation in a baroclinic environment. *Mon. Wea. Rev.*, **119**, 1979-2013.

Case, R.A., and H.P. Gerrish, 1984: Atlantic hurricane season of 1983. *Mon. Wea. Rev.*, **112**, 1083–1092.

Case, R.A., 1986: Atlantic hurricane season of 1985. *Mon. Wea. Rev.*, **114**, 1390-1405.

Challa, M., and R.L. Pfeffer, 1990: Formation of Atlantic hurricanes from cloud clusters and depressions. *J. Atmos. Sci.*, **47**, 909-927.

Chen, L. and W.M. Gray, 1985: Global view of the upper level outflow patterns associated with tropical cyclone intensity change during FGGE. Colorado State Univ. Atmospheric Science Paper No. 392, 126pp.

Demaria, M., J.-J. Baik, and J. Kaplan, 1993: Upper level angular momentum fluxes and tropical cyclone intensity change. *J. Atmos. Sci.*, **50**, 1133-1147.

\_\_\_\_\_, and J. Kaplan, 1994: Sea surface temperatures and the maximum intensity of Atlantic tropical cyclones. *J. Climate.*, **7**, 1324-1334.

Demaria, M., 1996: The effect of vertical shear on tropical cyclone intensity change. *J. Atmos. Sci.*, **53**, 2076-2087.

DeMaria, M., 1997: Operational tropical cyclone guidance models at the National Hurricane Center. Extended abstract, Typhoon Workshop, Boulder, CO.

DeMaria, M., and M.M. Huber, 1998: The effect of vertical shear on tropical cyclone intensity change: An historical perspective. *Preprint*, Symposium on Tropical Cyclone Intensity Change, 78<sup>th</sup> Annual AMS Meeting, Phoenix, AZ, Amer. Meteor. Soc., 22-29.

DeMaria, Mark, John Kaplan, 1999: An updated statistical hurricane intensity prediction scheme (SHIPS) for the Atlantic and eastern north Pacific basins. *Wea. Forecasting*, **14**, 326–337.

DeMaria, Mark, 2001: Personal communications.

Dvorak, V.F., 1984: Tropical cyclone intensity analysis using satellite data. NOAA Tech. Rep. NESDIS-11, 47, pp.

Dodge, P., R. W. Burpee, F. D. Marks Jr., 1999: The kinematic structure of a hurricane with sea level pressure less than 900 mb. *Mon. Wea. Rev.*, **127**, 987–1004.

Drury, S., and J.L. Evans, 1998: Modeling of tropical cyclone intensification as a result of interactions with mid-latitude troughs. Preprint, Symposium on Tropical Cyclone Intensity Change, 78<sup>th</sup> Annual AMS Meeting, Phoenix, AZ, Amer. Meteor. Soc., 65-72.

Dunn, G.E., and B.I. Miller, 1960: Atlantic hurricanes. Louisiana State University Press.

Dvorak, V.F., 1984: Tropical cyclone intensity analysis using satellite data. NOAA Tech. Rep. NESDIS-11, 47, pp.

Eliassen, A., 1951: Slow thermally or frictionally controlled meridional circulations in a circular vortex. *Astrophys. Norv.*, **5**, 19-60.

Elsberry, R.L., G.J. Holland, H. Gerrish, M. DeMaria, C.P. Guard, and K. Emanuel, 1992: Is there any hope for tropical cyclone intensity prediction? A panel discussion. *Bull. Amer. Meteor. Soc.*, **73**, 264-275.

Emanuel, K.A., 1986: An air sea interaction theory for Tropical Cyclones, Part I: Steady-state maintenance. *J. Atmos. Sci.*, **43**, 585-604.

Emanuel, K.A., 1988: The maximum intensity of hurricanes. *J. Atmos. Sci.*, **45**, 1143-1155.

Emanuel, K.A., 1991: The theory of hurricanes. *Annu. Rev. Fluid. Mech.*, **23**, 179-196,

Emanuel, K. A., 1997: Some aspects of hurricane inner-core dynamics and energetics. *J. Atmos. Sci.*, **54**, 1014-1026.

Frank, W.M., 1977: The structure and energetics of the tropical cyclone. Part II: Dynamics and energetics. *Mon. Wea. Rev.*, **116**, 1237-1244.

Frank, W.M., 1998: Mechanisms of environmentally induced hurricane structure change. Modeling of tropical cyclone intensification as a result of interactions with mid-latitude troughs. Preprint, Symposium on Tropical Cyclone Intensity Change, 78<sup>th</sup> Annual AMS Meeting, Phoenix, AZ, Amer. Meteor. Soc., 15-20.

Frank, W. M., and E. A. Ritchie, 2001: Effects of vertical wind shear on the intensity and structure of numerically simulated hurricanes. *Mon. Wea. Rev.*, **129**, 2249–2269.

Fitzpatrick, P.J., 1996: Understanding and forecasting tropical cyclone intensity change. Colorado State Univ. Atmospheric Science Paper No. 598, 346pp.

Flatau, M., W.H. Schubert, and D.E. Stevens, 1994: The role of baroclinic processes in tropical cyclone motion: The influence of vertical tilt. *J. Atmos. Sci.*, **51**, 2589-2601.

Fortner, L.E., 1958: Typhoon Sarah, 1956. *Bull. Amer. Meteor. Soc.*, **39**, 633-639.

Gallina, G.M., 2002: Environmental Vertical Wind Shear and Tropical Cyclone Intensity Change Utilizing Enhanced Satellite Wind Information. M.S. Thesis, University of Wisconsin-Madison, Madison, WI 53706 133 pp.

- Georgiou, P.N., 1985: Design wind speeds in tropical cyclone-prone regions. Ph.D. dissertation, University of Western Ontario, 295 pp.
- Gray, W.M., 1968: Global view of the origin of tropical disturbances and storms. *Mon. Wea. Rev.*, **96**, 669-700.
- Hawkins, H.F., and D.T. Rubsam, 1968: Hurricane Hilda, 1964, 2: Structure and budgets of the hurricane on Oct. 1, 1964. *Mon. Wea. Rev.*, **96**, 617-636.
- Hawkins, H.F., 1971: Comparison of results of the Hurricane Debbie (1969) modification experiments with those from Rosenthal's numerical model simulation experiments. *Mon. Wea. Rev.*, **99**, 427-434.
- Henderson, J. M., G. M. Lackmann, and J. R. Gyakum, 1999: An analysis of hurricane Opal's forecast track errors using quasigeostrophic potential vorticity inversion. *Mon. Wea. Rev.*, **127**, 292-307.
- Holland, G.J., 1983: Angular momentum transports in tropical cyclones. *Quart. J. Roy. Meteor. Soc.*, **109**, 187-210.
- Holland, G.J., and R.T. Merrill, 1984: On the dynamics of tropical cyclone structural changes. *Quart. J., Roy. Meteor. Soc.* **110**, 723-745.
- Holland, G.J., 1997: The maximum potential intensity of tropical cyclones. *J. Atmos. Sci.*, **54**, 2519-2541.
- Holliday, C.R., 1977: Double intensification of Typhoon Gloria, 1974. *Mon. Wea. Rev.*, **105**, 523-528.
- Hong, X., S.W. Chang, S. Raman, L.K. Shay, and R. Hodur, 2000: The interaction between Hurricane Opal (1995) and a warm core ring in the Gulf of Mexico. *Mon. Wea. Rev.*, **128**, 1347-1365.
- Hoose, H.M., and J.A. Colon, 1970: Some aspects of the radar structure of Hurricane Beulah on September 9, 1967. *Mon. Wea. Rev.*, **98**, 529-533.
- Hopkins, L.C., G.J. Holland, and A. Henderson-Sellers, 1998: The impact of land-surface parameterization schemes on a landfalling tropical cyclone. 23<sup>rd</sup> Conf. On Hurricanes and Tropical Meteorology. Dallas, Tx.
- Hubert, L.F., 1955: Frictional filling of hurricanes. *Bull. Amer. Meteor. Soc.*, **36**, 440-445.
- Jordan, C.L., 1966: Surface pressure variations at coastal stations during the period of irregular motion of Hurricane Carla of 1965. *Mon. Wea. Rev.*, **94**, 454-458.

\_\_\_\_\_, and F.J. Schatzle, 1961: The “double eye” of Hurricane Donna. *Mon. Wea. Rev.*, **89**, 354-356.

Kaplan, J.A. and M. DeMaria., 1995: A simple empirical model for predicting the decay of tropical cyclone winds after landfall. *J. Appl. Meteor.*, **34**, 2499-2512.

Kaplan, J.A. and M. DeMaria., 1998: Preprint, Symposium on Tropical Cyclone Intensity Change, 78<sup>th</sup> Annual AMS Meeting, Phoenix, AZ, Amer. Meteor. Soc., 119-123.

Kleinschmidt, E., Jr., 1951: Grundlagen einer Theorie des tropischen Zyklonen. *Arch. Meteor. Geophys. Bioklimatol., Ser. A*, **4**, 53-72.

Krishnamurti, T.N., W. Han, B. Jha, and H.S. Bedi, 1998: Numerical prediction of hurricane Opal. *Mon. Wea. Rev.*, **126**, 1347-1363.

Kurihara, Y., R.E. Tuleya, and M.A. Bender, 1998: The GFDL hurricane prediction system and its performance in the 1995 hurricane season. *Mon. Wea. Rev.*, **126**, 1306-1322.

Landsea, C.W., Kaplan, J., and M. DeMaria., 1998: Preprint, Symposium on Tropical Cyclone Intensity Change, 78<sup>th</sup> Annual AMS Meeting, Phoenix, AZ, Amer. Meteor. Soc., 113-114.

Lawrence, M.B., and J.M. Gross, 1993: 1992 National Hurricane Center forecast verification. *Minutes of the 47<sup>th</sup> Interdepartment Conf.*, Miami, Fl.

Leipper, D., and D. Volgenau, 1972: Hurricane heat potential of the Gulf of Mexico. *J. Physical Oceanography*, **2**, 218-224.

Madala, R.V., and S.A. Piacsek, 1975: Numerical simulation of asymmetric hurricanes on a B-plane with vertical shear. *Tellus*, **27**, 453-468.

Malkus, J.S., and H. Riehl, 1960: On the dynamics and energy transformation in steady-state hurricanes. *Tellus*, **12**, 1-20.

Marks, F.D., 1985: Evolution of the structure and precipitation in Hurricane Allen (1980). *Mon. Wea. Rev.*, **113**, 909-930.

Marks, F.D., L.K. Shay, and PDT-5, 1998: Landfalling tropical cyclones: Forecast problems and associated research opportunities. *Bull. Amer. Meteor. Soc.*, **79**, 305-323.

McBride, J.L., and R. Zehr, 1981: Observational analysis of tropical cyclone formation. Part II: Comparison of non-developing versus developing systems. *J. Atmos. Sci.*, **38**, 1132-1151.

Merrill, R.T., 1985: Environmental influences on hurricane intensification. Colorado State Univ. Atmospheric Science Paper No. 394, 156pp.

Merrill, R.T., 1987: An experiment in statistical prediction of tropical cyclone intensity change. NOAA Tech. Memo. NWS NHC-34, 34pp.

Merrill, R.T., 1988: Environmental influences on hurricane intensification. *J. Atmos. Sci.*, **45**, 1678-1687.

\_\_\_\_\_ and C.S. Velden, 1996: A three-dimensional analysis of the outflow layer of supertyphoon Flo (1990). *Mon. Wea. Rev.*, **124**, 47-63.

Mellor, G. L., and T. Yamada, 1974: A hierarchy of turbulence closure models for planetary boundary layers. *J. Atmos. Sci.*, **31**, 1791-1806.

\_\_\_\_\_, and \_\_\_\_\_, 1982: Development of a turbulence closure model for geophysical fluid problems. *Rev. Geophys. Space Phys.*, **20**, 851-875.

Miller, B.I., 1958: On the maximum intensity of hurricanes. *J. Meteor.*, **15**, 184-195.

Miller, B.I., 1964: A study of the filling of hurricane Donna (1960) over land. *Mon. Wea. Rev.*, **92**, 389-406.

Molinari, J., and D. Vollaro, 1989: External influences on hurricane intensity. Part I: Outflow layer eddy momentum fluxes. *J. Atmos. Sci.*, **46**, 1093-1105.

\_\_\_\_\_, and \_\_\_\_\_, 1990: External influences on hurricane intensity. Part II: Vertical structure and response of the hurricane vortex. *J. Atmos. Sci.*, **47**, 1902-1918.

\_\_\_\_\_, S. Skubis, and D. Vollaro, 1995: External influences on hurricane intensity. Part III Potential Vorticity Structure. *J. Atmos. Sci.*, **52**, 3593-3606.

\_\_\_\_\_, S. Skubis, D. Vollaro, and F. Alsheimer, and H.E. Willoughby, 1998: Potential vorticity analysis of tropical cyclone intensification. *J. Atmos. Sci.*, **55**, 2632-2644.

Montgomery, M.T., and B.F. Farrell, 1993: Tropical cyclone formation. *J. Atmos. Sci.*, **50**, 285-310.

National Weather Service, 1993: Hurricanes. National Weather Service Training Center, Kansas City, MO.

Ooyama, K.V., 1969: Numerical simulations of the life cycle of tropical cyclones. *J. Atmos. Sci.*, **26**, 3-40.

Ooyama, K.V., 1982: Conceptual evaluation of the theory and modeling of the tropical cyclone. *J. Meteor. Soc. of Japan*, **60**, 369-380.

- Palmen, E.H., 1948: On the formation and structure of tropical cyclones. *Geophysica*, **3**, 26-38.
- Pasch, R.J., and L.A. Avila, 1992: Atlantic hurricane season of 1991. *Mon Wea. Rev.*, **120**, 2671-2687.
- Pasch, R.J., 2000: Preliminary report: Hurricane Debby, 19-24 August 2000. DOC/NOAA/NWS/NCEP/TPC/NHC, 11691 SW 17<sup>th</sup> St. Miami, FL. [Available online at <http://www.nhc.noaa.gov/2000debby.html>].
- Perlroth, I., 1967: Hurricane behavior as related to oceanic environmental conditions. *Tellus*, **19**, 258-268.
- Perlroth, I., 1969: Effects of oceanic media on equatorial Atlantic hurricanes. *Tellus*, **21**, 230-244.
- Pfeffer, R.L., and M. Challa, 1981: A numerical study of the role of eddy fluxes of momentum in the development of Atlantic hurricanes. *J. Atmos. Sci.*, **38**, 2393-2398.
- Pfeffer, R.L., and M. Challa, 1992: The role of environmental asymmetries in Atlantic hurricane formation. *J. Atmos. Sci.*, **49**, 1051-1059.
- Pielke, R.A., Jr., and C.W. Landsea., 1998: Normalized hurricane damages in the United States: 1925-1995. *Wea. Forecasting.*, **13**, 621-631.
- Powell, M.D., 1982: The translation of the Hurricane Frederic boundary layer wind fields for the open Gulf of Mexico to landfall. *Mon. Wea. Rev.*, **110**, 1912-1932.
- Powell, M.D., 1987: Changes in the low-level kinematic and thermodynamic structure of Hurricane Alicia (1983) at landfall. *Mon. Wea. Rev.*, **115**, 75-98.
- Ramage, C.S., 1959: Hurricane development. *J. Meteor.*, **16**, 227-237.
- Riehl, H., 1954: *Tropical Meteorology*. McGraw-Hill, 392pp.
- Rodgers, E.B., S.W. Chang, J. Stout, J. Steronka, and J-J. Shi., 1991: Satellite observations of variations in tropical cyclone convection caused by upper tropospheric troughs. *J. Appl. Meteor.*, **30**, 1163-1184.
- Rogers, E.B., W.S. Olson, V.Mohan Karyampudi, and H.F. Pierce, 1998: Satellite-derived latent heat distribution and environmental influences in hurricane Opal (1995). *Mon. Wea. Rev.*, **126**, 1229-1247.

- Rosenthal, S.L., 1971a: The response of a tropical cyclone model to variations in boundary layer parameters, initial conditions, lateral boundary conditions, and domain size. *Mon. Wea. Rev.*, **99**, 767-777.
- Rosenthal, S.L., 1971b: A circularly symmetric primitive equation model of tropical cyclones and its response to artificial enhancement of the convective heating functions. *Mon. Wea. Rev.*, **99**, 414-426.
- Ross, R. J., Y. Kurihara, 1995: A numerical study on influences of hurricane Gloria (1985) on the environment. *Mon. Wea. Rev.*, **123**, 332-346.
- Sadler, J.C., 1976: A role of the tropical upper tropospheric trough in early season typhoon development. *Mon. Wea. Rev.*, **104**, 1266-1278.
- Schneider, D.G., 1998: Structural and intensity changes of Hurricane Opal (1995) and Hurricane Fran (1996). M.S. Thesis, North Carolina State University, Raleigh, NC, 27606. 53 pp.
- Schubert, W.M., and J.J. Hack, 1982: Inertial stability and tropical cyclone development. *J. Atmos. Sci.*, **39**, 1687-1697.
- Shapiro, L.J., and H.E. Willoughby, 1982: The response of balanced hurricanes to local sources of heat and momentum. *J. Atmos. Sci.*, **39**, 378-394.
- Shapiro, L.J., 1983: The asymmetric boundary layer flow under a translating hurricane. *J. Atmos. Sci.*, **40**, 1984-1998
- Shapiro, L.J., and J.L. Franklin, 1995: Potential vorticity in Hurricane Gloria. *Mon. Wea. Rev.*, **123**, 1465-1475.
- Shay, L.K., G.J. Joni, F.D. Marks, J.J. Cione, and P.G. Black, 1998: Role of warm ocean features on intensity change: Hurricane Opal. Preprint, Symposium on Tropical Cyclone Intensity Change, 78<sup>th</sup> Annual AMS Meeting, Phoenix, AZ, Amer. Meteor. Soc., 131-138.
- Shay, L.K., G.J. Goni, P.G. Black, 2000: Effects of a warm oceanic feature on hurricane Opal. *Mon. Wea. Rev.*, **128**, 1366-1383.
- Sheets, R.H., 1990: The National Hurricane Center, past, present and future. *Wea. Forecasting*, **5**, 185-232.
- Shi, J.J., S.W. Chang, and S. Raman, 1990: A numerical study of the outflow layer of tropical cyclones. *J. Atmos. Sci.*, **54**, 1231-1247.
- Shi, J.J., S.W. Chang, and S. Raman, 1997: Interaction between Hurricane Florence (1988) and an upper-tropospheric westerly trough. *J. Atmos. Sci.*, **54**, 1231-1247.

Smith, R.K., 1981: The cyclostrophic adjustment of vortices with application to tropical cyclone modification. *J. Atmos. Sci.*, **38**, 2021-2030.

Spencer, R.W., H. Goodman, and R. E. Hood, 1989: Precipitation retrieval over land and ocean with the SSM/I: Identification and characteristics of the scattering signal. *J. of Atmospheric and Oceanic Technology.*, **6**, 254–273.

Thorpe, A.J., 1986: Synoptic-scale disturbances with circular symmetry. *Mon. Wea. Rev.*, **114**, 1384-1389.

Tonkin, H., G. J. Holland, N. Holbrook, A. Henderson-Sellers, 2000: An Evaluation of Thermodynamic Estimates of Climatological Maximum Potential Tropical Cyclone Intensity. *Monthly Weather Review*: Vol. **128**, 746–762.

Tuleya, R.E., and Y. Kurihara, 1978: A numerical simulation of the landfall of tropical cyclones. *J. Atmos. Sci.*, **35**, 242-257.

\_\_\_\_\_, and Y. Kurihara, 1981: A numerical study of the effects of environmental flow on tropical storm genesis. *Mon. Wea. Rev.*, **109**, 2487-2506.

\_\_\_\_\_, M.A. Bender, and Y. Kurihara, 1984: A simulation of the landfall of tropical cyclones using a moveable nested-mesh model. *Mon. Wea. Rev.*, **112**, 124-136.

Tuleya, R.E., 1994: Tropical storm development and decay: Sensitivity to surface boundary conditions. *Mon. Wea. Rev.*, **122**, 291-304.

U.S. Department of Commerce, 1993: *Hurricane Andrew: South Florida and Louisiana August 23-26, 1992*. 131 pp.

Uccellini, Louis W., Paul J. Kocin, 1987: The Interaction of Jet Streak Circulations during Heavy Snow Events along the East Coast of the United States. *Wea. Forecasting*, **2**, 289–309.

Velden, C.S., C.M. Hayden, S.J. Nieman, W.P. Menzel, S. Wanzong, and J.S. Goerss, 1997: Upper-tropospheric winds derived from geostationary satellite water vapor observations. *Bull. Amer. Meteor. Soc.*, **87**, 173-195.

Wakimoto, R.M., and P.G. Black, 1994: Damage survey of hurricane Andrew and its relationship to the eyewall. *Bull. Amer. Meteor. Soc.*, **75**, 189-200.

Willoughby, H.E., J.A. Clos, and M.G. Shoreibah, 1982: Concentric eyewalls, secondary wind maxima, and the evolution of the hurricane vortex. *J. Atmos. Sci.*, **39**, 395-411.

Willoughby, H.E., 1990: Temporal changes of the primary circulation in tropical cyclones. *J. Atmos. Sci.*, **47**, 242-264.

Willoughby, H.E., and P.G. Black, 1996: Hurricane Andrew in Florida: Dynamics of a disaster. *Bull. Amer. Meteor. Soc.*, **77**, 543-549.

Wu, C-C., and H-J. Cheng, 1999: An observational study of environmental influences on the intensity changes of typhoons Flo (1990) and Gene (1990). *Mon. Wea. Rev.*, **127**, 3003-3031.

Forecast	Period (hrs)				
	12	24	36	48	72
AVNI	54(15)	82(13)	106(11)	85(9)	37(5)
CLIP	48(15)	91(13)	138(11)	172(9)	378(5)
GFDI	45(15)	74(13)	100(11)	106(9)	145(5)
NGPI	43(15)	80(13)	112(11)	138(9)	149(5)
UKMI	37(14)	75(12)	96(10)	80(8)	87(5)
NHC (official)	43(15)	75(3)	90(11)	85(9)	132(5)
NHC (official) 10-yr average	46	85	122	158	235

**Table 1.** Official track forecast errors for Debby (2000) in nautical miles with number of forecasts in parenthesis.

Date/Time (UTC)	Latitude (EN)	Longitude (EW)	Pressure (mb)	Wind Speed (kt)	Stage
19 / 1800	12.0	44.5	1010	30	tropical depression
20 / 0000	12.6	45.3	1010	30	"
20 / 0600	13.3	46.8	1009	35	tropical storm
20 / 1200	14.0	48.8	1008	40	"
20 / 1800	14.7	50.6	1007	45	"
21 / 0000	15.1	52.1	1006	55	"
21 / 0600	15.4	54.0	1005	65	hurricane
21 / 1200	15.7	56.3	1004	75	"
21 / 1800	16.1	58.5	1004	75	"
22 / 0000	16.8	60.1	995	70	"
22 / 0600	17.5	61.7	993	65	"
22 / 1200	18.1	63.5	994	65	"
22 / 1800	18.8	65.4	995	65	"
23 / 0000	19.2	66.7	995	65	"
23 / 0600	19.5	68.1	995	65	"
23 / 1200	19.8	69.7	1005	60	tropical storm
23 / 1800	20.0	71.5	1009	50	"
24 / 0000	19.9	73.3	1010	40	"
24 / 0600	19.6	75.1	1011	35	"
24 / 1200	19.5	77.0	1011	30	tropical depression
24 / 1800					dissipated
21 / 1200	15.7	56.3	1004	75	maximum intensity
22 / 0300	17.1	60.9	991	70	minimum pressure
22 / 0600	17.5	61.7	993	65	landfall near Barbuda
22 / 0915	17.9	62.8	993	65	landfall near St. Barthelemy
22 / 1500	18.5	64.4	994	65	landfall near Virgin Gorda

**Table 2.** Official National Hurricane Center best track for Debby 2000 August 19-24 (from Pasch 2001).

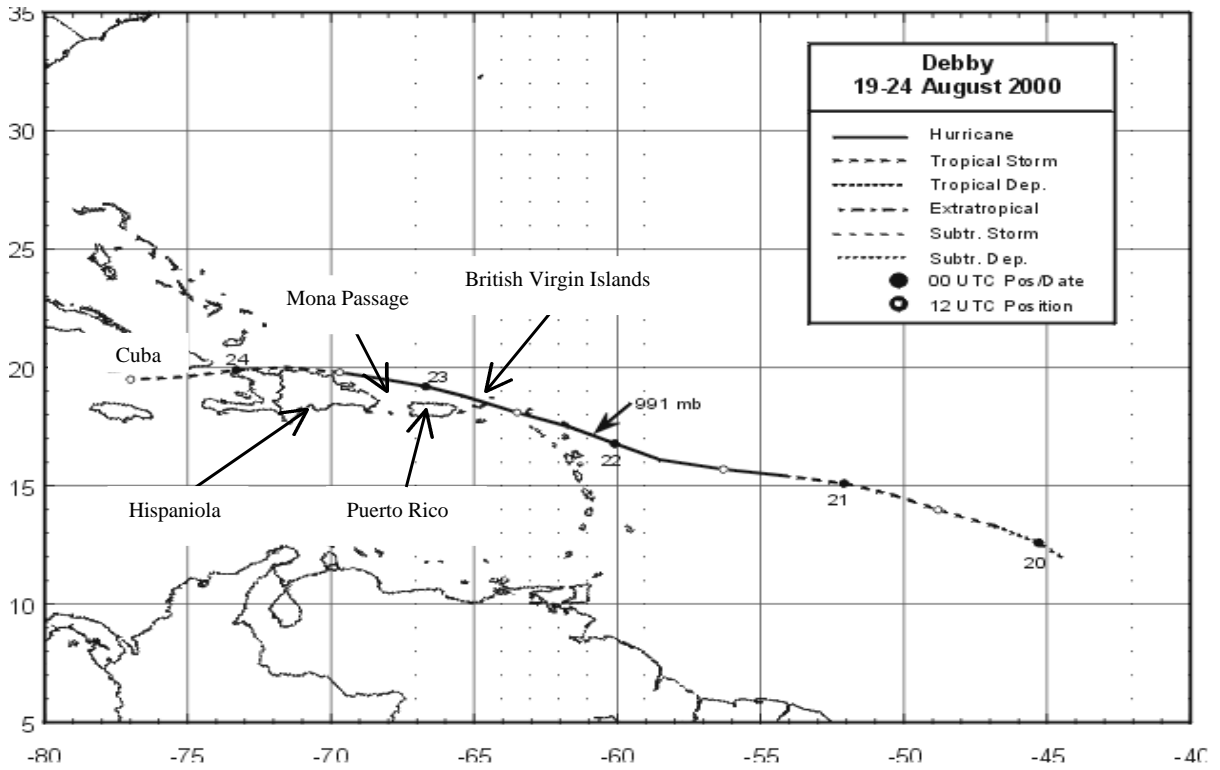


**Figure 1.** Official National Hurricane Center best track for Hurricane Debby August 19-24, 2000.

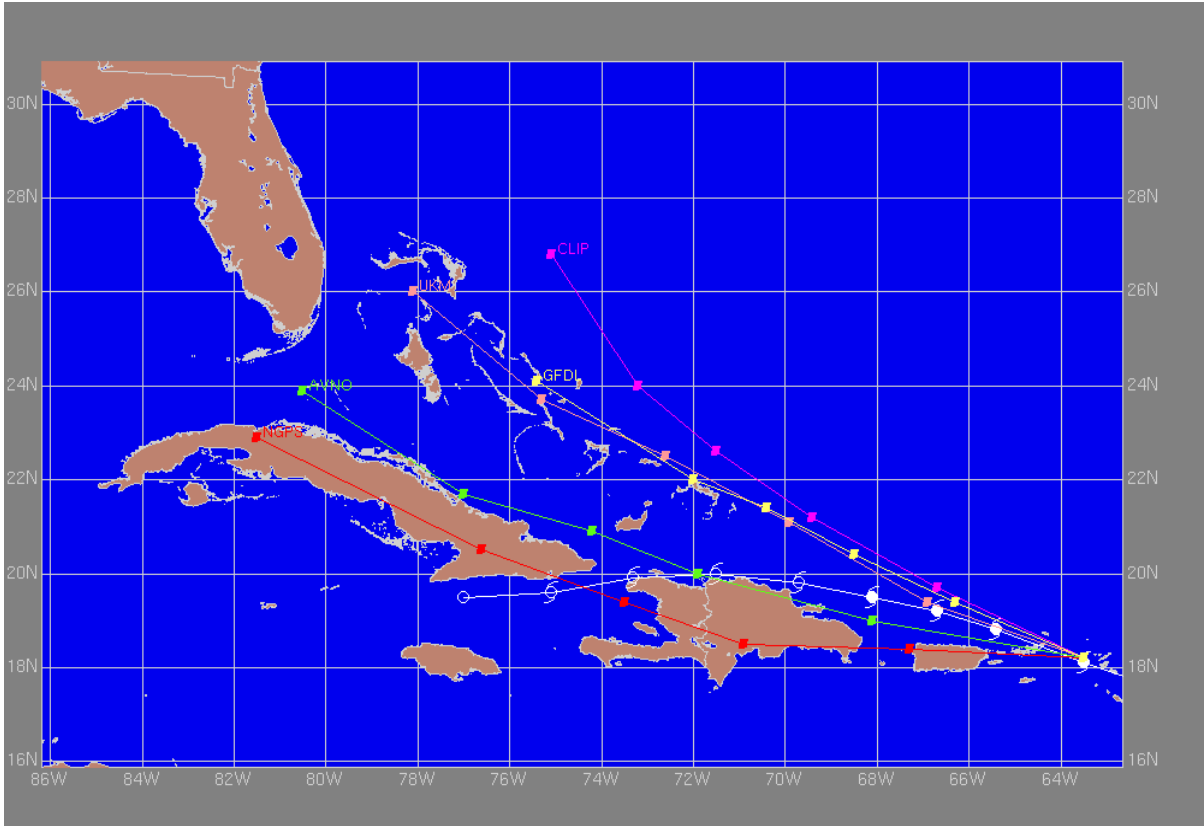


**Figure 2.** Comparison of the 72-hour forecasts (12 hour points) for UKMET (orange), AVN (green), NOGAPS (red), Clipper (pink), and GFDL (yellow) initialized 1200 UTC 22 August along with the official NHC best track (white) from 1200 UTC 22 August through 1200 UTC 24 August.

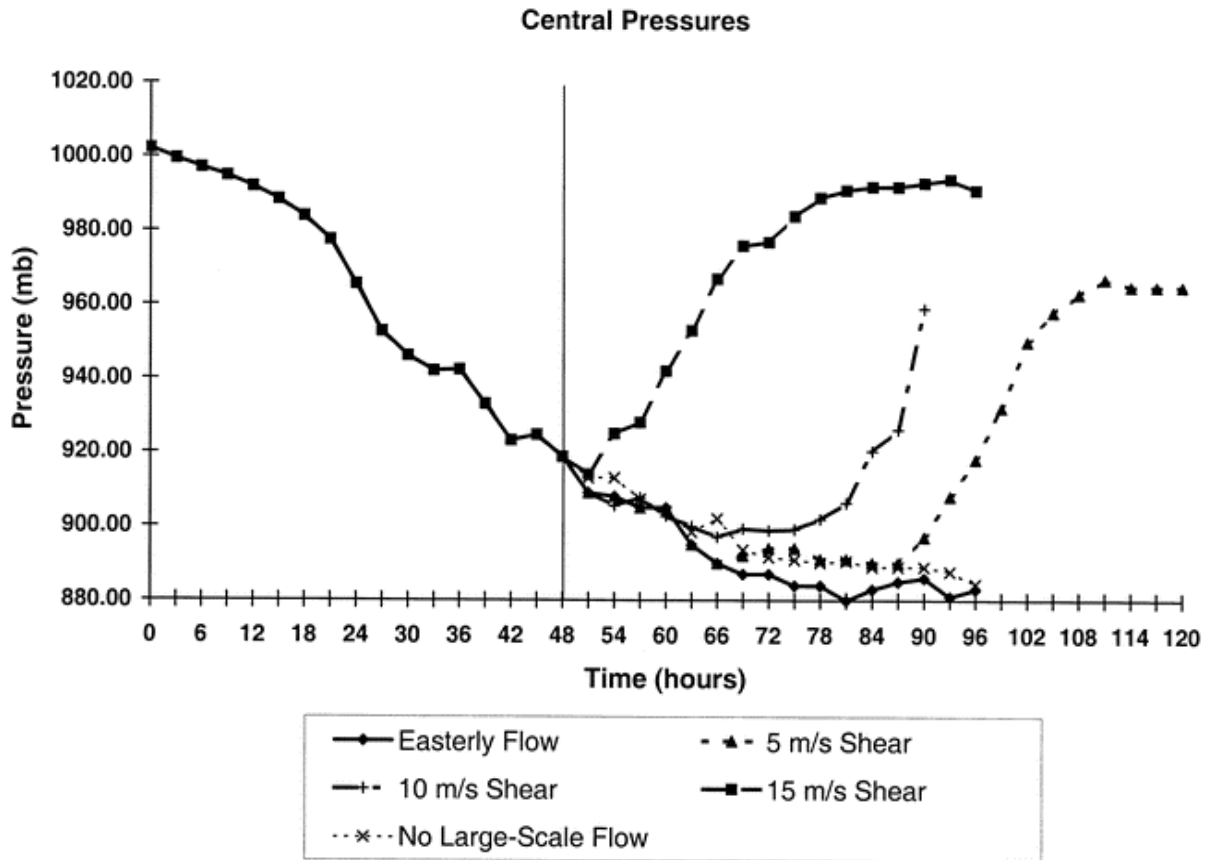


**Figure 3.** Time series of minimum central pressures for the cases with constant easterly flow of 3.5, 5, 10, and 15  $\text{m s}^{-1}$  shear, and no large-scale flow. The vertical line at  $t = 48$  h is shown to mark the time at which the environmental fields are changed to introduce the shear or zonal flow (from Frank and Ritchie 2001).

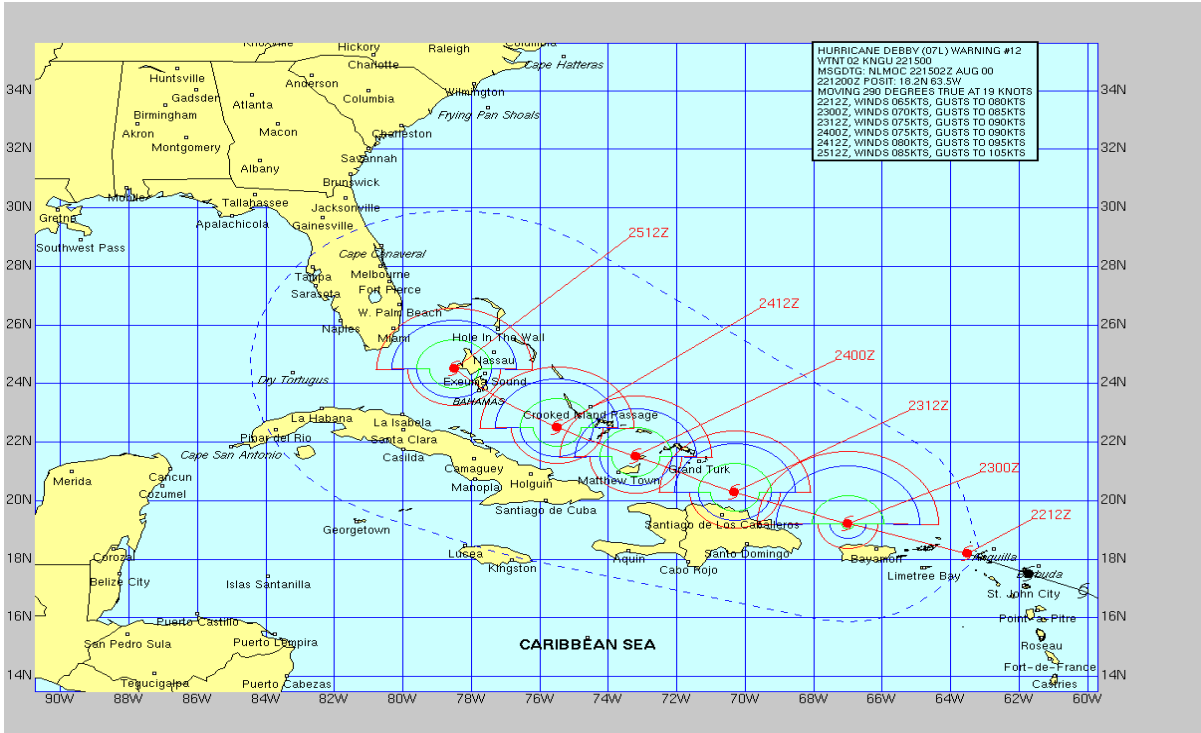


**Figure 4.** NHC 72-hour forecast from August 22 1200 UTC. Black hurricane symbols indicate past track. Red hurricane symbols indicate forecast locations in 12-hour increments. Green, blue, and red lines indicate radius of 63, 50, and 34 knot winds respectively. Dash blue line indicates area of avoidance.

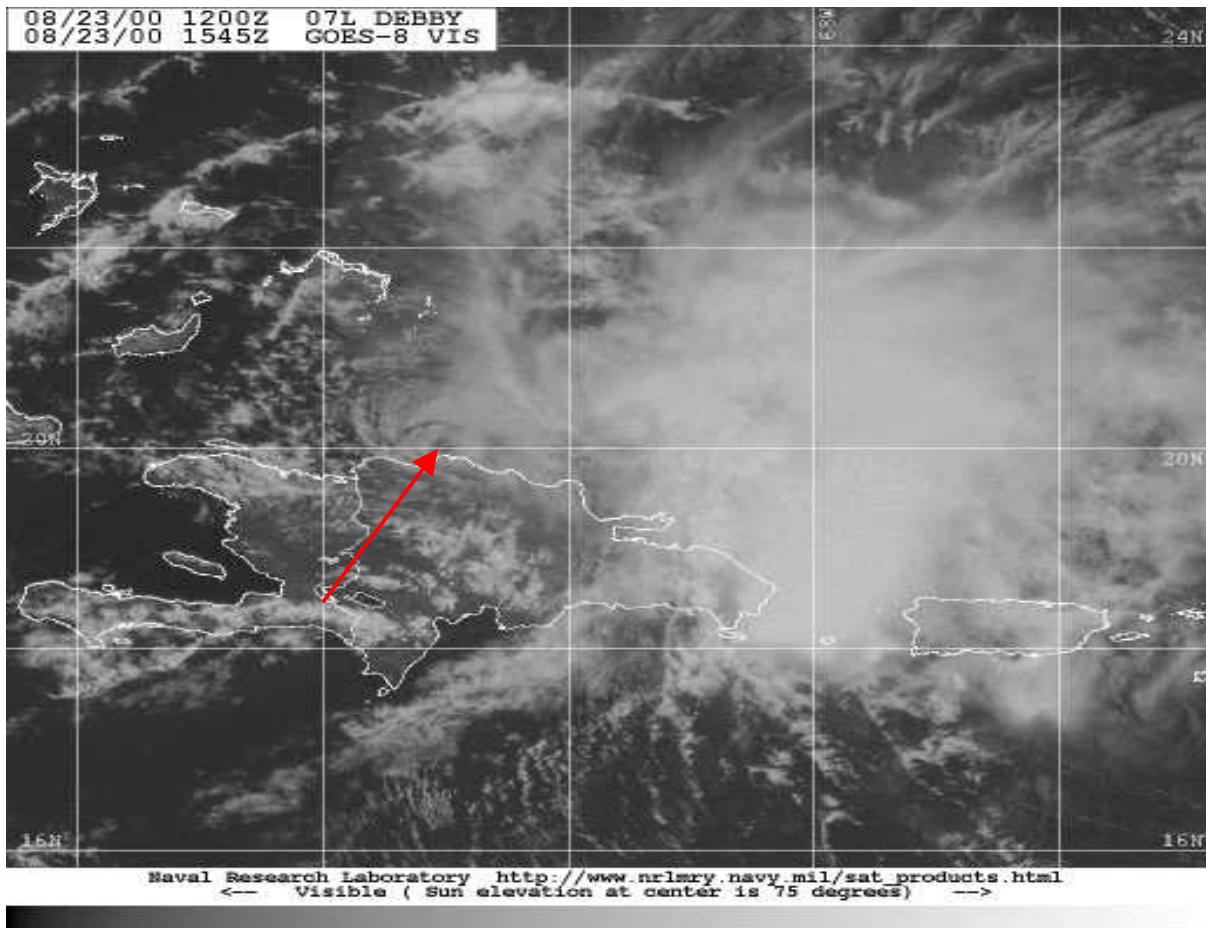
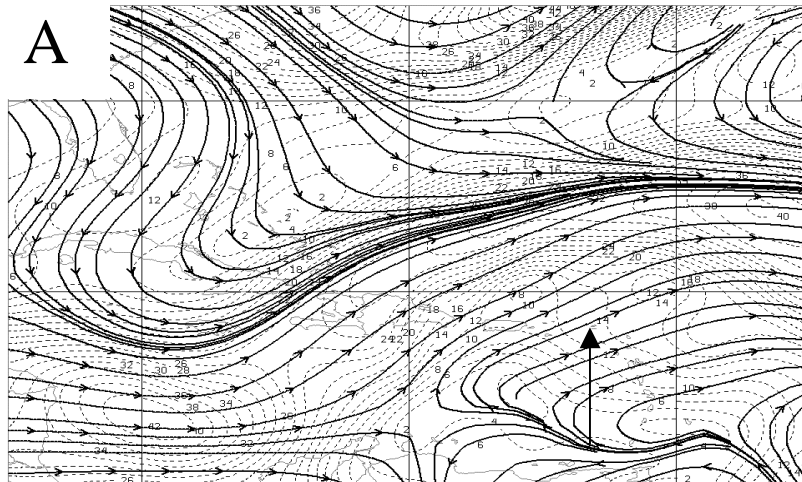
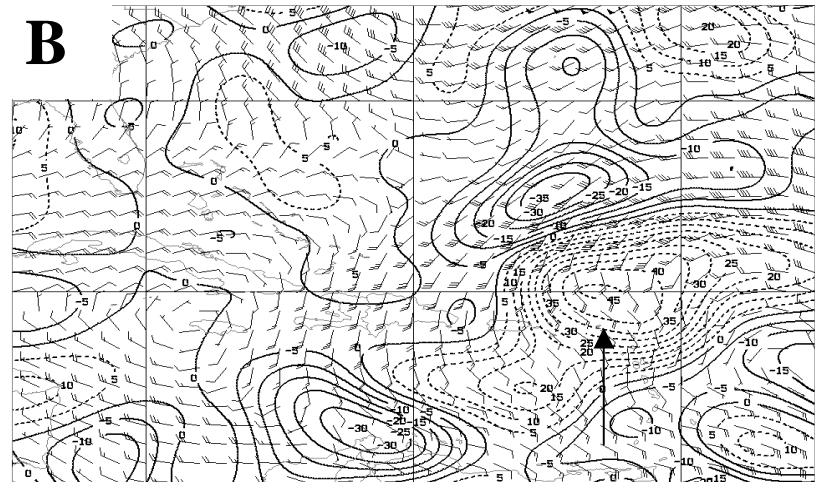


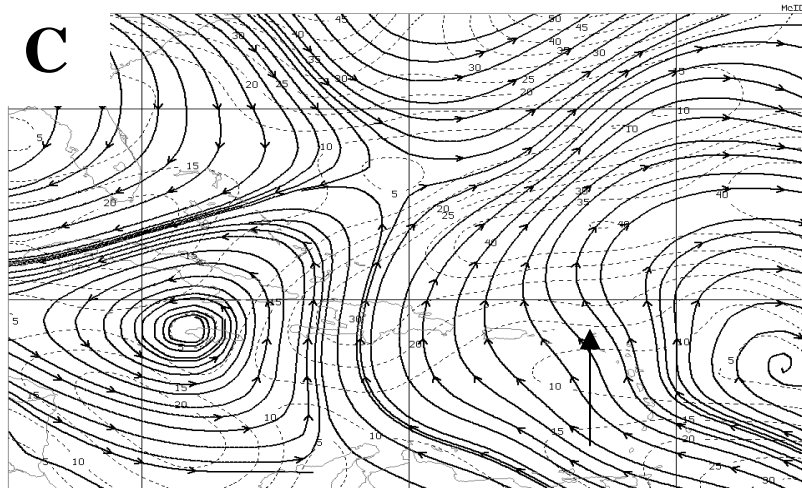
**Figure 5.** One kilometer GOES-8 Visible satellite imagery on August 23 1545 UTC. Tip of arrow indicates location of low-level circulation.



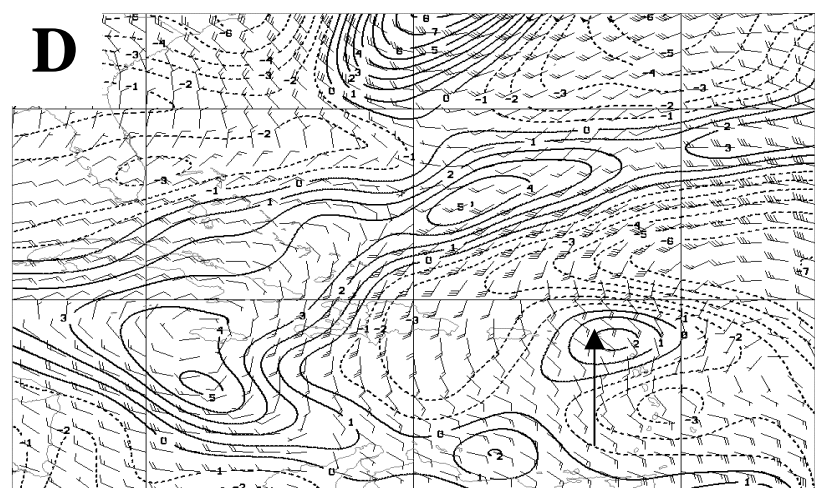
STR TIME:10:25:00 DAY:2000235085 3900235



DV8 (1/5:1E6) 150 TIME:10:25Z DAY:3900235



STR 200 TIME:10:25Z DAY:3900235 3900235



WOR6 (1/5:1E9) 0200 TIME: 10:25Z DAY:0900235

**Figure 6.** Four-panel display of 200 mb wind (kt)/150 mb divergence ( $10^{-6} s^{-1}$ ) (panel A), 200/850 mb shear streamlines/speed (kts) (panel B), 200mb streamlines/speed (kt) (panel C), 200 mb wind/relative vorticity ( $10^{-5} s^{-1}$ ) (panel D) for August 22 2000 1200 UTC. Tip of arrow indicates approximate location of the center of Debby.

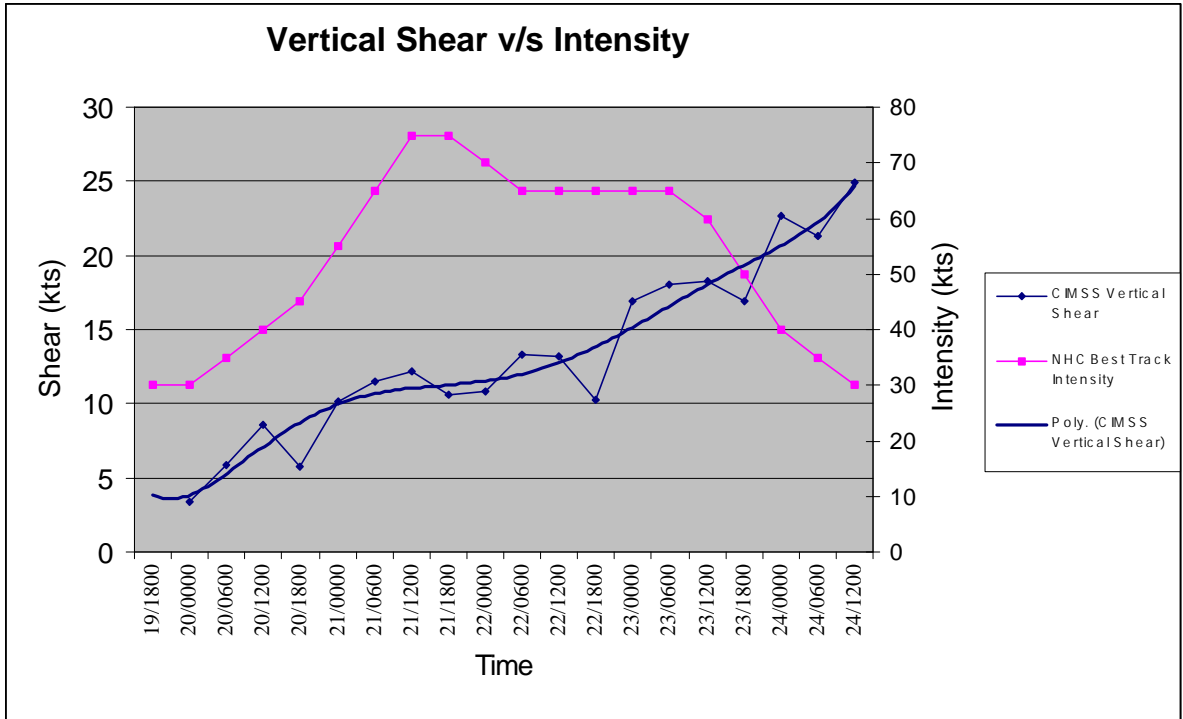
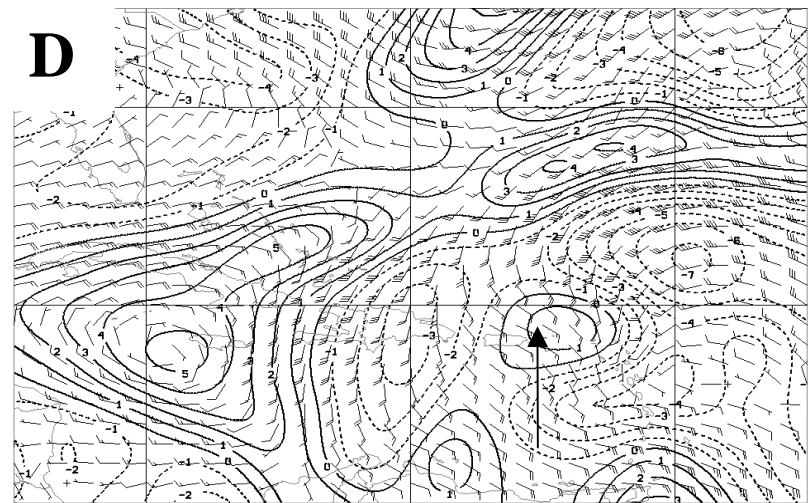
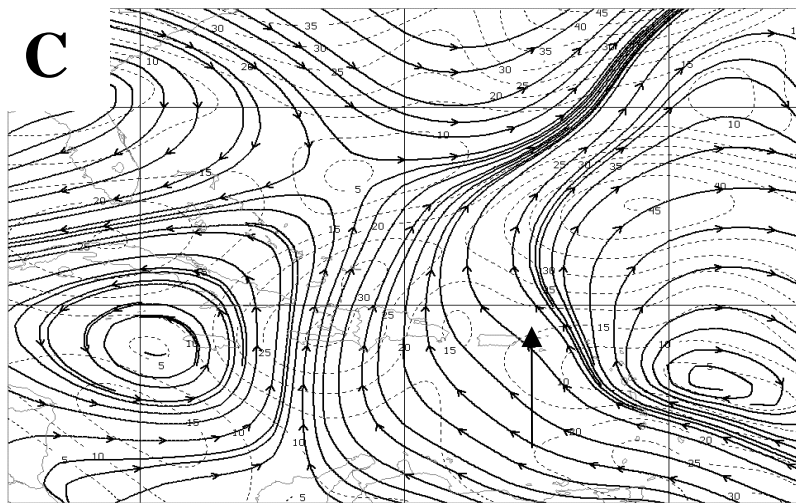
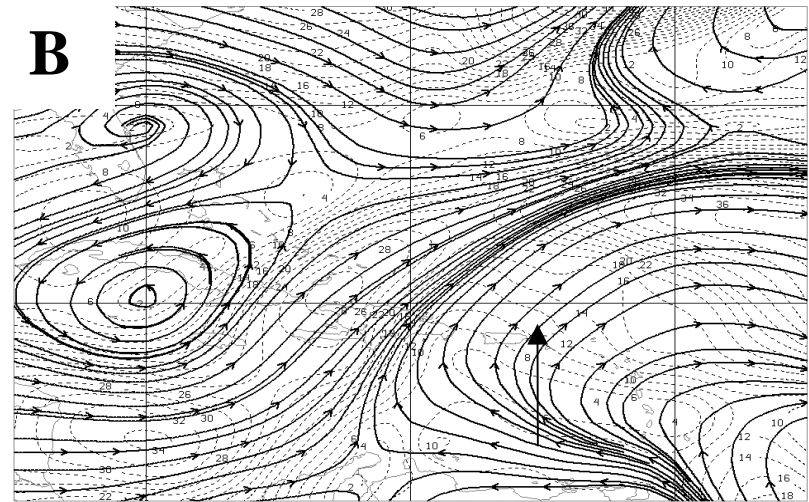
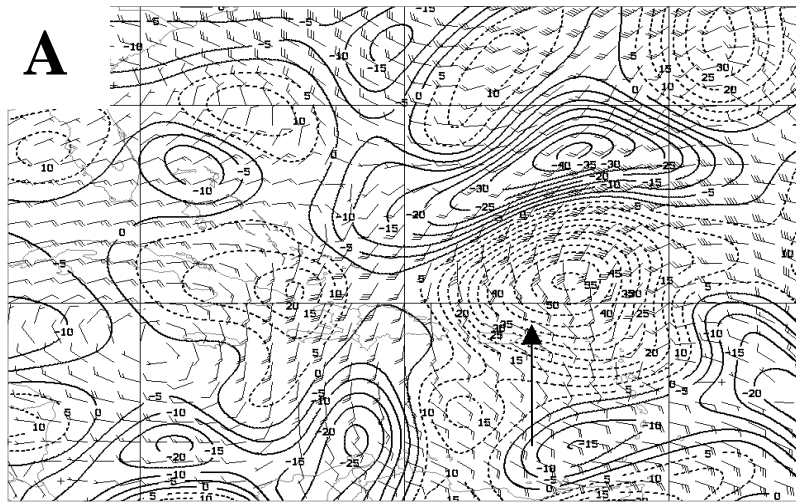


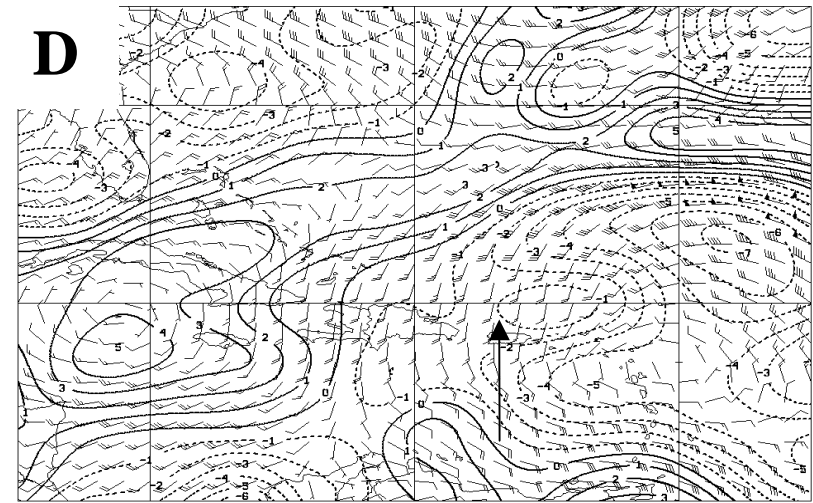
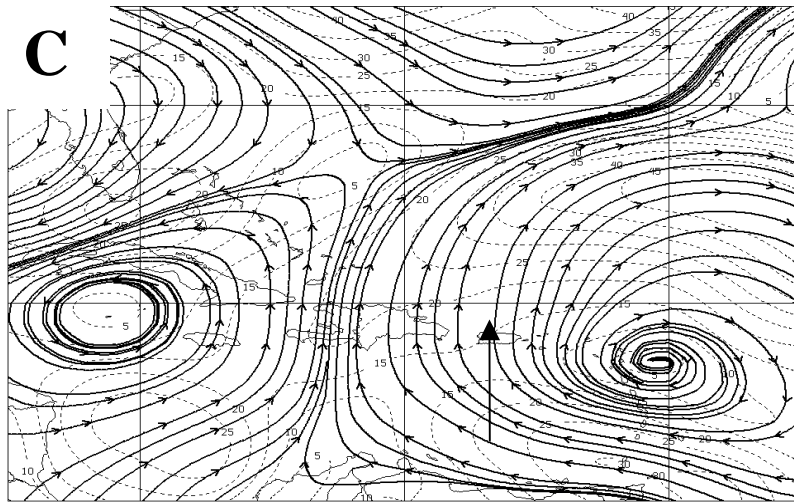
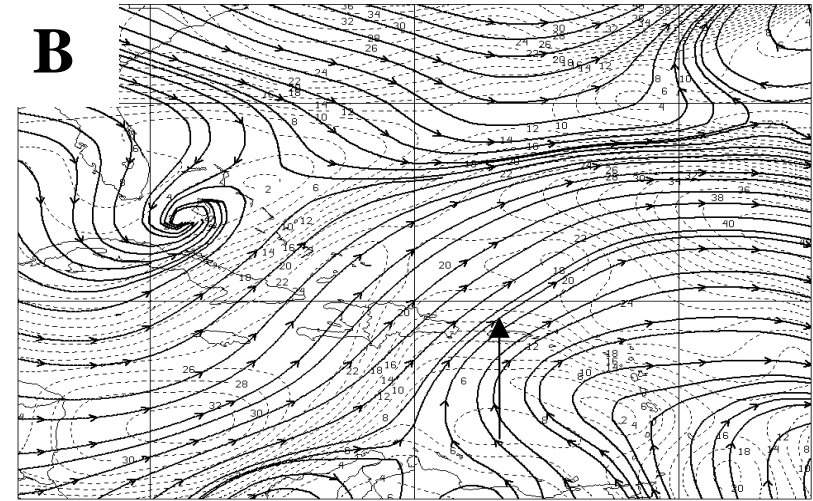
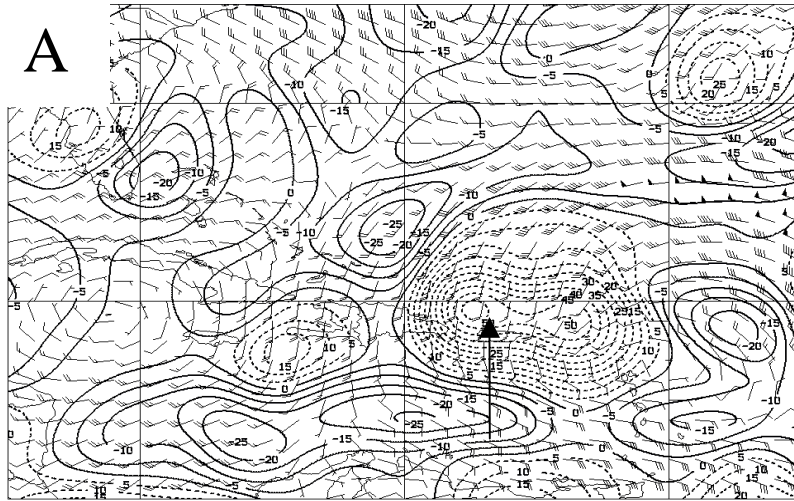
**Figure 7.** Time series analysis of CIMSS vertical wind shear (knots) versus intensity (knots) for Debby (2000). A trend analysis is also shown for vertical shear using a six-degree polynomial function. Horizontal axis denotes time (tick mark equals 6 hrs) from August 19 1800 UTC through August 24 1200 UTC.



SFR 2000 TIME:16/20Z DAY:3900239900235

VOR: (11/SK1E90200) TIME: 16/20Z DAY:0800235

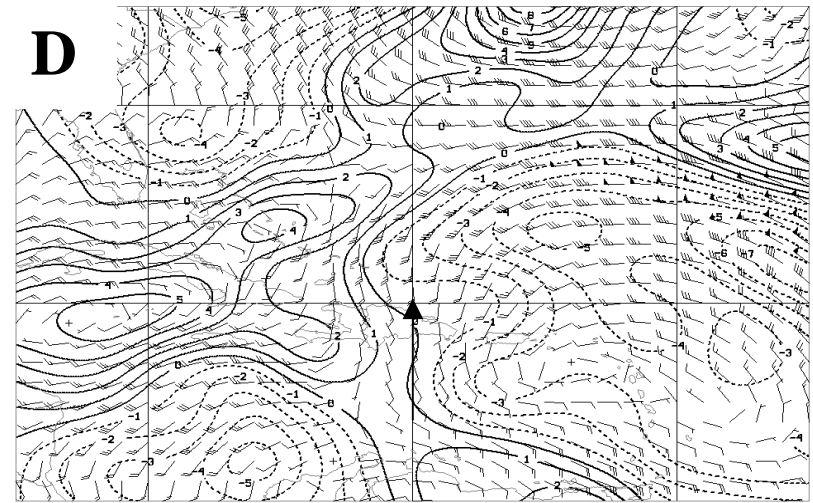
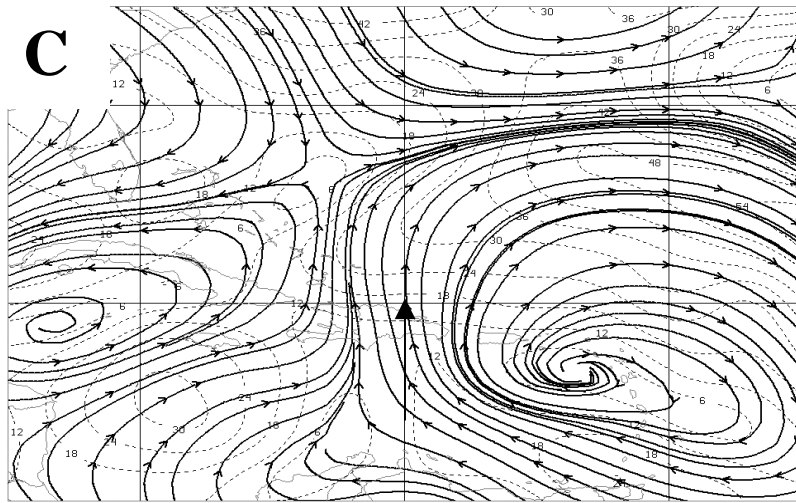
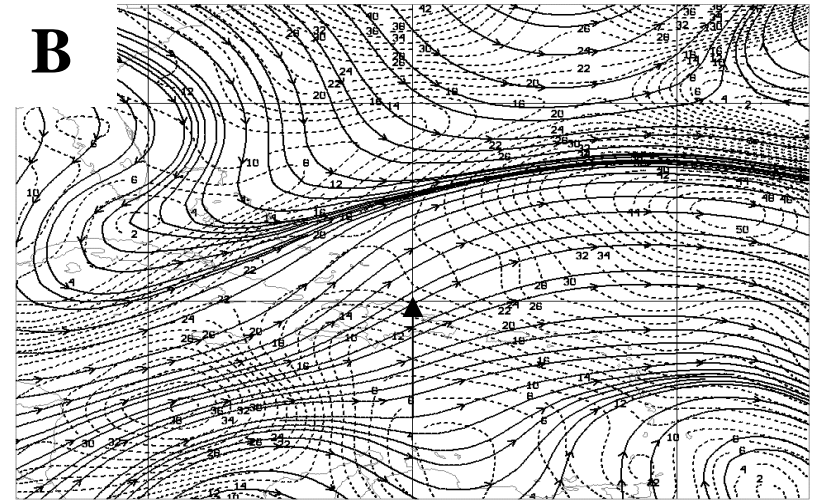
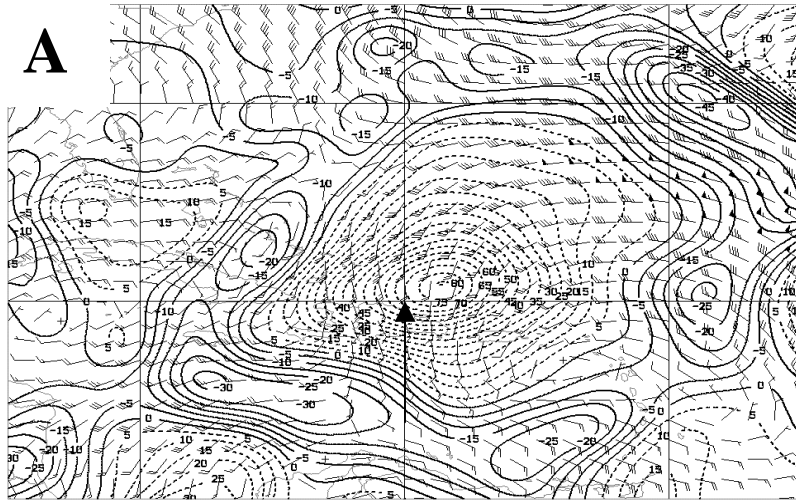
Figure 8. Same as in Figure 6 except for August 22 2000 1800 UTC.



SFR 2000 TIME: 22:05Z DAY: 3900239900235

VOR: 115K1E590200 TIME: 22:20Z DAY: 0800235

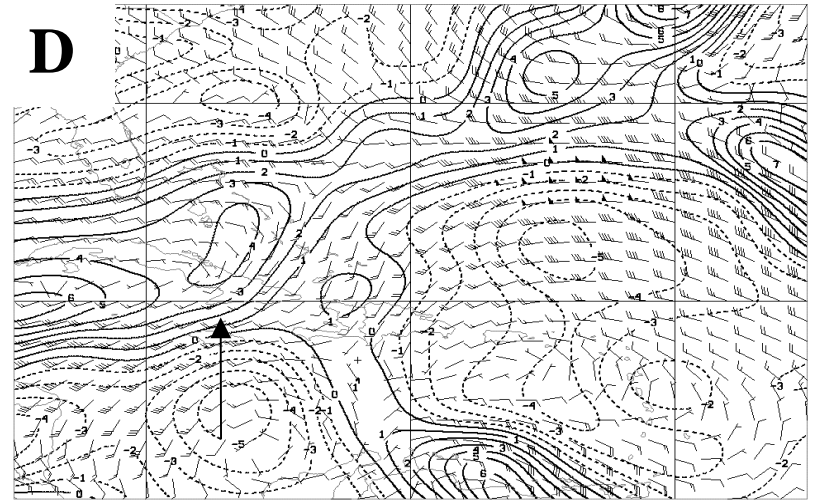
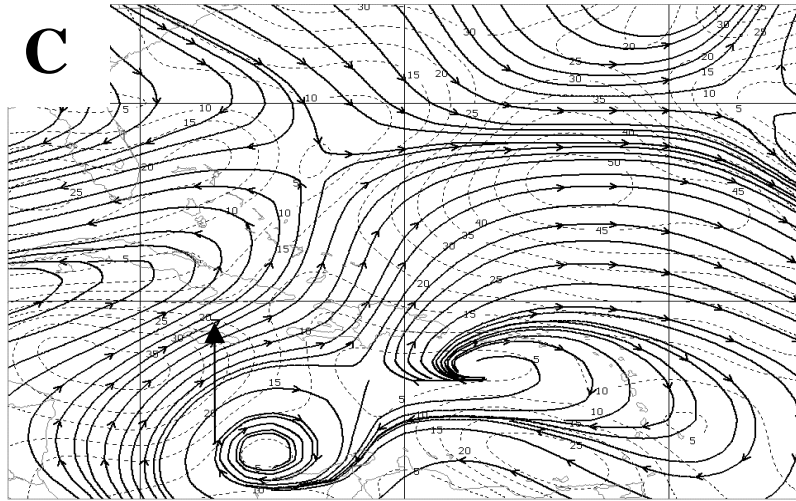
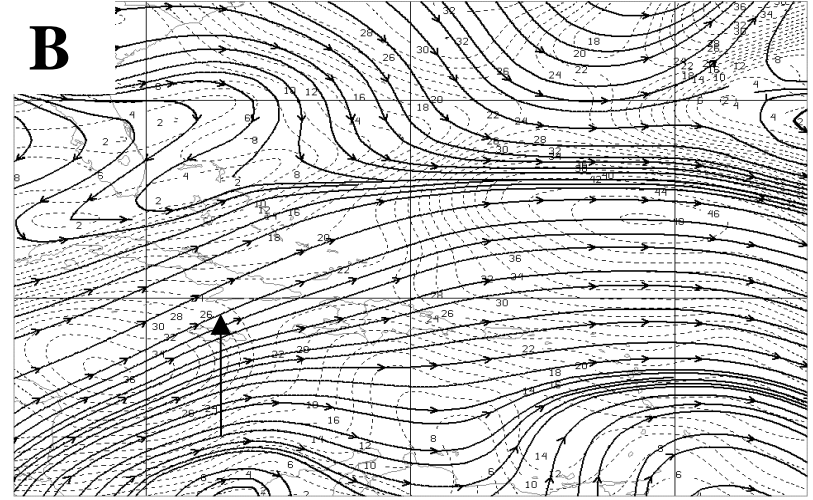
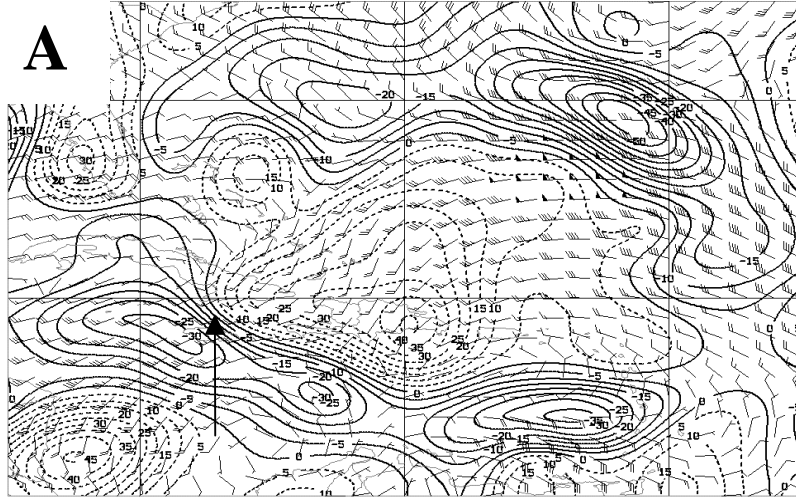
Figure 9. Same as in Figure 6 except for August 23 2000 0000 UTC.



SFR 2005 TIME:10J25Z DAY:3900236900236

VOR:115K1E590200 TIME:10J25Z DAY:0800236

Figure 10. Same as in Figure 6 except for August 23 2000 1200 UTC.



SFR 2005 TIME:022726Z DAY:3900236900236

VOR: (115K1E59)2005 TIME: 22726Z DAY:0800236

1  
**Figure 11.** Same as in Figure 6 except for August 24 2000 0000 UTC.

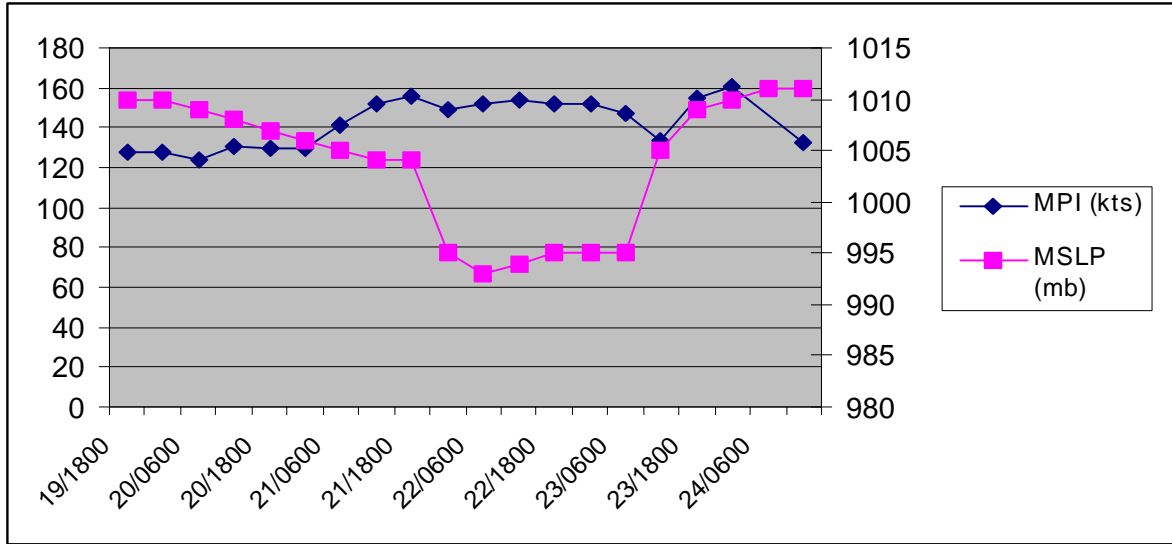


**Figure 12.** Time series analysis of maximum potential intensity (MPI) (kts) versus mean sea level pressure (MSLP) (mb) for August 19 1800 UTC through August 24 1200 UTC.

### TOPEX/ERS-2 Analysis Aug 22 2000

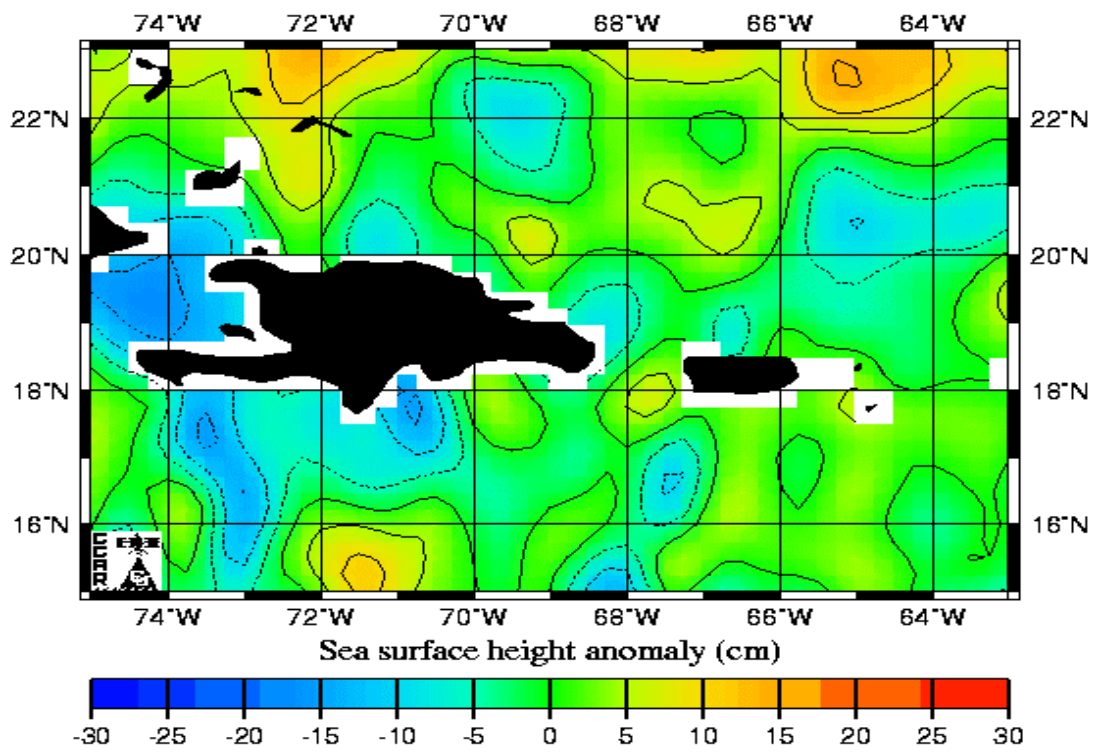


**Figure 13.** Topex/ERS-2 sea height anomaly (cm) analysis for August 22 2000. Warm colors indicate positive anomalies, and cool colors indicate negative anomaly.

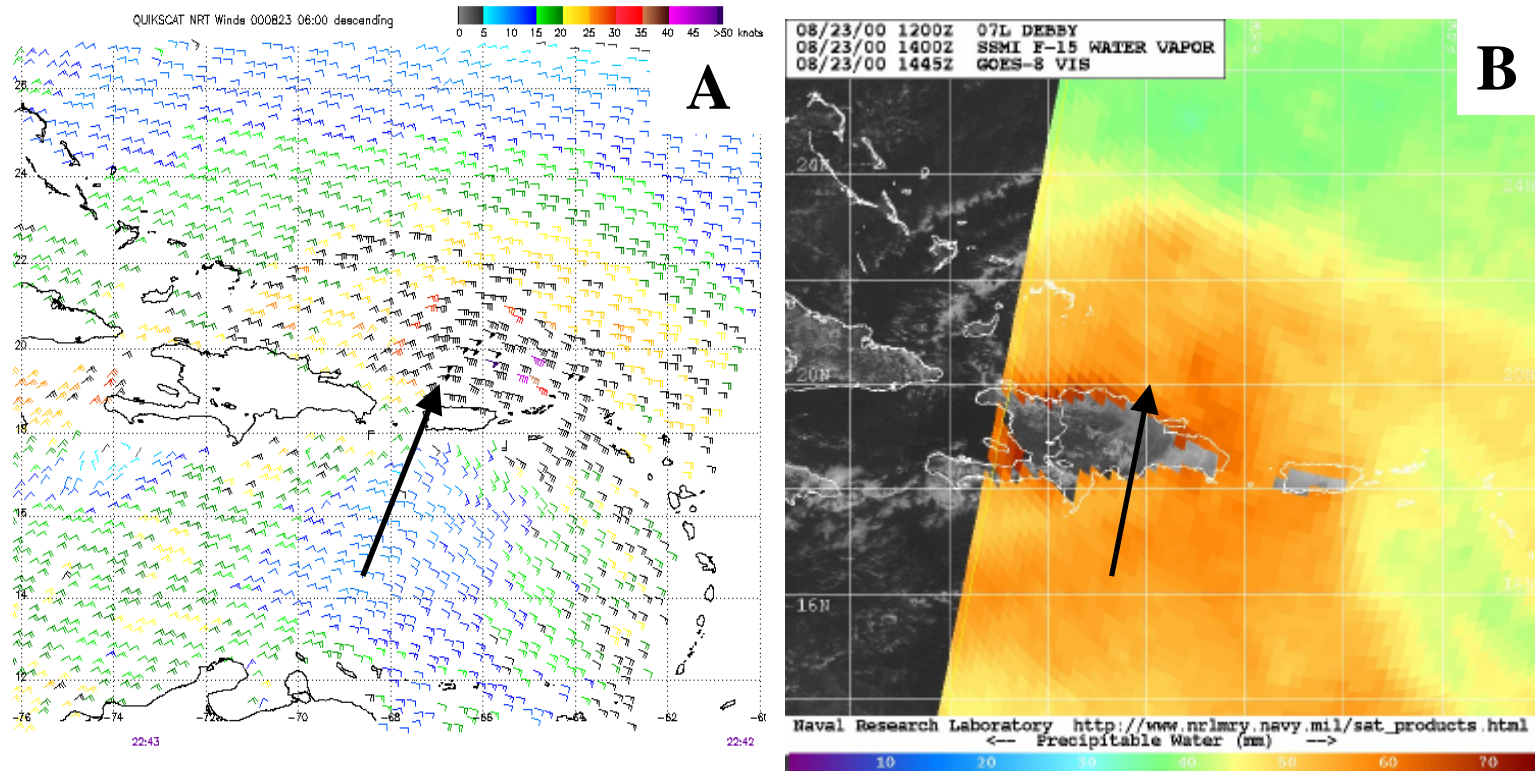


**Figure 14.** SeaWinds scatterometer surface winds (10 m) over Debby on August 22, 2000 (panel A) and SSM/I 22 GHz low-level vertical integrated water vapor (panel B) at 1400 UTC August 23 2000. For panel A, times (GMT) are denoted at bottom of image and correspond to time when right edge of swath passes 25N. Black barbs indicate rain contamination. For panel B, cool colors indicated drier air. Tip of arrow indicates approximate location of Debby at 0000 UTC 23 August 2000 (panel A) and 1200 UTC 23 August 2000 (panel B).

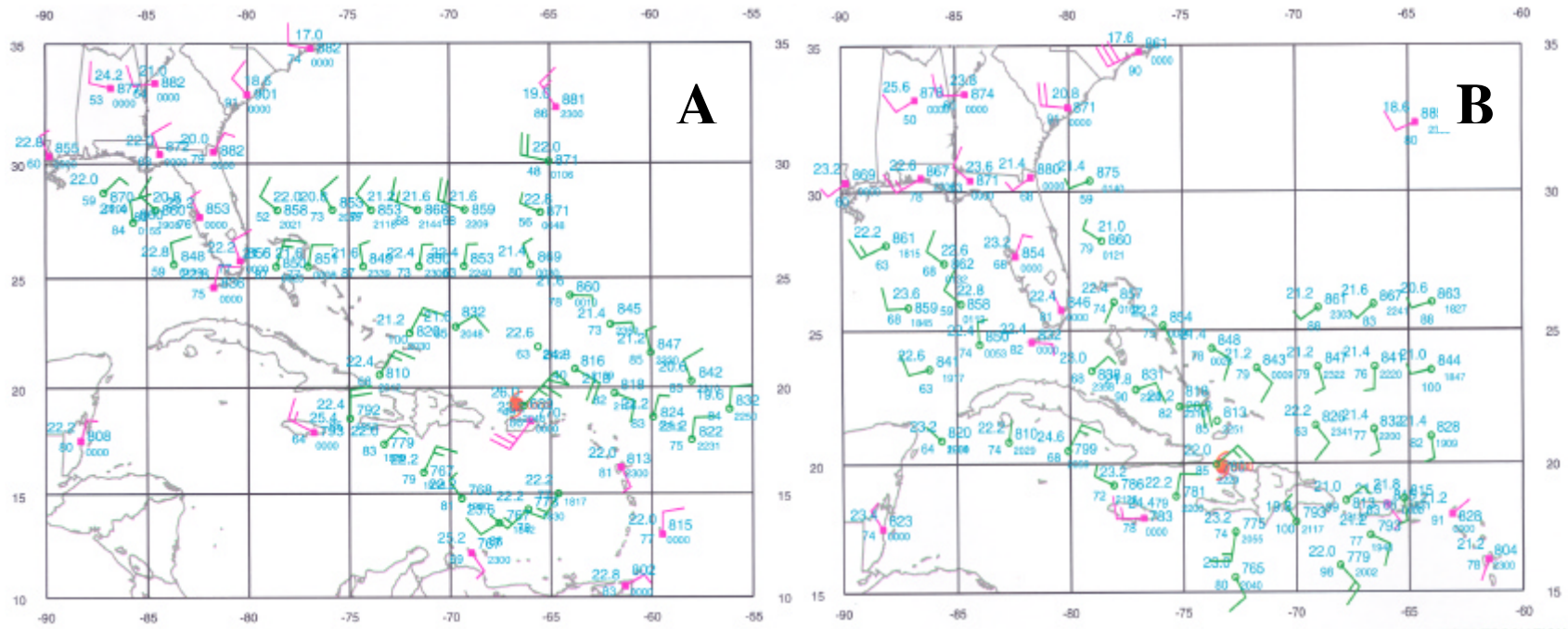


**Figure 15.** 925 hPa storm-relative flow for 0000 UTC 23 August (panel A) and 0000 UTC 24 August (panel B). Gray wind barbs denote upper air soundings. Black wind barbs denote NOAA G-IV dropsondes with text indicating time of dropsonde in UTC (lower right) relative humidity in percent (lower left), temperature in Celsius (upper left), and geopotential height in meters (upper right).

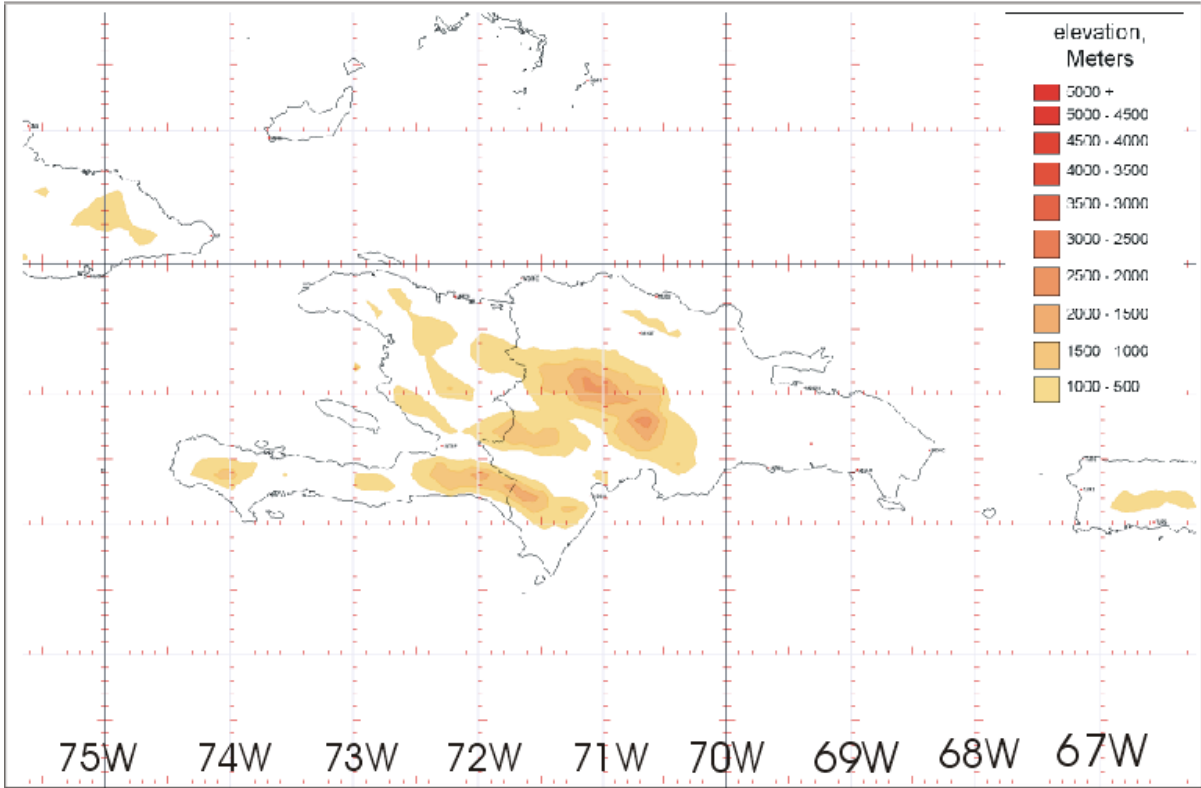


**Figure 16.** Hispaniola elevation contours (m).

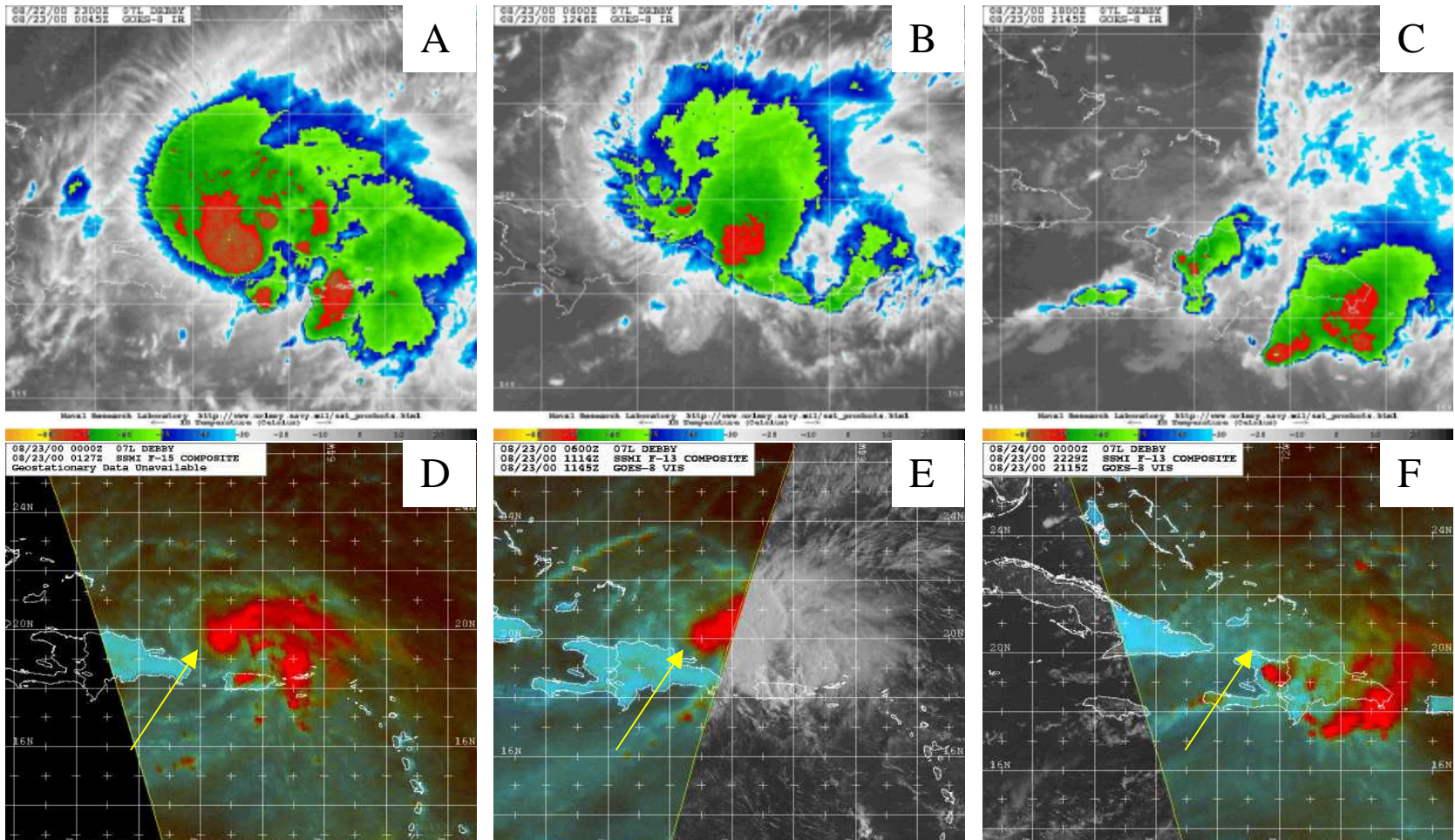


**Figure 17.** GOES-8 infrared satellite imagery at 0045 UTC 23 August (panel A), 1246 UTC 23 August (panel B), and 2145 23 August (panel C) along with SSM/I 85 GHz at 0127 UTC 23 August (panel D), 1114 UTC 23 August (panel E), and 2229 UTC 23 August (panel F). Tip of arrow indicates approximate location of the center of Debby.

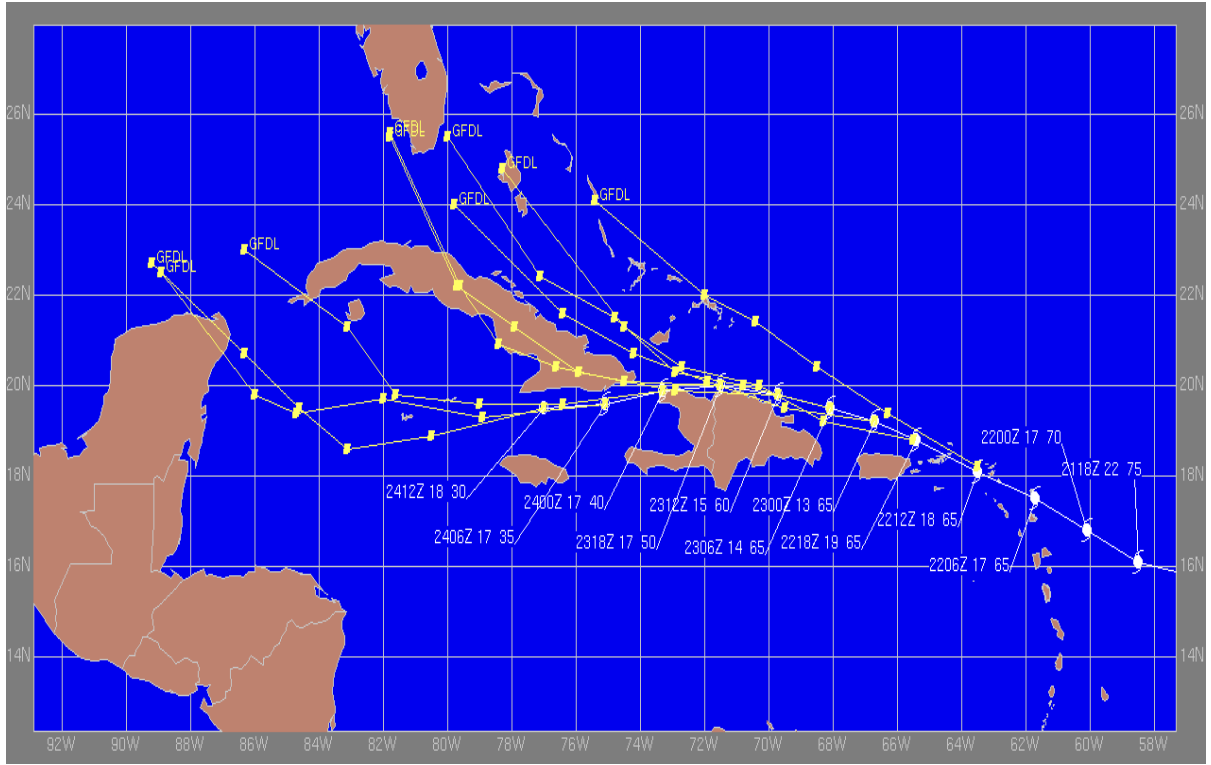


**Figure 18.** Official NHC best-track (white line) for Debby (2000) versus 72-hour forecast track guidance (yellow line) from GFDL simulations (initialized 1200 UTC 22 August through 1800 UTC 24 August) indicating a consistent poleward bias.

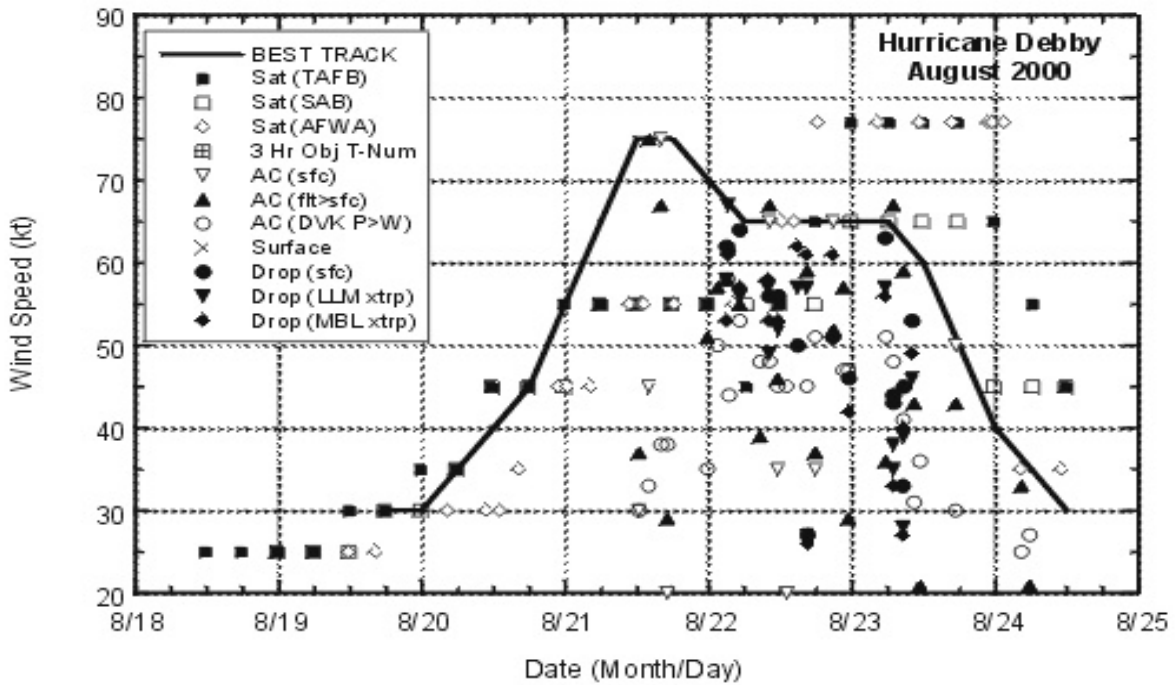


**Figure 19.** Official National Hurricane Center best track maximum sustained surface wind speed curve for Debby, 19-24 August 2000, and the observations on which the best track curve is based. AC denotes aircraft observations, which have been adjusted for elevation using 90%, 80%, and 85% reduction factors for observations from 700 hPa, 850 hPa, and 1500 feet, respectively. Drop denotes dropsonde observations which include actual 10 meter winds (sfc), as well as surface estimates derived from the mean wind over the lowest 150 meters of the wind sounding (LLM), and from the sounding boundary layer mean (MBL). Sat denotes satellite intensity estimates using Dvorak technique (adapted from Pasch 2000).

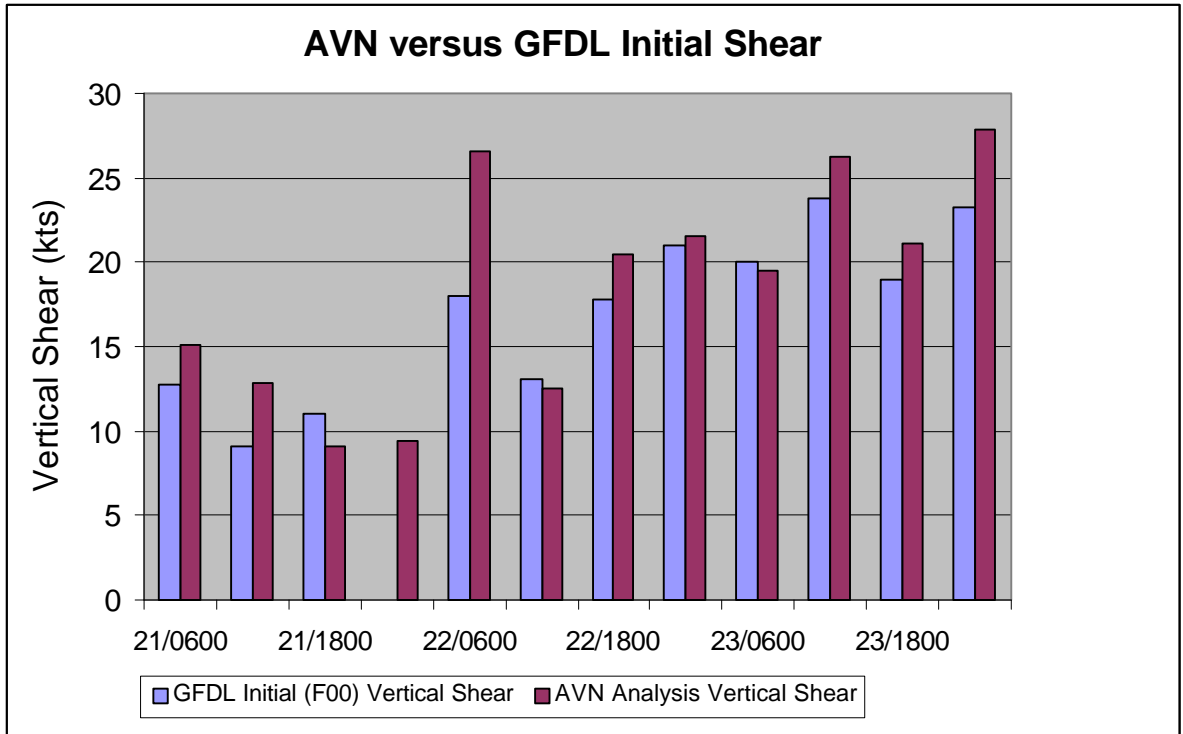


**Figure 20.** Comparison of the GFDL versus AVN initial vertical shear.

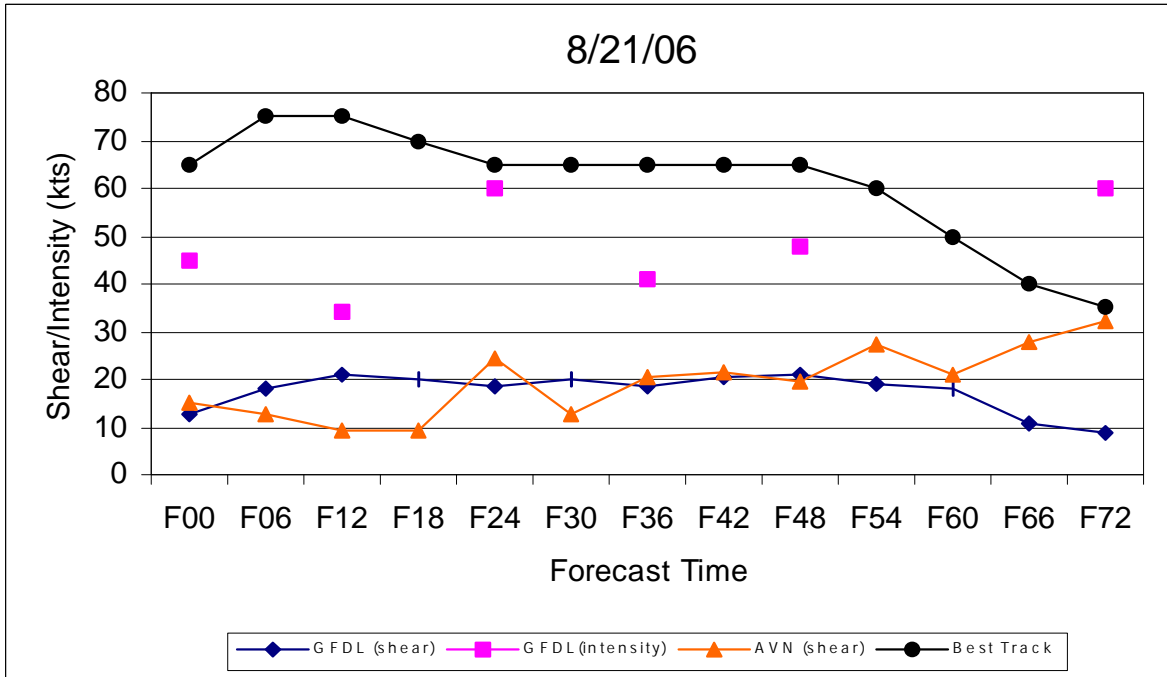


**Figure 21.** Time-series analysis of NHC best track intensity (knots), GFDL 72-hour forecast intensity (knots) initialized 0600 UTC 21 August 2000, AVN Global analysis vertical shear (knots), and the GFDL 72-hour forecast vertical shear (knots) initialized 0600 UTC 21 August 2000. Time period extends from 0600 UTC 21 August (2000) through 0600 UTC 24 August 2000.

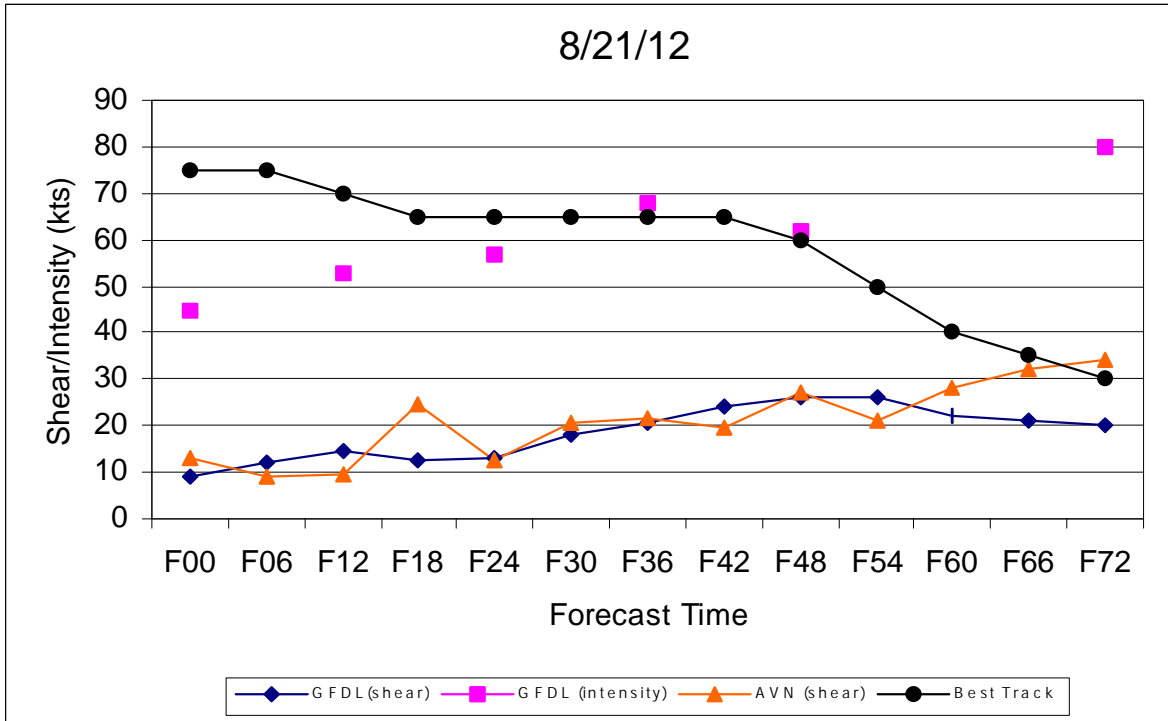


**Figure 22.** Time-series analysis of NHC best track intensity (knots), GFDL 72-hour forecast intensity (knots) initialized 1200 UTC 21 August 2000, AVN Global analysis vertical shear (knots), and the GFDL 72-hour forecast vertical shear (knots) initialized 1200 UTC 21 August 2000. Time period extends from 1200 UTC 21 August (2000) through 1200 UTC 24 August 2000.

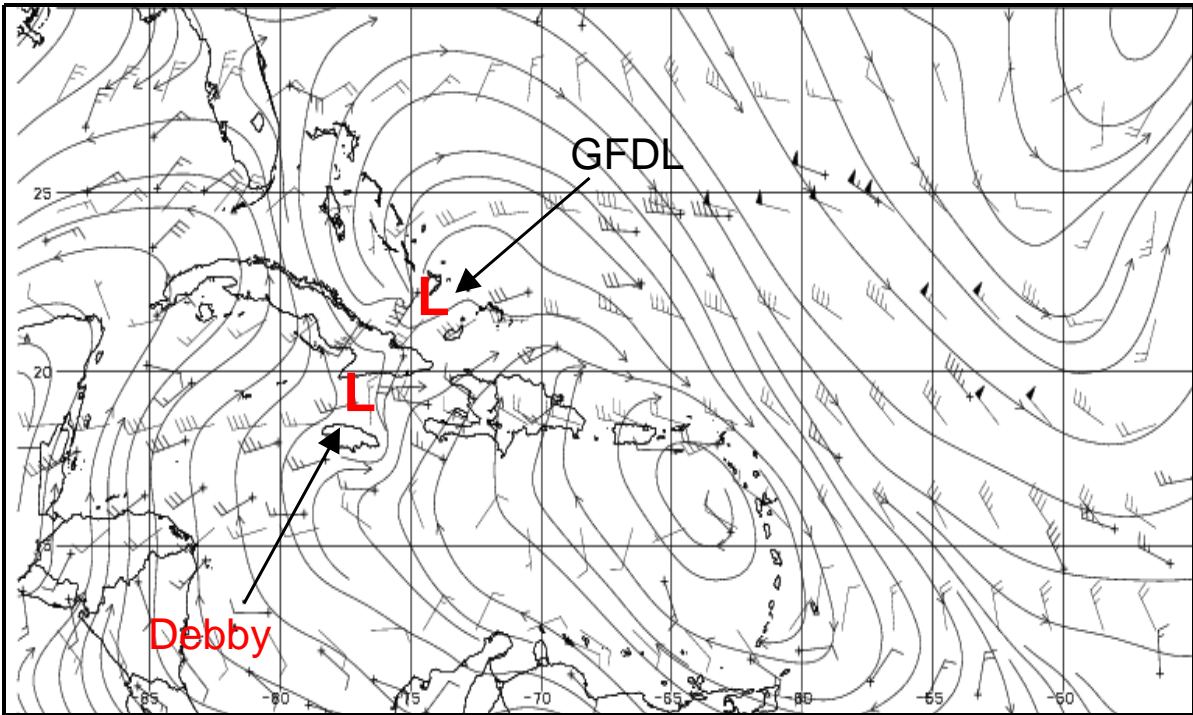


**Figure 23.** Comparison of the 72-hour GFDL 200 hPa forecast winds (streamlines) initialized 1200 UTC 21 August (2000) versus satellite derived winds (wind barbs with cross), upper-air data (wind barbs with diamonds), and the GFDL analysis (wind barbs) valid 1200 UTC 23 August 2000.

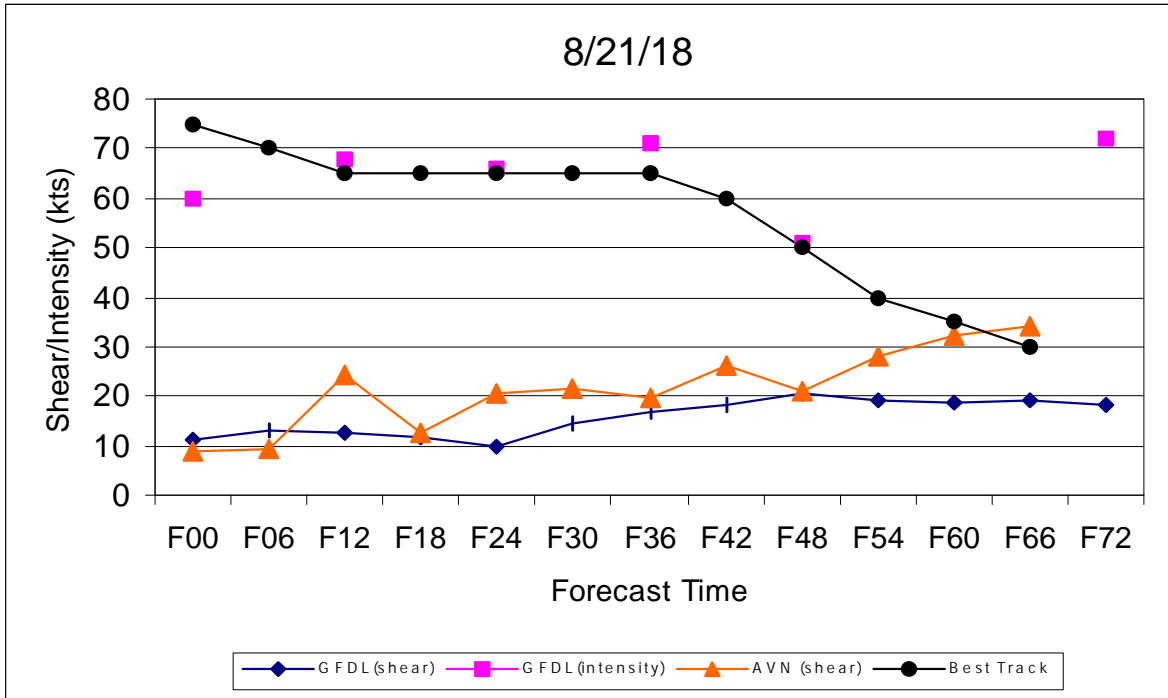


**Figure 24.** Time-series analysis of NHC best track intensity (knots), GFDL 72-hour forecast intensity (knots) initialized 1800 UTC 21 August 2000, AVN global analysis vertical shear (knots), and the GFDL 72-hour forecast vertical shear (knots) initialized 1800 UTC 21 August 2000. Time period extends from 1800 UTC 21 August (2000) through 1800 UTC 24 August 2000.

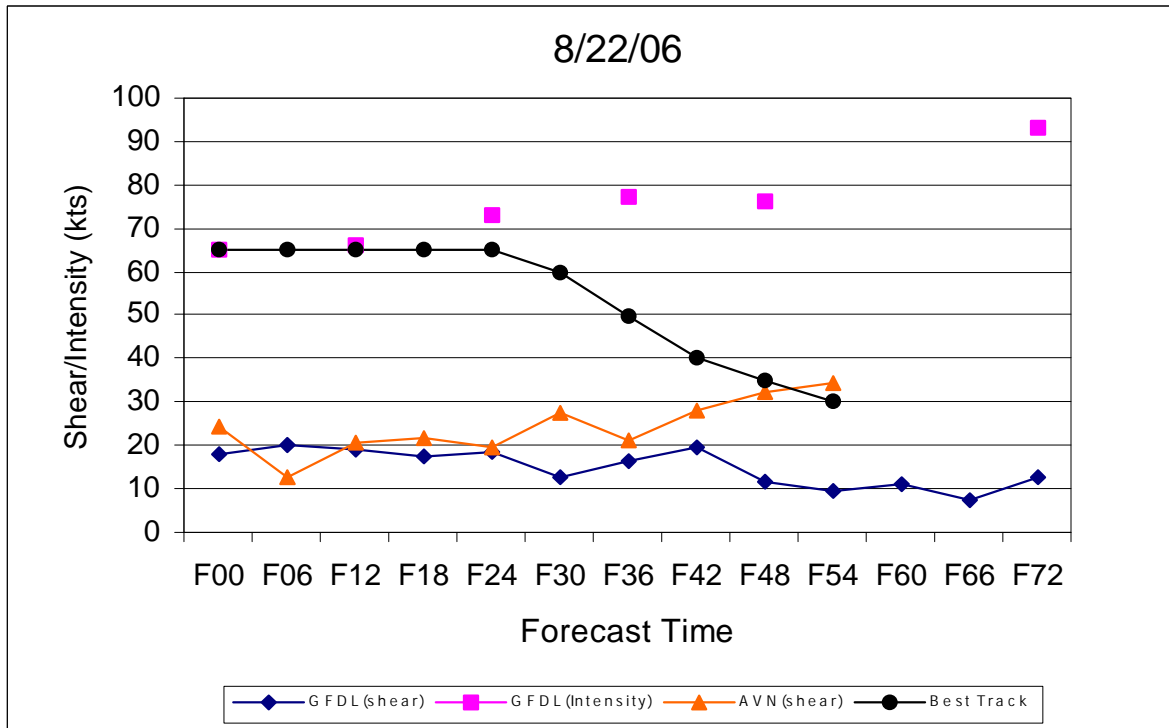


**Figure 25.** Time-series analysis of NHC best track intensity (knots), GFDL 72-hour forecast intensity (knots) initialized 0600 UTC 22 August 2000, AVN global analysis vertical shear (knots), and the GFDL 72-hour forecast vertical shear (knots) initialized 0600 UTC 22 August 2000. Time period extends from 0600 UTC 22 August (2000) through 0600 UTC 25 August 2000.

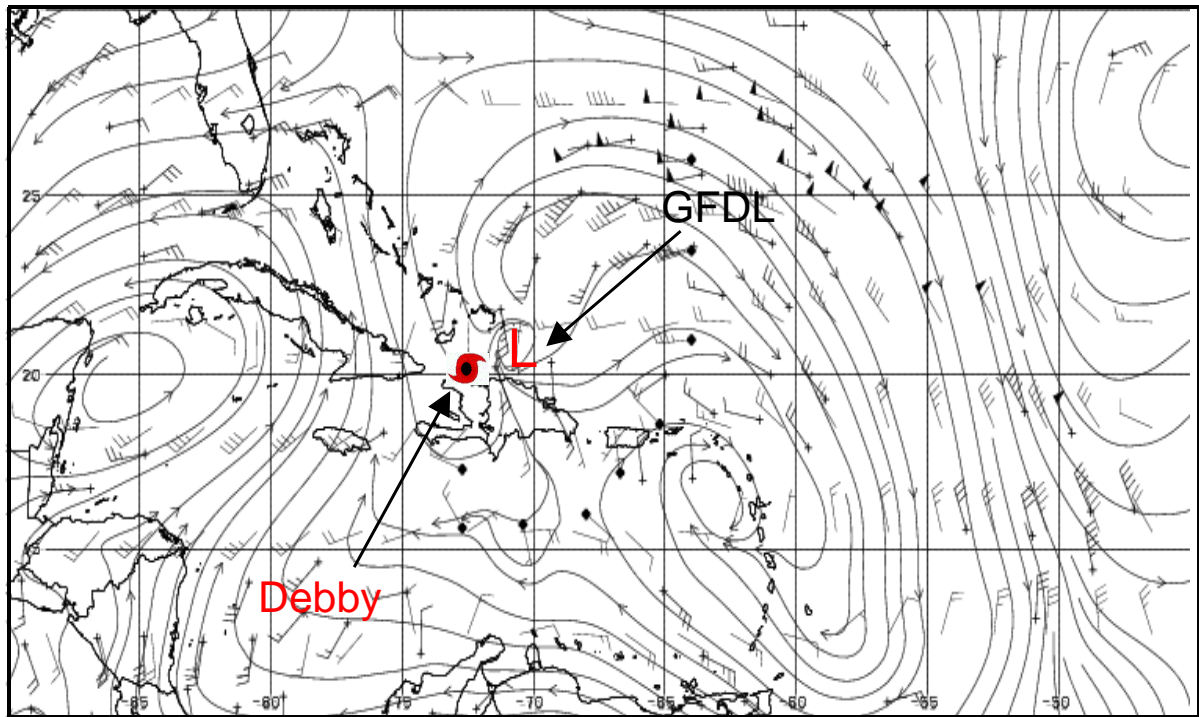


**Figure 26.** Comparison of the 36-hour GFDL 200 hPa forecast winds (streamlines) initialized 0600 UTC 22 August (2000) versus NOAA G-IV dropsondes (wind barbs with circles), satellite derived winds (wind barbs with cross), upper-air data (wind barbs with diamonds), and the GFDL analysis (wind barbs) valid 1800 UTC 23 August 2000.

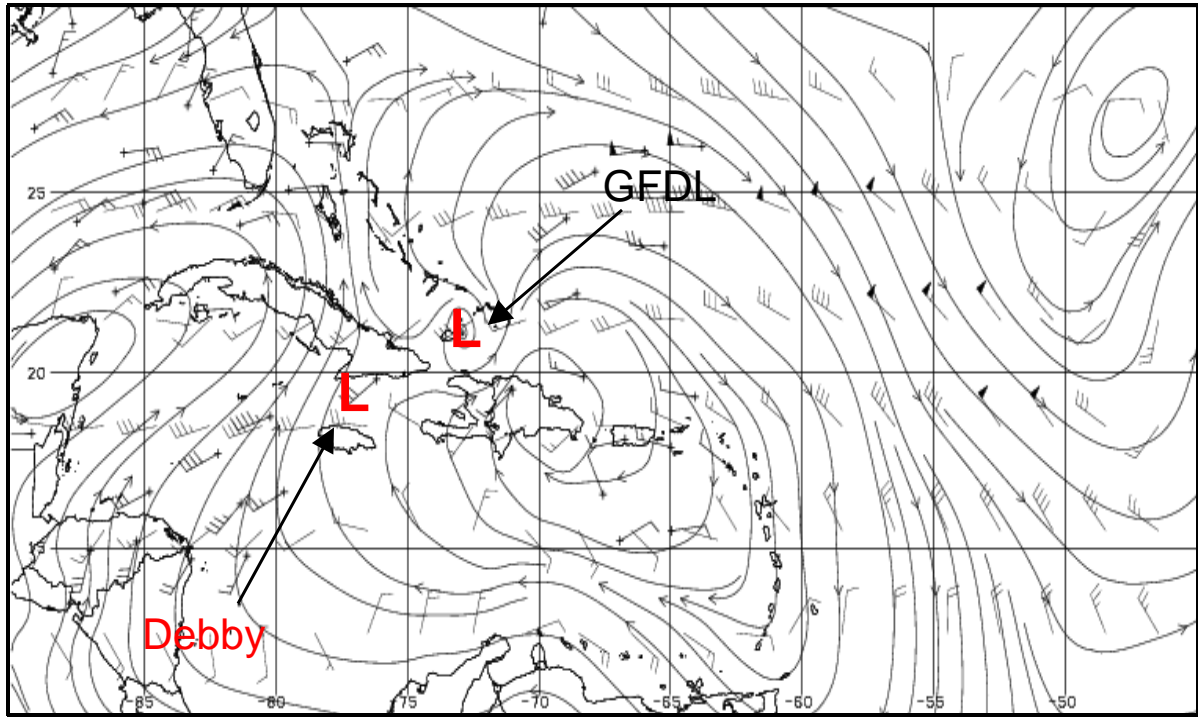


**Figure 27.** Comparison of the 48-hour GFDL 200 hPa forecast winds (streamlines) initialized 0600 UTC 22 August (2000) versus satellite derived winds (wind barbs with cross), upper-air data (wind barbs with diamonds), and the GFDL analysis (wind barbs) valid 0600 UTC 24 August 2000.

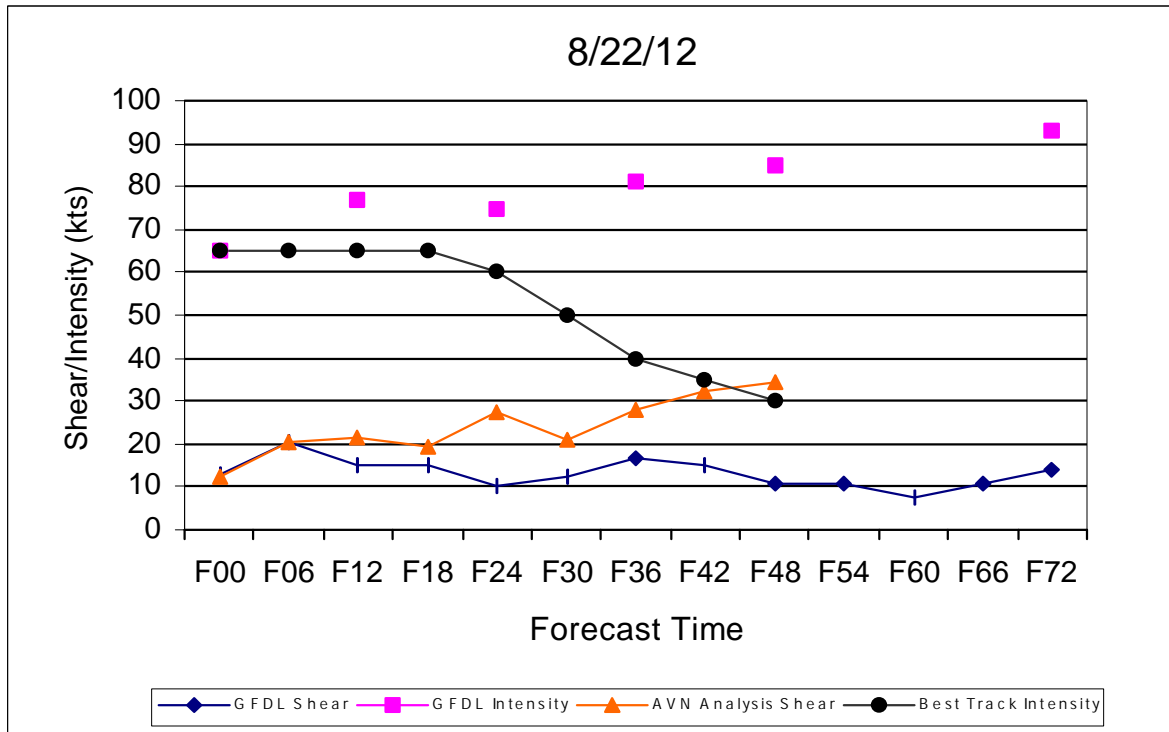


**Figure 28.** Time-series analysis of NHC best track intensity (knots), GFDL 72-hour forecast intensity (knots) initialized 1200 UTC 22 August 2000, AVN global analysis vertical shear (knots), and the GFDL 72-hour forecast vertical shear (knots) initialized 1200 UTC 22 August 2000. Time period extends from 1200 UTC 22 August (2000) through 1200 UTC 25 August 2000.

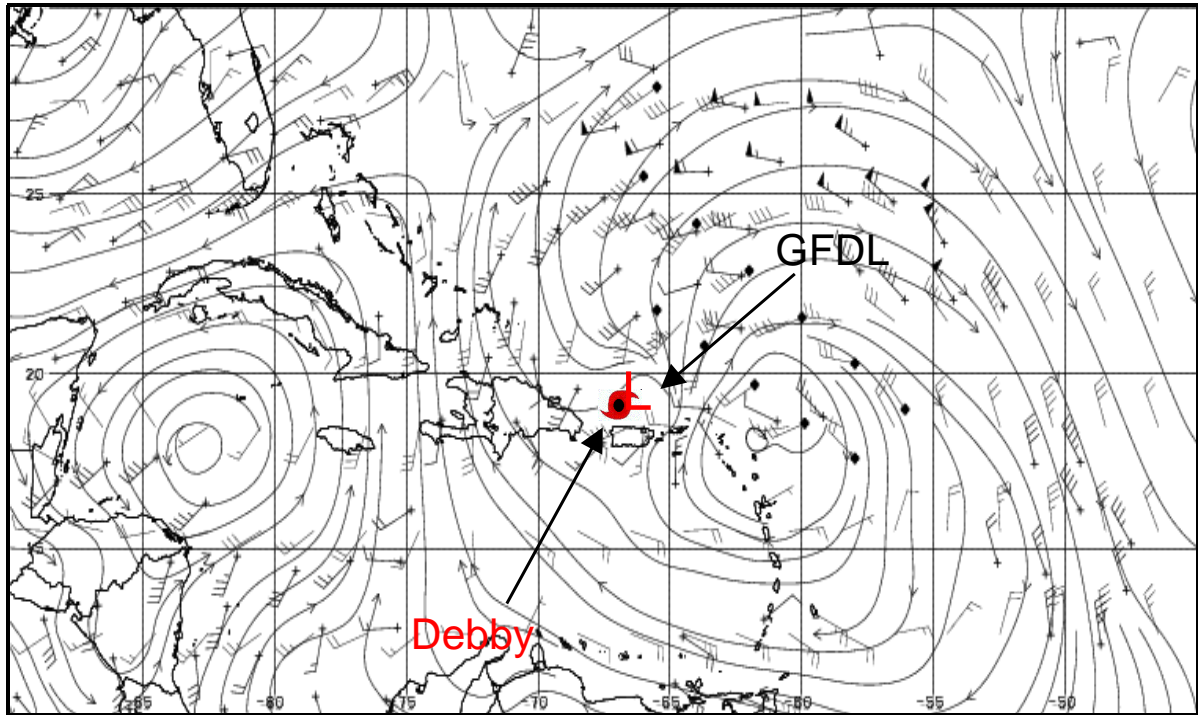


**Figure 29.** Comparison of the 12-hour GFDL 200 hPa forecast winds (streamlines) initialized 1200 UTC 22 August (2000) versus NOAA G-IV dropsondes (wind barbs with circles), satellite derived winds (wind barbs with cross), upper-air data (wind barbs with diamonds), and the GFDL analysis (wind barbs) valid 0000 UTC 23 August 2000.

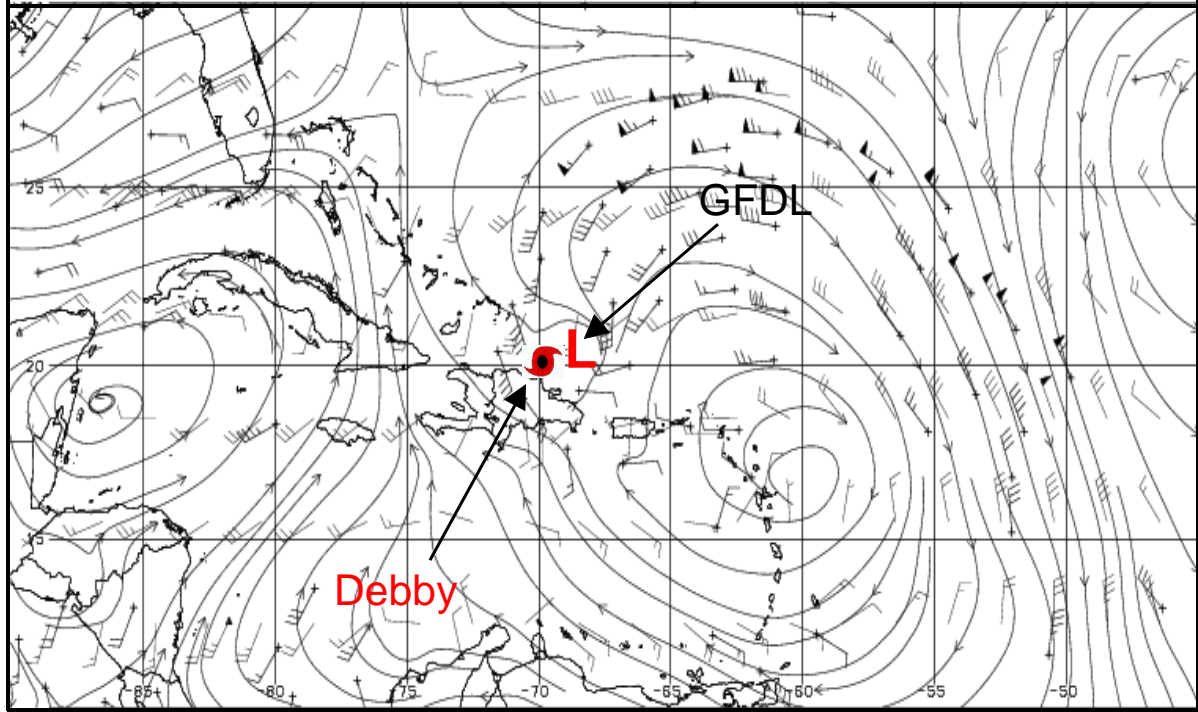


**Figure 30.** Comparison of the 24-hour GFDL 200 hPa forecast winds (streamlines) initialized 1200 UTC 22 August (2000) versus satellite derived winds (wind barbs with cross), upper-air data (wind barbs with diamonds), and the GFDL analysis (wind barbs) valid 1200 UTC 23 August 2000.

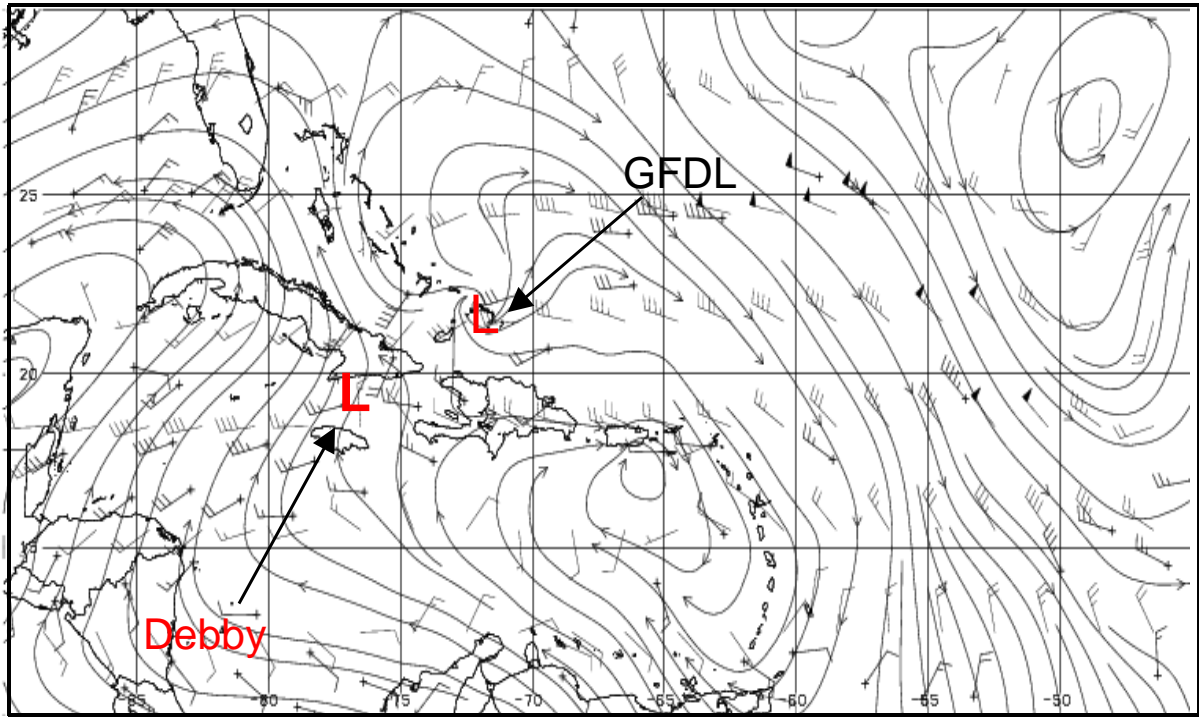


**Figure 31.** Comparison of the 48-hour GFDL 200 hPa forecast winds (streamlines) initialized 1200 UTC 22 August (2000) versus satellite derived winds (wind barbs with cross), upper-air data (wind barbs with diamonds), and the GFDL analysis (wind barbs) valid 1200 UTC 24 August 2000.

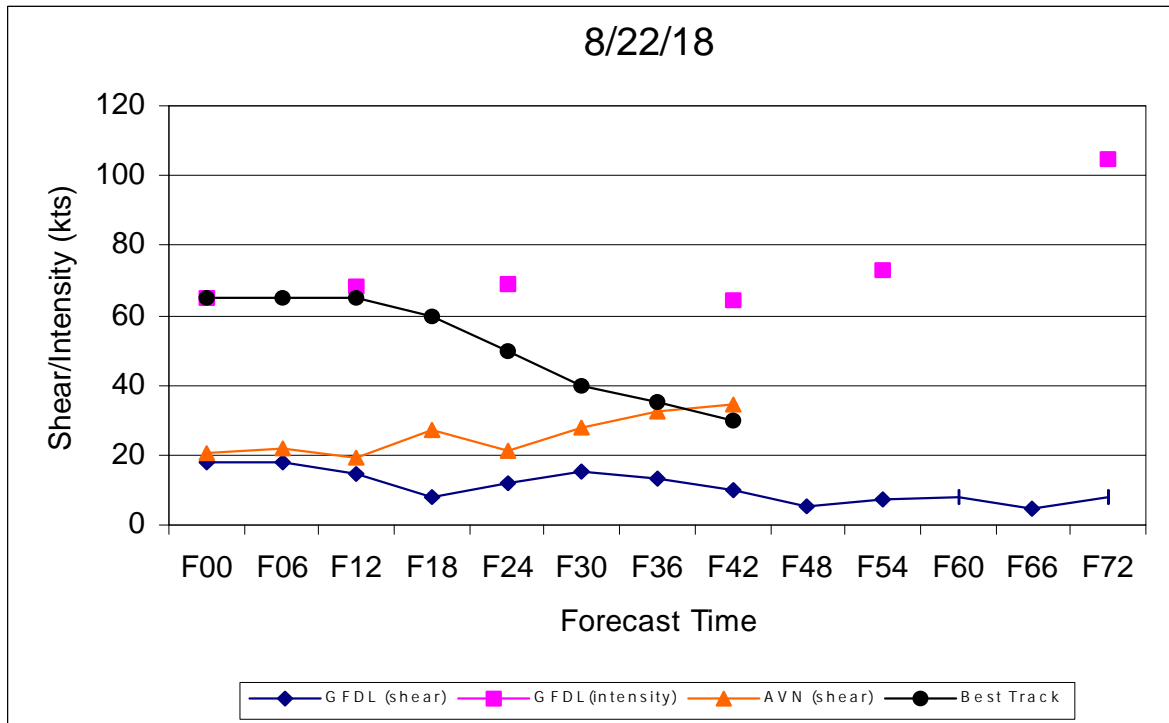


**Figure 32.** Time-series analysis of NHC best track intensity (knots), GFDL 72-hour forecast intensity (knots) initialized 1800 UTC 22 August 2000, AVN global analysis vertical shear (knots), and the GFDL 72-hour forecast vertical shear (knots) initialized 1800 UTC 22 August 2000. Time period extends from 1800 UTC 22 August (2000) through 1800 UTC 25 August 2000.

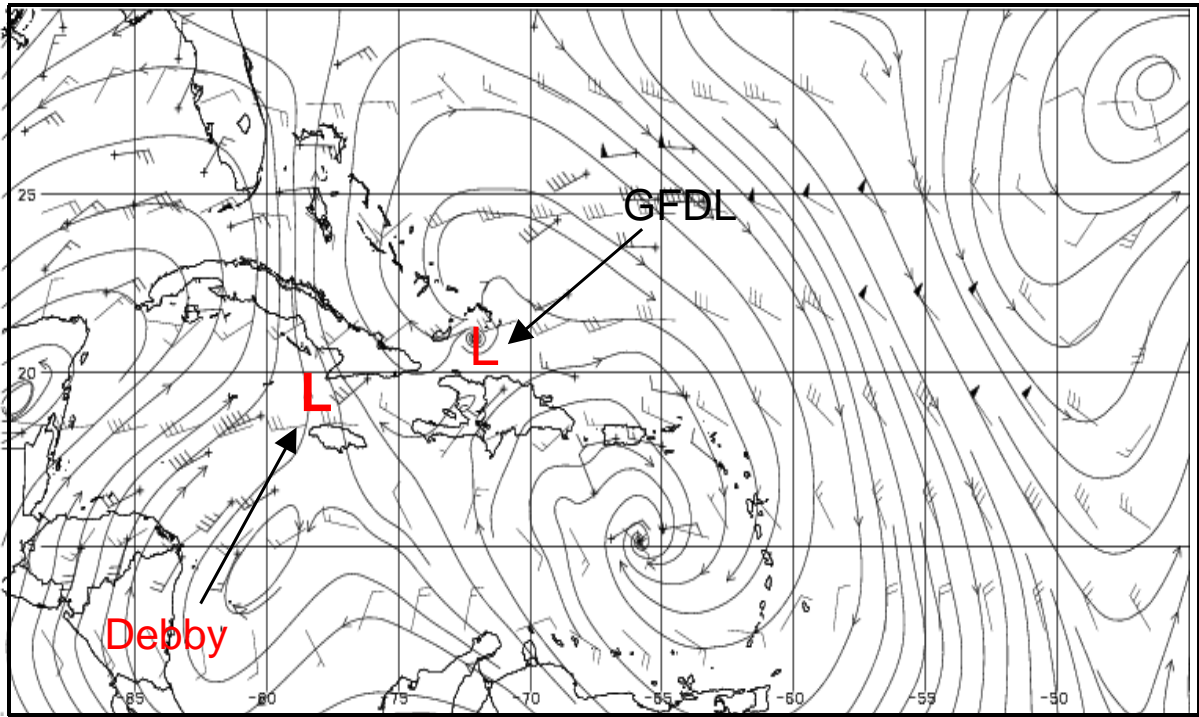


**Figure 33.** Comparison of the 36-hour GFDL 200 hPa forecast winds (streamlines) initialized 1800 UTC 22 August (2000) versus satellite derived winds (wind barbs with cross), upper-air data (wind barbs with diamonds), and the GFDL analysis (wind barbs) valid 0600 UTC 24 August 2000.

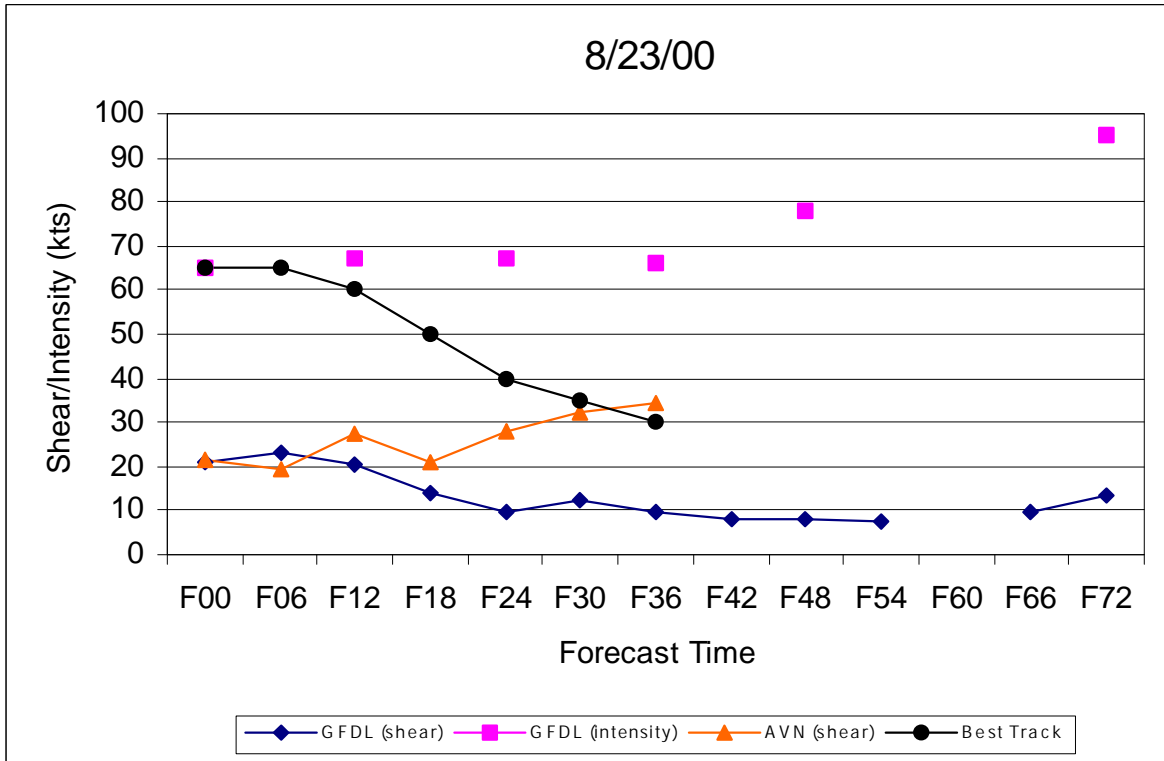


**Figure 34.** Time-series analysis of NHC best track intensity (knots), GFDL 72-hour forecast intensity (knots) initialized 0000 UTC 23 August 2000, AVN global analysis vertical shear (knots), and the GFDL 72-hour forecast vertical shear (knots) initialized 0000 UTC 23 August 2000. Time period extends from 0000 UTC 23 August (2000) through 1200 UTC 24 August 2000.

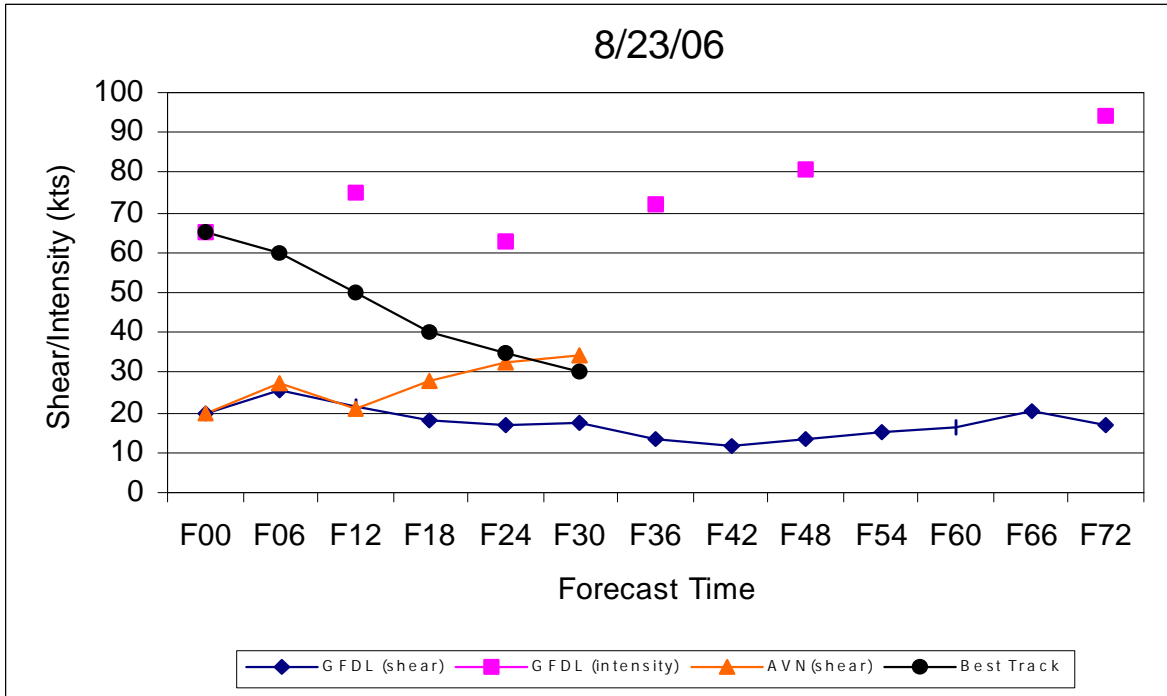


**Figure 35.** Time-series analysis of NHC best track intensity (knots), GFDL 72-hour forecast intensity (knots) initialized 0600 UTC 23 August 2000, AVN global analysis vertical shear (knots), and the GFDL 72-hour forecast vertical shear (knots) initialized 0600 UTC 23 August 2000. Time period extends from 0600 UTC 23 August (2000) through 0600 UTC 26 August 2000.

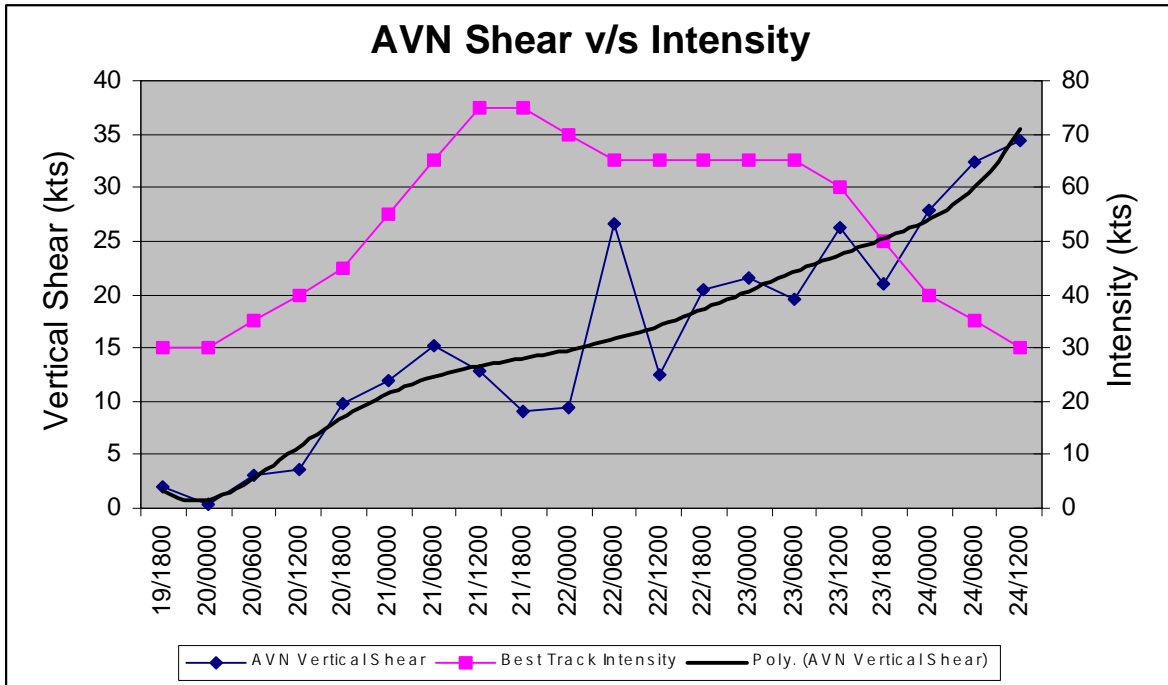


**Figure 36.** Time-series analysis of NHC best track intensity (knots) versus vertical shear (knots) calculated from the AVN global analysis valid 1800 UTC 19 August 2000 through 1200 UTC 24 August 2000. A trend analysis is also shown for vertical shear using a six-degree polynomial function. Horizontal axis denotes time (tick mark equals 6 hours).

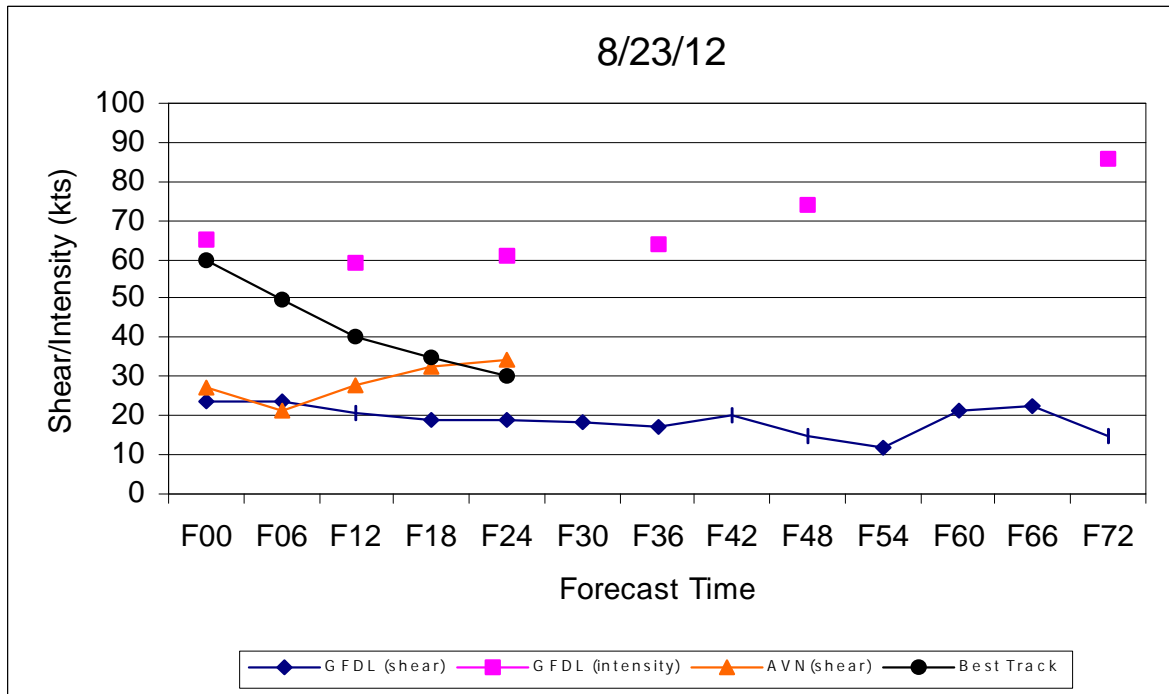


**Figure 37.** Time-series analysis of NHC best track intensity (knots), GFDL 72-hour forecast intensity (knots) initialized 1200 UTC 23 August 2000, AVN global analysis vertical shear (knots), and the GFDL 72-hour forecast vertical shear (knots) initialized 1200 UTC 23 August 2000. Time period extends from 1200 UTC 23 August (2000) through 1200 UTC 26 August 2000.

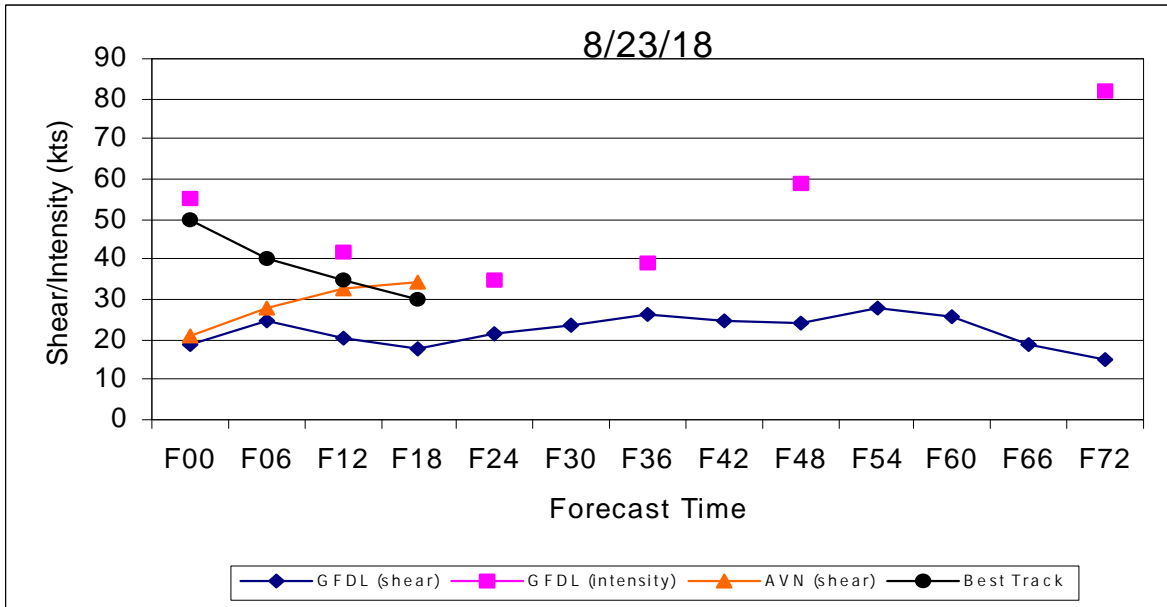


**Figure 38.** Time-series analysis of NHC best track intensity (knots), GFDL 72-hour forecast intensity (knots) initialized 1800 UTC 23 August 2000, AVN global analysis vertical shear (knots), and the GFDL 72-hour forecast vertical shear (knots) initialized 1800 UTC 23 August 2000. Time period extends from 1800 UTC 23 August (2000) through 1800 UTC 26 August 2000.